

PhD THESIS

Distinct Element Simulations of Granular Materials

by

SÁNDOR FAZEKAS

Supervisor:

Prof. János Kertész



Department of Theoretical Physics
Budapest University of Technology and Economics
Budapest, Hungary

(2007)

Nyilatkozat

Alulírott Fazekas Sándor kijelentem, hogy ezt a doktori értekezést magam készítettem és abban csak a megadott forrásokat használtam fel. minden olyan részt, amelyet szó szerint, vagy azonos tartalomban, de átfogalmazva más forrásból átvettettem, egyértelműen, a forrás megadásával megjelöltem.

Budapest, 2007. június 21.

Fazekas Sándor

Acknowledgments

I am greatly indebted to my supervisor Prof. János Kertész and also to Prof. Dietrich E. Wolf without the help of whom I would have been unable to complete this work. I am very grateful to Prof. Dmitry Chetverikov who supported and encouraged me in finishing this Thesis. I am also very grateful to my high school teacher István Bartos-Elekes who motivated me the most to become a physicist. János Török, Tamás Unger, and Henning A. Knudsen have also helped my work with many fruitful discussions.

Preface

Granular materials, which are essentially large conglomerations of macroscopic solid particles, are relevant for many different areas of science and technology. Their study forms a wide interdisciplinary research field attracting the interest of physicists, applied mathematicians, geologists, as well as chemical, civil, mechanical, and agricultural engineers. Progress in mastering the theoretical complexity of granular behavior and also improvements in industrial production and process performance can be partly expected from the development of computational methods.

In the past couple of decades, computer simulations have already become important research, modeling, and design tools used to conduct investigations which are difficult (or expensive) to carry out in experiments. Distinct element simulations offer an ideal way to study the relation between micromechanical theories and macroscopic behavior of granular materials observed in experiments. These techniques are becoming more and more efficient as computational power grows.

In the work presented here, with distinct element simulations, I have investigated several aspects of the dynamic and quasistatic behavior of granular systems. In the first part of my work, I studied systems where magnetic attractive forces were present between the grains. The dipole interaction between iron spheres placed in a magnetic field can be viewed as a kind of adhesion force and the system itself as a model for cohesive granular materials. By varying the strength of the magnetic field, this model facilitates the study of the transition from noncohesive to cohesive behavior.

Computer simulations of dipolar magnetic systems have to deal with the long range nature of the dipole-dipole interaction. The size of the tractable systems is limited through the fact that the order of N^2 calculations are to be carried out at each simulation step, where N is the number of particles. It is crucial from the point of view of efficient simulations to know if a reasonable cutoff can be introduced in such a system.

I investigated this question by comparing the stability of static configurations, focusing on characteristic local orderings, which play a central role in the behavior of granular systems. Based on numerical calculations, I derived a lowest reasonable interaction cutoff, which made it possible to run systematic two-dimensional distinct element simulations. For a deeper understanding of the similarities and differences of magnetic and other types of cohesive systems (such as wet granular matter and dry fine powders), I analyzed piling and avalanches of magnetized grains at different levels of magnetization.

In the second part of my work, I studied spontaneous strain localization in non-cohesive granular systems by means of three-dimensional distinct element simulations. In granular materials undergoing slow shear, the strain is usually localized to narrow domains called shear bands. Strain localization has a vast literature dating back to decades and including both numerical and experimental studies. However, most of these studies focus only on two-dimensional boundary induced shear bands.

Three-dimensional studies have a major drawback in the difficulty of getting information from inside a sheared sample. They gained increasing attention when experimental tools such as Computer Tomography became available. Triaxial shear tests revealed complex localization patterns and shear band morphologies depending on the test conditions. In computer simulations modeling the usual experimental setup of triaxial shear tests, I reproduced different shear band morphologies and analyzed their properties.

One important factor of the behavior of granular materials is the packing density of the grains. On one hand, dense granular samples dilate during slow deformations (as it was noted by Reynolds already in 1885), on the other hand, loose granular samples densify as a result of periodic shearing. Based on experimental results and theoretical considerations, it is tempting to assume that inside shear bands a granular system self-organizes its density to a unique (critical) value.

The relevance of distinct element simulations modeling triaxial shear tests is at least twofold: (1) they help the understanding of the strain localization process at fixed conditions, and (2) they make it possible to accurately control the density and the internal friction of the samples, which is difficult in experiments. Based on this, I investigated the relation between packing density and strain localization by simulating triaxial shear tests using different initial densities and friction coefficients.

Following the self-organization of a spontaneous strain localization process leading to a well-defined shear band, I identified the grains in this failure zone and I measured their packing density. I found evidence, that the packing state arising from the dynamic equilibrium of dilation and compaction, characteristic to strain localization, is restricted to the shear bands, while the density outside of shear bands keeps the memory of the initial packing conditions. The asymptotic packing density developed in shear bands depends on the coefficient of friction. At large friction, the shear bands approach a low density *dynamic random loose packing* (DRLP) state. I estimated the packing density of the DRLP state based on the friction dependence of the localization process.

This Thesis is organized as follows: Chapter 1 outlines the significance and the basic properties of granular materials. Chapters 2 and 3 present a short phenomenological and theoretical introduction to specific topics such as piling, avalanches, strain localization, shear bands, and packing density, which are going to be discussed in more details later. Chapter 4 gives a short overview of distinct element simulation techniques with an outlook to other methods. Chapters 5 and 6 discuss a magnetic model of cohesive systems along with the numerical derivation of a lowest reasonable interaction cutoff. Simulation results on piling and avalanches of magnetized grains are presented. Chapters 7 and 8 study strain localization, shear band morphologies, and the development of a critical packing density in shear bands. The Summary outlines the new scientific results (in English and in Hungarian). The Appendix presents additional calculations and technical details which serve for a better understanding of the main text.

Contents

I	Introduction	11
1	Granular materials	13
1.1	Significance and history	13
1.2	Basic properties	14
2	Piling, avalanches, and the effect of cohesion	17
2.1	Angle of stability	18
2.2	Self-organized criticality	19
2.3	Moisture-induced changes	21
2.4	Dry fine powders	23
2.5	Magnetic systems	25
3	Strain localization and the packing density	29
3.1	Shear bands	30
3.2	Granular packings	31
3.3	Criticality of strain localization	33
3.4	Triaxial shear tests	34
4	Distinct element simulations	39
4.1	Overview and outlook	39
4.2	Discrete geometry	42
4.3	Contact models	44
4.4	Motion integration	48
II	Magnetized grains	51
5	Introducing an interaction cutoff	53
5.1	The Luttinger-Tisza method	55
5.2	Two-dimensional array of magnetic particles	56
5.3	The effects of an interaction cutoff	57
5.4	Finite size correction	59
5.5	Bending two lines of magnetic particles	62
5.6	Conclusions and discussion	63
6	Granular piles and avalanches of magnetized particles	65
6.1	Computational method	65
6.2	Simulation setup	68

6.3	Angle of repose and surface roughness	70
6.4	Particle avalanches at zero magnetization	71
6.5	Effect of magnetization on avalanches	72
6.6	The granular regime	74
6.7	The correlated regime	76
6.8	Conclusions and discussion	77
III	Shear bands	79
7	Morphologies of three-dimensional shear bands	81
7.1	Simulations	81
7.2	Local shear intensity	84
7.3	Shear band morphologies	85
7.4	Alternative ways of shear band identification	87
7.5	Stress-strain relation	88
7.6	Conclusions and discussion	89
8	Critical packing density in granular shear bands	91
8.1	Simulations	92
8.2	Spontaneous strain localization	94
8.3	Identification of high shear intensity regions	96
8.4	Volume fraction in shear bands	97
8.5	Global behavior	98
8.6	Conclusions and discussion	100
Summary		103
New scientific results		103
Új tudományos eredmények		105
Appendix		109
A	Tangential force in three-dimensional contacts	109
B	Rotation integration in quaternion representation	111
C	Ground state of a two-dimensional system of dipoles	113
D	Magnetic dipole-dipole interaction	119
E	Otsu's threshold selection method	123
Bibliography		127

Part I

Introduction

Chapter 1

Granular materials

According to a classical definition [112, 113, 47, 120], granular materials are characterized by hard inelastic contacts of their elementary constituents, friction, and negligible thermodynamic effects. For this, dry sand is a canonical example. In most of the cases, granular systems are in metastable states far from equilibrium. They can be activated with vibrations, shear, external volume forces (such as gravity, electric and magnetic fields), and motion of the interstitial fluid or gas (e.g. water or air).

Such driving forces can induce transitions between solid, fluid, and gas-like states, which show characteristics similar in many aspects to conventional solids, liquids, and gases, even though, significant differences do also exist. Recently, granular systems with complex moisture-induced, van der Waals, electric, and magnetic interparticle interactions have gained increasing attention [33, 154, 10]. However, there are still many “basic laws” to be found for the classical case as well [47, 120, 61].

Below we first outline the importance of granular materials and give a short summary of their basic properties. The next two Chapters give an introduction to some more phenomenological and theoretical aspects which are discussed further on in the Part II and III of this Thesis. We do not undertake a complete overview of the literature because of its many subfields and tremendous size. For a most complete and most up to date overview of the current state of the art see [88].

The last Chapter of this introductory part gives a summary of different computational techniques used to study granular systems. We focus on discrete models with special attention on the Distinct Element Method which forms the basis of our investigations presented later on. Distinct element simulations are important mainly because – in a natural way – they make possible a full scale study of granular materials, ranging from grain level to macroscopic behavior.

1.1 Significance and history

In spite of the fact that granular systems are omnipresent in our daily lives, the complete understanding of their behavior is still a major challenge of science. Even in seemingly simple systems such as dry sand, the large number of internal degrees of freedom lead to irreversible interactions and to highly nonlinear effects, making it difficult to relate the known (or assumed) grain scale dynamics to the observed collective behavior.

The question of how to deal with granular materials has a long history dating back to the work of such illustrious scientists as Coulomb [42], who introduced the idea of static

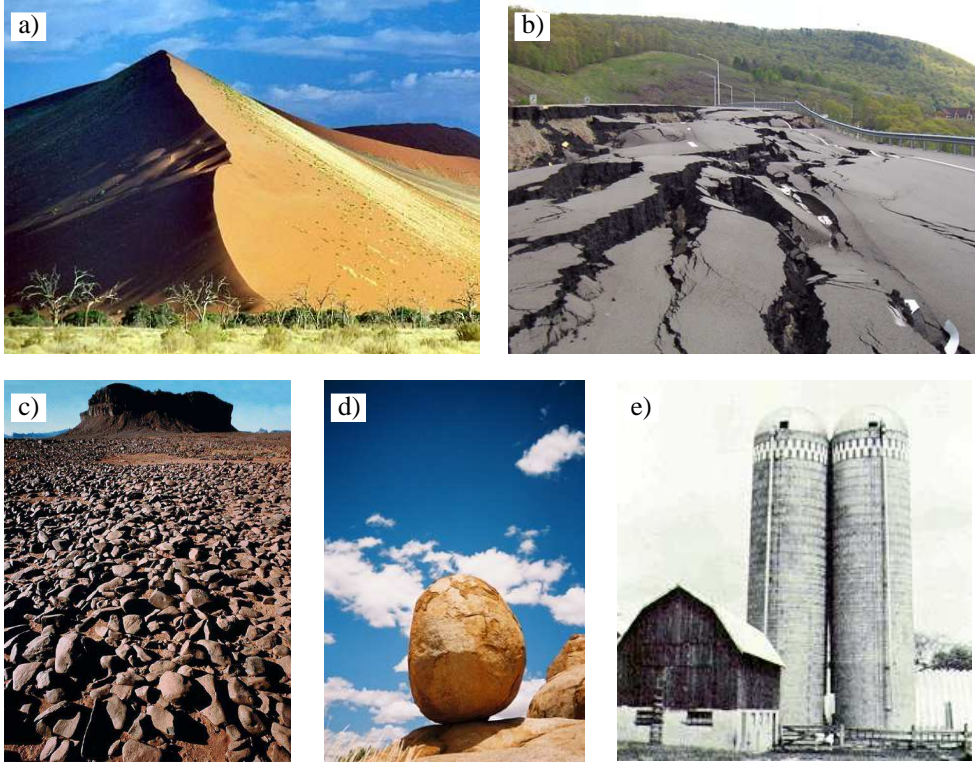


Figure 1.1: Examples of granular systems and related phenomena: (a) Sand dune, (b) Landslide, (c) Stony desert, (d) “Devil’s marble”, (e) “Kissing silos”.

friction (1773), Faraday [65], who discovered the convective instability in vibrated powders (1831), and Reynolds [189], who observed that a compacted granular material must expand in order to undergo any shear (1885).

Erosion and deposition, dune migration, landslides, avalanches, and the instability of silos are just a few example of processes and systems where granular materials play an important role (see Fig. 1.1). Handling, transporting, and storing granular materials are central to a large number of industries including the pharmaceutical, agricultural, mining, and construction industries. Many of the materials processed by these industries (in second largest amount after water) are in granular form.

According to the International Red Cross, it is estimated that landslides cause globally billions of dollars in damage and thousands of deaths and injuries each year. Based on rough estimates, about 5% of the global energy budget is wasted due to problems with granular materials in conveyor belts, sorting machines, mixers, and other industrial machinery operating below optimum. Even a small improvement in understanding granular phenomena can lead to significant benefits.

1.2 Basic properties

In addition to complex internal and external physical conditions and different material parameters such as the stiffness of the particles, as well as the nature of the liquid or gas filling the space between them, a large variety of factors arising from grain geometry (size,



Figure 1.2: Different kinds of sand grains (regular, irregular, round, elongated, smooth, rough, etc.) as seen with a microscope (www.scienceart.nl).

shape, and surface roughness) can significantly influence the particle interactions and the overall behavior of the system.

The size of the grains can vary on a wide scale from very small to very large. At micron and sub-micron particle sizes the attractive van der Waals forces are higher than a typical particle weight. This induces cohesion and leads to very loose packing structures [33]. Even though, for fine powders and suspensions, thermal fluctuations and Brownian motion can be significant, for larger particles, such as a typical sand grain, these are out of question [112, 113, 47].

In dry sand, which is probably the most common noncohesive system, the contact forces are only repulsive. However, in wet sand, adhesion forces, and hence cohesive effects come into play [99, 154]. For larger grains, such as pebbles and boulders, these forces become less significant, still, moisture, inducing slippage and creeping, is crucial for geological processes leading to landslides and avalanches.

Grains of all sizes can be encountered outside of Earth too, for example in the planetary rings of Saturn [213, 160]. On interstellar scale, the aggregation process of dust leading to larger and larger particles and finally to planet formation [176] has many implications of the kinetic theory of granular gases [29].

The shape and surface roughness of particles forming granular systems can also vary on a large scale. The grains can be round, elongated, regular, irregular, etc. [57], and they can resemble spheres, ellipsoids, polyhedra, and other complex geometric shapes, while their surface can be anywhere between very smooth and very rough.

Taking for example the sand samples shown in Fig. 1.2, under a microscope we observe that the shape and the surface of the grains varies significantly from case to case as function of the geologically different places from which they are coming. Sand collected

Oahu, Makaha, Beach Park (USA, Hawaii)	Rio de Janeiro, Tititi'ca Beach (Brazil)	Grand Canyon, Colorado River (USA, Arizona)	Lombok, Kuta Beach (Indonesia)
Nova Scotia, Lockeport Beach (Canada)	Constanța, Neptun Beach (Romania)	Yallingup, Main Break Beach (West. Australia)	Isla Culebra, Playa Tortuga (Puerto Rico)
Istanbul, Yesilköy, Sea of Marmara, beach (Turkey)	Costa Blanca, Almeria, Mojacar, beach (Spain)	Cape Town, Blouberg Beach (South Africa)	Sicily, Santa Teresa di Riva, beach (Italy)
New Mexico, El Malpais, volcano (USA)	California, Fall River Mills, lava (USA)	Gran Canaria, Cald. Bandana, volcano (Spain)	Saint Maries, Emerald Creek (USA, Idaho)

Table 1.1: Places of origin of the sand samples presented on Fig. 1.2. From the collection of Loes Modderman (www.scienceart.nl).

from sea or large river beaches are usually made up of round grains with a smooth surface, while sand coming from mountains and volcanoes are typically composed of irregularly shaped grains with a rough surface.

In order to simplify the theoretical and experimental treatment of granular systems, in many cases idealized spherical grains with a sufficiently smooth surface (e.g. glass, polystyrene, or iron beads) are assumed. Despite of this simplification the complexity of their behavior is still very high.

A grand unified theory of granular materials currently seems almost impossible. In many cases, conventional concepts of statistical physics prove to be unsuitable for granular systems [61]. However, new ideas and new solutions emerge, which – beyond direct applicability to soils, seeds, or powders – give insight into seemingly different but equally challenging scientific fields such as the study of foams, dense colloids, dusty plasmas, suspensions, and ferrofluids.

Chapter 2

Piling, avalanches, and the effect of cohesion

Granular materials behave partly like fluids [113, 47, 185, 10]: They can flow and they can take up any shape imposed to them. However, they are unusual fluids as they can also maintain an inclined surface and they can form piles. In typical granular systems (e.g. in dry sand) in absence of external driving forces, metastable states far from equilibrium can exist for a very long time [47]. This is due to friction, which acts as a stabilizing force, and due to the insignificant thermal fluctuations, which cannot move the grains. When tilted more than a given limit, a granular surface becomes unstable and the grains start flowing in an avalanche lasting until the surface angle is sufficiently lowered and a new stable state is reached [136]. Both piling and the avalanche formation process strongly depend on the cohesion between the grains.

In what follows, we first review the general characteristics of a granular pile formed by noncohesive grains and show that it possesses an internal structure determined by a complex network of contact forces. We also discuss the dynamics of sandpile avalanches and the concept of self-organized criticality [13, 14]. The importance of this concept lies in the fact that it inspired the description of many slowly driven nonequilibrium systems which in a critical state, reached without the fine tuning of a control parameter, present a scale-invariant dynamics with power-law distribution of event sizes.

Later we turn to the question of how interparticle attractive forces such as cohesion induced by liquid bridges formed between wet grains [99, 154] influence the stability and the roughness of a pile's surface as well as the related avalanche dynamics. Another type of cohesive granular materials which we discuss are fine powders having grains smaller than approximately $250\ \mu\text{m}$. Even if they are dry and uncharged, fine powders are cohesive as a result of the van der Waals forces of quantum mechanical origin. This form of cohesion [33] is similar to moisture induced cohesion in many aspects, however, there are differences too. Discussing the behavior of dry fine powders, we also give a short outlook to triboelectric and electrostatic effects [45, 257].

At the end of this Chapter, we discuss the behavior of granular systems characterized by magnetic interparticle interactions. Magnetic granular systems exhibit a series of nontrivial structure formation effects [255, 20, 21, 246, 211] and can be viewed as a macroscopic model of dipolar fluids [48, 194, 138, 10] such as a ferrofluid. Recently, they have gained increasing attention. Systems of grains with controlled magnetization proved to be an efficient model for analyzing the transition of granular systems from noncohesive to

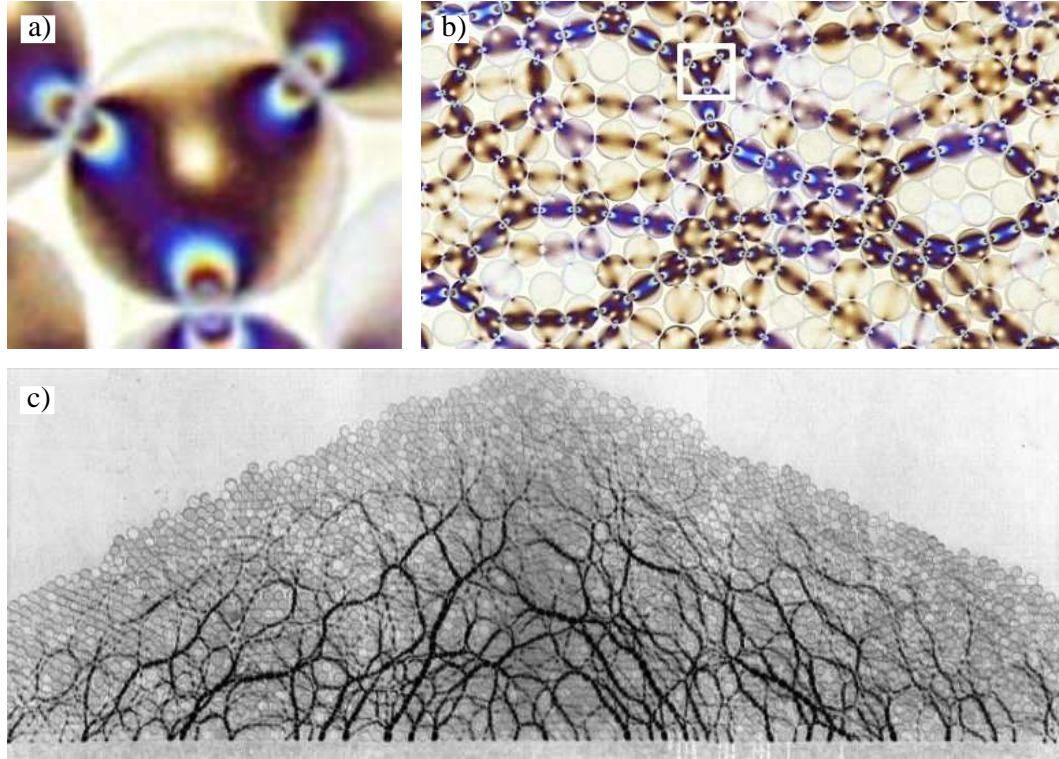


Figure 2.1: Network of contact forces: (a) distorted photoelastic disk, (b) force chains made visible [149], and (c) internal structure of a pile constructed by pouring grains on its top [89]. (Images reproduced with color inversion.)

cohesive behavior [82, 177, 71]. We focus mainly on this latter aspect, which is discussed in more details in Chapter 6.

2.1 Angle of stability

The angle of any granular surface is affected substantially by avalanche formation. By increasing the inclination angle, the stability of the grains decreases and at a characteristic angle, at the *maximum angle of stability* θ_m , the grains start moving. The formed avalanches carry away material and lower the surface angle until another characteristic angle, the *angle of repose* θ_r is reached. The same process can be initiated by adding grains on the top of a pile.

A grain falling on a pile can either find an equilibrium position, stop there, and thus increase the local surface angle, or, providing that the surface angle is already large enough, it can dislocate other grains, start an avalanche, and decrease the surface angle accordingly. The surface angles before and after avalanches are in general randomly distributed around θ_m and θ_r . Usually, for noncohesive grains the avalanches are restricted to a thin superficial layer of about 10 grains depth. In cohesive case both the pile's angle and the avalanches are affected by aggregation. We return to this question later on.

Due to the limiting angles θ_m and θ_r , the inclination of a granular pile's surface depends on how the pile was built. In most of the cases, the internal angle of a crater

formed when sand is allowed to flow out through a hole on the bottom of a box (such as in the *draining crater method*) is larger than the angle of a pile formed when sand is poured on a flat surface [92].

This dependence on construction history is explained by the “frozen” indeterminacy [238, 239] of the spatially correlated contact forces which form a complex network of chains [89, 149] (see Fig. 2.1). Another example on dependence on construction history is given by the stress distribution at the bottom of a pile. When built with pouring grains through a funnel – contrary to general expectations – this exhibits a minimum at the point where the pile’s height is maximal. This central pressure dip is missing if the grains were deposited with a sieve [245, 89]. Even if, geometrically, the two piles are seemingly identical, their internal structure is clearly different.

The force chains, with characteristic lengths of about 10 grain diameters, form the backbone of granular packings. The forces carried by different grains depend on the grain’s size [226]. Because some of the force lines propagate sideways and form arches [55], the weight of a granular sample poured in a container is partly supported by the side walls, and thus the pressure at the bottom of the container is not proportional to the filling height – as it would be for a fluid – but it saturates according to an exponential law. This phenomena was first described by Janssen in 1895 [114].

Based on the above properties, it is rather obvious that the presence of side walls (e.g. in a quasi-two-dimensional setup) can raise significantly the angle of a pile (up to about 20%) [92, 58]. The roughness of the base on which the pile was built does also increase the angle of stability [9] and the shape of the grains has a strong impact too. Identical cubic particles (such as bricks) could be used to build a vertical wall of certain stability, while this is almost impossible with spherical particles. The roughness and the size distribution of the grains affect the internal friction and the number of contacts, which, on their turn, can again increase a pile’s angle of stability.

2.2 Self-organized criticality

The avalanches on a sandpile can be small and restricted to only a few grains in the immediate vicinity of the initiating grain or they can be very large, spanning the whole system. This broad distribution of scales stimulated Bak, Tang, and Wiesenfeld [13, 14] to suggest a simple sandpile model for the general description of complex systems exhibiting large fluctuations (for a review see e.g. [233, 234]).

In their model, which is defined on a finite lattice, grains are dropped vertically one by one to random places where they form columns. Whenever the height difference between neighboring columns exceeds a certain threshold, grains fall from the top of the higher column onto the top of the lower columns. This can induce further instability and lead to an avalanche. The grains can leave the system at the boundary of the lattice, which results in a sandpile and avalanches “tumbling down” on its surface.

In the above “cellular automaton”, the size of the avalanches (determined by the number of grains set into motion) exhibits a power-law distribution of form

$$P(x) \propto x^{-\zeta} \tag{2.1}$$

with a characteristic exponent $\zeta = 1$, which is analogous to the behavior of a physical system near a critical point of a second-order phase transition. The only conceptual difference

is that the external tuning of a control parameter (such as temperature) is not needed, i.e. the system reaches the critical state in a self-organized way.

This *self-organized criticality* inspired the description of processes such as breakdown phenomena in semiconductors, turbulent systems, and earthquake dynamics, however, its general applicability is still a matter of debate, because many experiments on “real sandpiles” (see e.g. [111, 184, 63]) could not confirm the scale invariant distribution of avalanches. Feder [75] found that a stretched exponential of form

$$P(x) \propto \exp(-(x/x_0)^\gamma) \quad (2.2)$$

with γ between 0.34 and 0.44 can explain the data he analyzed. Currently it is widely believed that real sandpiles, showing hysteresis and features of a first-order phase transition, do not exhibit self-organized criticality in a strict sense [161, 10]. Several alternative theoretical descriptions based on dependence on packing density, stick-slip friction, and multiplicative processes were proposed [63, 140, 24, 185, 186, 10].

One of the problems which makes it difficult to relate theory to experiments is the fact that finite-size effects can have a strong impact on the results. In case of small piles, θ_m and θ_r are close to each other and one single grain can move the surface angle back and forth between the two limits [142].

Surprisingly, small piles are found to exhibit avalanches with power-law size distribution [98] suggesting self-organized criticality in accordance with the sandpile model of Bak et al. [13, 14], which, in fact, makes no difference between θ_m and θ_r . Power-law distributions were also found for small avalanches between large ones [28, 193] and for small-scale “landslides” of a watered granular mixture [212]. A model experiment of formation of river beds could also reveal the presence of dynamic scaling indicating that braided rivers may behave as self-organized critical systems [200].

Furthermore, it was shown that the shape of the grains can influence significantly the avalanche statistics. For rice grains with a large aspect ratio, evidence for self-organized criticality was found for two [86, 39] and recently also for three [2, 3] dimensional piles. Rice piles do also exhibit a roughening of their surface with a self-affine fractal structure [2, 3, 4], which is consistent with the theoretical mapping between self-organized criticality and roughening observed in the Kardar-Parisi-Zhang model [123, 175].

The type of the base on which two dimensional piles of steel balls are built with irregular and unstable profiles, was also reported [9] to have a strong influence on the scaling properties of the avalanche distributions. The induced profile disorder and the thickness of the grain layer involved in avalanches was found to lead to self-organized critical behavior, which could be approached choosing a suitable base.

In recent experiments, with uniform spherical glass beads dropped on a conical pile, Costello et al. [41] found a power-law behavior with an exponential cutoff. They have shown, that the exponential correction depends on the height from which the particles are dropped. This result further emphasizes that avalanche dynamics and the size distribution of the avalanches can depend on several factors¹, which disagrees with the postulated universality of the self-organized critical behavior [13, 14, 219].

Even if there are doubts that real sandpiles exhibit self-organized criticality in a strict sense, it is tempting to anticipate the existence of systems for which this concept is

¹Factors such as the system size, the shape of the grains, the irregularity of the internal structure of the pile, and also the way the grains were dropped on the pile.

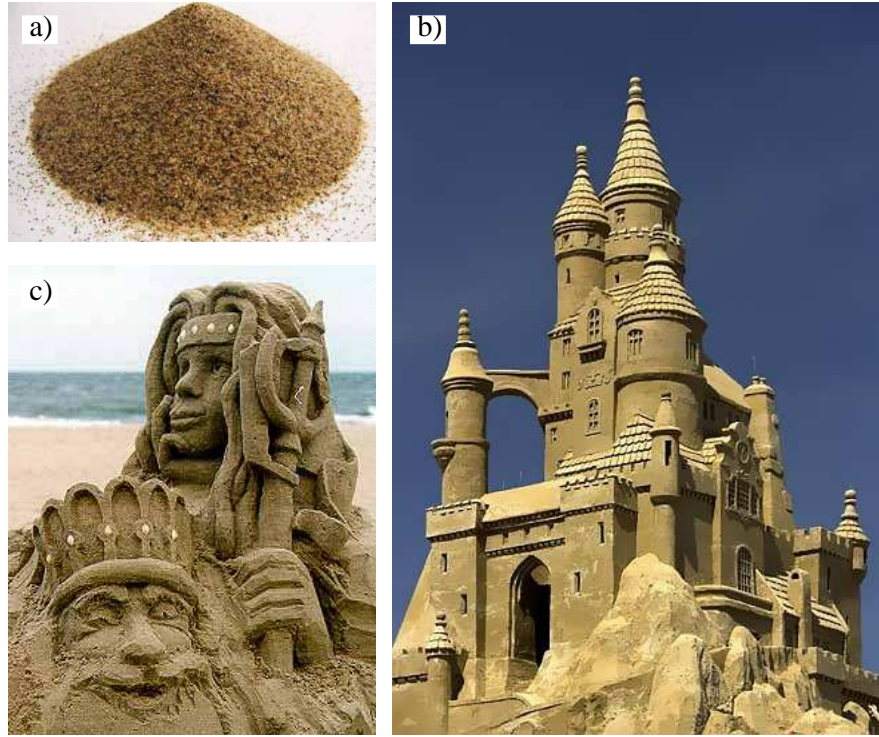


Figure 2.2: (a) A pile of dry sand, (b) a fairytale castle built of wet sand (Nils Bergmann, Sand World 2005, www.sandworld.de), and (c) a sand sculpture with fine details (Damon Farmer, Neptune festival 1997, www.sandhands.com).

suitable, at least as a source of new ideas. Such a system is given for example by magnetic vortices in superconductors, which, based on various criteria, show signs of self-organized critical behavior [5]. More examples from physical, biological, and social sciences, are given in [234] and in references therein.

2.3 Moisture-induced changes

Some time ago Hornbaker et al. [105] addressed the question of how sandcastles stand. It is obvious that dry sand is not suitable for building vertical walls, towers, and arches needed for any decent sandcastle, as gravity tends to flatten these structures, however, a small quantity of wetting liquid can make miracles. Building sandcastles of fine details (see Fig. 2.2) seems to be reserved for artists (and children) capable of creating exceptional artworks on the beach (or in a sandbox), but it is well known that moisture-induced effects are extremely important in real geophysical applications too. Halsey and Levine [94] addressed the question of how sandcastles fall. The importance of moisture-induced changes in granular materials (and soils) cannot be overestimated: Landslides associated with periods of heavy rainfall or rapid snow melt cause globally billions of dollars in damage and thousands of deaths and injuries each year.

In a simplified setup, adding small quantities of oil to spherical polystyrene beads, Hornbaker et al. [105] demonstrated with a draining crater method that the particles tend to aggregate and the angle of repose of a pile increases nearly linearly with the liquid

content (up to a certain value where the size of the formed clusters approached the size of the draining aperture and draining was no more possible). They argued that the surface tension of the liquid forming “bridges” between grains at contact points lead to finite range attractive forces [206] responsible for cluster formation and the increased stability.

Albert et al. [7] explained the findings theoretically using a surface stability criteria based on geometrical considerations. An alternative explanation based on more elaborate stability arguments and the Mohr-Coulomb theory adopted from soil mechanics [163] was proposed by Halsey and Levine [94]. They found that as a result of adhesive forces the failure leading to avalanches occurs within the bulk of the pile rather than at its surface. Further results on moisture-induced ageing and on kinetics of capillary condensation, obtained with similar methodology, were presented by Bocquet et al. [22]. Both Halsey and Levine [94] and Bocquet et al. [22] concluded that the strength of the capillary bridges is controlled by the surface roughness of the grains.

In experiments, using a similar technique to the one applied by Hornbaker et al. [105], (i.e. with the draining crater method) Tegzes et al. [221] performed detailed measurements of the angle of repose as function of the added liquid content and the sample size in order to test the validity of the above theories. The angle of repose was first observed to increase with the liquid content and then it saturated. Tegzes et al. [221] identified three distinct regimes as liquid was added: (1) a *granular regime* in which the grains move individually, (2) a *correlated regime* in which the grains move in correlated clusters, and (3) a *plastic regime* in which the grains flow coherently. It turned out that the surface stability criteria of Albert et al. [7] describes the behavior of the granular regime, while the Mohr-Coulomb theory proposed by Halsey and Levine [94] works for the correlated and the plastic regimes. Yet, deviations and quantitative disagreement from both theories exist.

Several other studies [85, 152, 162, 199] were devoted to humidity effects and stability of granular piles. In one of these, Samadani and Kudrolli [199] studied the effect of interstitial fluid on the angle of repose of spherical glass beads poured into a quasi-two-dimensional box. Besides surface tension, the viscosity of the fluid is found to have an effect on the angle of repose. In accordance with the results of Tegzes et al. [221], the angle of repose first increased with the liquid content and then it saturated. The saturation value was found to increase with the viscosity and also with the size of the particles. Samadani and Kudrolli [199] argued that the saturation occurs at a higher liquid content than estimated based only on particle roughness. Besides, as a result of particle aggregation controlled by liquid bridges, the surface of the pile was found to become rough as the fluid content increased. At same liquid content, the smaller particles clumped more than larger ones, therefore the roughness of the surface was greater for smaller particles.

Briefly, the behavior of wet granular media proved to be richer than anticipated by early results based either on discrete geometrical stability of the grains on a pile’s surface [105, 7] or on continuum models of failure within the pile [94, 22]. The former approach seemed to be more appropriate for small quantities of wetting liquid, while the latter described better the case of high liquid contents. Experiments [221, 85, 152, 162, 199] revealed that the results can depend on the dimensions of the system (the larger the sandcastle, the greater the chances of failure), the nature of the liquid, such as surface tension, viscous damping, and lubrication, as well as the size and surface of the grains. Moreover, the distribution of liquid on the surface of the grains can change with time [22, 188], which can further complicate an already complicated case.

Ideas which seemed to be conflicting for a long time [204] were recently unified in

a hybrid “theory of sandcastles” by Nowak et al. [167]. Their theory, developed for the description of the maximum angle of stability of a granular pile, combines surface stability considerations with the nature of failure within the pile. The theory can *quantitatively* account for experimental data over a broad range of parameters, including different interstitial fluids, as well as system and grain sizes.

Recent experiments with wet granular materials focus mainly on dynamic effects such as avalanches and the dynamics of grain flows [87, 223], the fluidization of vibrated grains [107, 203], and the segregation of grains having different sizes [198, 199, 139]. Tegzes et al. [222, 223], adding liquid to a granular material, in a series of experiments using a rotating drum apparatus (consisting of a cylindrical chamber partially filled with grains and rotated around a horizontal axis) studied the effects on avalanches. No self-organized criticality was reported. Instead, it was found that the liquid-induced cohesion can lead to the development of a correlation length that spans many grain diameters. Tegzes et al. [222, 223] observed formation of clumps with a characteristic size and smooth flow at high liquid content. They quantitatively analyzed the time evolution of the surface profile and the surface velocities during continuous flow. The same granular, correlated, and plastic regimes could be identified as in their previous work [221]. These results show connections with other correlated systems of hard condensed matter [204].

The importance of the structure of the network of capillary bridges and their changes upon shearing, as well as their connection with mechanical properties of wet granular materials, is also studied extensively (see [84, 99] and the references therein). Recent advances in the physics of wet granular materials is reviewed by Mitarai and Nori [154]. They also list several open problems such as jamming, statistical mechanics approach, arches and contact-force fluctuations, numerical simulations, mechanical properties of snow, and simple experimental setups used to study the dynamics of wet granular media.

2.4 Dry fine powders

For beach sand, with medium grain sizes of $0.25 - 0.5\text{ mm}$ (or larger), the van der Waals forces are negligible. These attractive forces arise from the collective interaction of atoms and molecules through fluctuating dipole-dipole fields [110]. For atoms and molecules it decays as $1/r^6$ (where r is the interparticle separation), while for macroscopic particles, closer to each other than 100 nm , it falls off as $1/r^2$. At larger distances, its strength diminishes very rapidly. The van der Waals force can be considered effectively a force with a finite range of about 100 nm with strength increasing linearly with particle size [110, 97, 83]. The inertial force arising from particle weight increases as the cube of the particle size, therefore, the effects of the van der Waals force are seen only for closely packed fine powders with small grains of micron and sub-micron size. Fine corn flour and icing sugar, or xerographic toners composed of polymer particles, even if they are dry and uncharged, are typically cohesive as a result of this force.

Particles larger than approximately 0.25 mm under normal gravity settle with roughly the same porosity. Fine powders, with smaller particle size, experience a significant increase of the adhesive forces as the particle size decreases. The adhesive forces become so much stronger than gravity that very loose packing structures form and the porosity increases (see Fig. 2.3). Contrary to coarse grained granular materials, compaction of fine powders can significantly decrease the average interparticle distance, and hence it can increase the



Figure 2.3: Dry fine powders of the same material and the same total mass, but with different particle sizes. The samples are poured into cylinders of the same size. The labels show the particle size in micrometer. (From the PhD Thesis of D. Kadau [121].)

adhesive forces by several orders of magnitude. On the other hand, large asperities of the grains decrease the local radius of curvature at contact, and thus lead to smaller adhesion forces [97, 83]. Fine powders with irregularly shaped particles flow better than powders with smooth and round grains. In many industrial applications, e.g. in production of xerographic toners, hard nanopowders are used to coat grains of micron size in order to reduce cohesion and to control their flow properties [33]. Puffball spores use the same mechanism to get easily dispersed in the air.

In cohesive systems, as the ratio of interparticle force to particle weight² increases, the tendency of particles to aggregate becomes more and more dominant. Capillary forces in wet sand can exceed the particle weight in 2 to 3 orders of magnitude [206]. For fine powders the van der Waals force can be up to 4 orders of magnitude higher than the particle weight [244]. Because of the dominance of adhesive forces over particle weight, these materials behave partly like wet sand. Fine powders form piles with a high angle of stability, fracture before breaking, and form avalanches and flow in coherent blocks. However, due to extreme sensitivity to interstitial gas flow, fine powders transit directly from plastic dense flows to fluidization without passing through collisional regimes with negligible gas interaction [34, 35]. The absence of such inertial regimes makes them qualitatively different from coarse granular materials. (For a recent review see [33].)

Valverde et al. [243] investigated the onset of avalanches while tilting a bed of uncharged dry fine cohesive powder (xerographic toner of particle diameter of about $10 \mu\text{m}$). They have shown that adhesion, originated from van der Waals forces, causes the site of failure to move deep into the bulk of the material. This is explained by formation of large scale semicoherent granular clusters. They found that the depth of avalanches increases with the bed width and is of several millimeters, which is very large compared to a particle diameter, contrary to the noncohesive case, in which the avalanches are restricted to a

²This *interparticle force ratio* resembles the Bond number defined in fluid mechanics, so by analogy is sometimes referred to as the “cohesive granular Bond number” [162].

thin superficial layer [112, 113, 10]. The angle where avalanches are started can achieve even 90° for very narrow beds, however this decreases with increasing separation of the retaining walls. Valverde et al. [243] explained their data with a theory based on a generalized version of Coulomb's method of wedges [163] appropriate for granular materials in high cohesion regime. This analysis shows that cohesion and boundary conditions play a fundamental role in avalanches of dry fine powders.

A common tool to analyze the behavior of powders is the rotating drum apparatus. Such equipment, which consists of a horizontal cylindrical device rotated around its axis, is commercially available and widely used to evaluate the flowability of powders and to predict their behavior under industrial conditions [125, 134]. In fine powders, strongly disordered regions of varying degrees of consolidation are very typical. In a rotating drum, the distribution of disordered regions changes randomly after each avalanche and the free surface of the material is also very rough. Furthermore, the motion of the particles is constrained by adhesion forces, which increases the dissipation and counteracts the effect of inertia. In such conditions, slightly cohesive powders are similar to rice grains of strong anisotropy for which self-organized criticality was found [86, 3]. All these effects are expected to lead to very broad distribution of avalanche sizes, and thus fine powders, at least in certain conditions, should exhibit self-organized criticality.

Quintanilla et al. [183] addressed the above question in experiments with slowly rotating drums. Their results show that avalanches of slightly cohesive dry fine powders do not behave in a self-organized critical manner. The avalanche sizes and the time interval between avalanches do not follow a power-law distribution, but they scale with powder cohesiveness. At low cohesion the avalanches occur quite regularly, with nearly uniform size and time spacing. At larger cohesion, when the flowability of powders decays, the time spacing and the size of the avalanches show a noisy behavior. The time interval between avalanches presents a peak correlated to cohesiveness. The avalanche sizes, their time spacing, and the angle of stability are on average increasing with cohesion.

In addition to the van der Waals forces, cohesion and aggregation can be also induced by electrostatic charges. Whenever dry insulating granular materials are exposed to driving forces (e.g. when powders are stirred or shaken) triboelectric charging of the grains is inevitable [118, 220]. The influence of electric charges is expected to play an important role especially when the particles are small. In natural phenomena, this applies for example to small ice particles in thunderclouds (cumulonimbus) associated with thunderstorms and lightning, or to eruption of volcanos, where triboelectric charging produces enormous electrical fields. In general, any handling of fine granular materials is to some extent accompanied by electrostatic phenomena [147], even in the case of powder suspensions in a nonpolar liquid [258, 257]. For a recent review of very promising results on electrostatically charged granular matter see [45] and the references therein.

2.5 Magnetic systems

Magnetic systems are important for industrial applications such as high precision industrial printers based on magnetic toner particles controlled by an external magnetic field [209]. Several interesting effects were reported for monolayers of magnetic particles subjected to vibrations [214, 215, 20, 21] and periodic electrostatic and magnetic excitations [211], which can be considered an extremely simplified model of ferrofluids.

For vertically vibrated spheres, Stambaugh et al. reported that magnetic granular materials show pattern formation [214] and segregation [215] due to differences of the strength and the shape of the dipole field of the components. Blair et al. [20, 21] observed a rich variety of structures (clusters, rings, chains, and networks) and have identified *gas*, *clustered* and *network* phases, which the system experiences at different vibration intensities relative to the strength of the dipolar interactions.

For small particles fluidized with electrostatic and magnetic excitation, Snezhko et al. [211] observed the formation of similar structures and a sharp transition from chains to the network phase. In the limit where the dissipative interactions can be reduced to zero, such magnetic granular systems can be mapped to the *dipolar hard sphere* model [48, 194]. Using this model, some of the observed structures can be understood, however, the phenomena show deviations from this model and indicate a deep implication of the dissipative nature of the particle collisions.

The study of spatial configurations of dipolar particles forms an important issue concerning the physics of electro and magnetorheological suspensions. Martin et al. [151] have shown that stable classical molecules and particle foams exhibiting a large variety of morphologies can be created with the simultaneous application of magnetic fields along three orthogonal axes. Butter et al. confirmed the existence of dipolar chains [31] in ferrofluids using cryogenic electron microscopy. Theories [48, 194] predicted that such systems separate into coexisting liquid and gas phases. However, because weakly interacting chains of aligned dipoles competing with closed rings and clusters [255, 127, 128, 20, 246] complicate the situation, the nature of this transition is still debated [137, 138, 10].

The effects of cohesion on granular materials have been studied mainly in form of moisture-induced changes and through the influence of van der Waals forces on dry fine powders. In neither case is easy to study the transition from noncohesive to cohesive behavior. For example, it is difficult to achieve an exact degree of humidity with a uniform distribution [221, 85]. Moreover, it is problematic to relate experimentally the liquid content to the strength of the interparticle forces induced by liquid bridges [206, 154]. Preparing samples of fine powders with controlled and uniform cohesiveness is not easy either [34, 35]. The cohesion of dry fine powders depends on the size of the particles and their surface roughness, which is difficult to be set to a required value. The influence of the surrounding gas and electric charges make the situation even more complex [33]. The interaction with the walls of the container in which the material is placed can affect the results in a nontrivial manner for both wet granular materials and dry fine powders. The initial conditions, such as packing and internal structure due to force chains, can also depend on the strength and the nature of the cohesion [76, 260].

Because of the numerous factors which make the study of wet granular materials and dry fine powders at different controlled levels of cohesion difficult, Forsyth et al. [82, 108] suggested a method based on magnetized particles. Their method is useful especially for analyzing the transition of granular systems from noncohesive to cohesive behavior. They adopted the widely accepted idea that – independent of its physical details – competition between interparticle forces and inertial forces is the main factor which determines the behavior of cohesive granular materials.

In their experimental setup, iron spheres placed in a static homogenous magnetic field become magnetized and all acquire a magnetic dipole oriented parallel to the field. Because iron particles are magnetically linear, the arising dipole-dipole interaction forces, which are in overall attractive, are proportional to the square of the applied field [119, 82, 108].

Varying the strength of the field allows to continuously vary the strength of the interparticle forces and hence the level of cohesion. Using nonmagnetic perspex walls, the particle-wall interactions remain the same as in noncohesive case, and thus it is ensured that additional effects of nontrivial magnetic origin are excluded. Particles under same packing conditions with cohesiveness set later guarantee that the initial configurations are as well-defined and uniform as possible.

With all the apparent advantages of the method based on magnetized particles, it is evident that in some aspects magnetic systems are different from both wet granular materials and dry fine powders. One main difference – of assumed importance – is the fact that the magnetic dipole-dipole interactions are long-ranged and anisotropic, rather than finite-ranged and invariant to the orientation of the grains, such as the van der Waals forces or the point to point attractive forces induced by liquid bridges. The anisotropy of the system is further increased by the fixed external field, which forces the dipoles to be aligned to its direction. As a consequence, when the line joining the centers of two particles is parallel with the field, the dipoles attract each other and they repel when this line is perpendicular to the field. In a random arrangement, the average force exerted by two particles on each other is less than the maximum force arising from the most favorable head-to-tail alignment, and thus the ratio of the maximum interparticle force and the average particle weight – a straightforward way to quantify the degree of cohesion – overestimates the real cohesiveness.

In spite of the strong anisotropy and the long interaction range, the results of Forsyth et al. [82, 108] show many conceptual analogies of magnetic systems with both wet granular materials and dry fine powders. In a series of experiments, under magnetic fields of different strengths, Forsyth et al. [82, 108] have poured grains through a funnel into a quasi-two-dimensional box and measured the static angle of repose of the formed piles. They have also executed experiments with a rotating drum apparatus, setting the rotation speed of the drum to a value at which the surface of the tested material was in constant motion with a well-defined dynamic angle of repose. The results show that both the static and dynamic angle of repose increases proportional to the square of the applied magnetic field, which corresponds to a linear dependence on the strength of interparticle forces. This result is in good agreement with the behavior of wet granular materials, for which a similar dependence was reported at small quantities of wetting liquid [105]. When more liquid was added and the interparticle forces increased accordingly, a saturation of the angle of repose was observed [221, 199, 167]. For magnetized grains, such saturation was not found by Forsyth et al. [82, 108]. This could be caused by the fact that the applied magnetic fields, and hence the interparticle forces, were not strong enough.

Hutton [108] presented additional details and also examined the surface roughness of granular piles built of magnetized grains, showing that the roughness increases with increasing cohesiveness. In another study, Forsyth et al. [81] presented the effects of magnetic interparticle forces on the packing of magnetized iron beads. They compared the results with other types of cohesive systems and found good agreement with the behavior of dry fine powders dominated by van der Waals forces [83]. In a further study [80], they have examined the flow properties of wet granular systems and compared the results with the flow properties of magnetized iron beads. They reported a critical interparticle force ratio at which the system undergoes a transition from free-flowing to stick-slip behavior. This transition could correspond to the transition of wet granular materials from granular regime to correlated regime [221]. Hutton et al. [109] recently presented results on

avalanche stratification and segregation in rotating drums. Their results – important for applications mixing cohesive powders – show that interparticle forces can induce mixed granular materials to segregate and segregating materials to mix.

Extending the results of Forsyth et al. [82, 108], Peters and Lemaire [177] have shown that the stability angle of quasi-two-dimensional piles formed by magnetized iron beads depends on the direction of the external magnetizing field. When the field applied parallel to the plane of the cell is vertical or horizontal, the angle of stability is approximately the same, however, it increases when the field is roughly parallel with the surface and it decreases when it is perpendicular to it. In order to reduce this anisotropy, Peters and Lemaire [177] proposed a rotating external field. Using a rotating field, the angle of stability was again found to be proportional to the square of the field intensity, which corresponds to linear dependence on the strength of dipole-dipole forces. However, a closer look to the results indicate small deviations from this linearity. According to Peters and Lemaire [177], at small magnetic fields (much smaller than those used by Forsyth et al. [82, 108]) the dependence of the angle of stability on cohesive interparticle forces is slightly sublinear. Peters and Lemaire [177] studied also the difference between the angle of repose and the angle of stability and noticed a dissimilar dependence on the applied field, the former being less sensitive to the degree of cohesion.

A short time before Forsyth et al. [82, 108], Hutton [108], and Peters and Lemaire [177] published their results, Szalmás et al. [217] had already built a similar experimental setup and studied the avalanches of magnetized particles dropped into a quasi-two-dimensional box. Yet, most of their results remained unpublished. In their setup, an external magnetic field was not applied during the experiments, instead the particles carried a remanent magnetization accumulated before they were dropped into the test cell. Some observations of Szalmás et al. [217] indicate that this setup is more favorable than those suggested by Forsyth et al. [82, 108] and Peters and Lemaire [177], because the anisotropy is smaller. However, in this case the exact magnetization of the grains, and thus the cohesiveness, becomes more difficult to control. The few available results of Szalmás et al. [217] show qualitative agreement with the presumed general behavior of cohesive systems. In particular, their results present experimental evidence for the existence of a characteristic avalanche size which increases with cohesion.

Chapter 3

Strain localization and the packing density

Granular materials are able of withstanding shear stress. This property gives them a solid-like behavior. However, when dry granular materials are subjected to slow deformations, unlike in usual solids, the strain is localized to narrow domains called shear bands [259, 102]. The shear bands destabilize the force chains forming the backbone of granular packings and lower the load bearing capacity of the material. Under further stress the deformations can amplify and can lead to a complete breakdown of stability. Strain localization, as well as strain softening followed by failure, is responsible, among others, for processes such as landslides and avalanches.

One of the main properties of granular materials, which seems strongly linked to strain localization, is their packing density. Dense systems must expand in order to undergo shear deformations [189], while due to shear induced rearrangements loose systems move towards denser configurations [261, 227]. Based on several observations [32, 266, 178, 50, 17, 195], it is widely assumed that strain localization generates a unique packing state independently of the initial conditions. At this “critical” packing density the material can be deformed without any further volume change.

Strain localization and associated effects [102, 106, 158, 227, 95, 228, 207] are important for many classical fields of engineering, including, but not limited to, geotechnical, earthquake, and mining engineering. Understanding the underlying mechanisms and the properties of shear bands are crucial for predicting the stability of granular packings and for describing the strongly inhomogeneous deformations which can suddenly destroy these fragile states of matter. In this respect, finding a suitable mathematical description of the stress transmission properties of granular assemblies exposed to various boundary conditions seems to be a fundamental aim [201, 25, 62, 23, 90].

Soil Mechanics and related engineering fields usually adopt a continuum approach based on constitutive models [205, 132, 259]. However, the currently available models of soils are only descriptive and leave unanswered questions concerning grain scale dynamics. In many cases, it is difficult to relate the model parameters to soil properties. Furthermore, they are far from being general and widely accepted. Usually different models are developed for different types of soils and different behavior [126]. The predictive power of these is often restricted to the targeted specific phenomenon.

In this Chapter, we first give a short overview of the general properties of shear bands and related phenomena, then we turn to granular packings and discuss the assumed

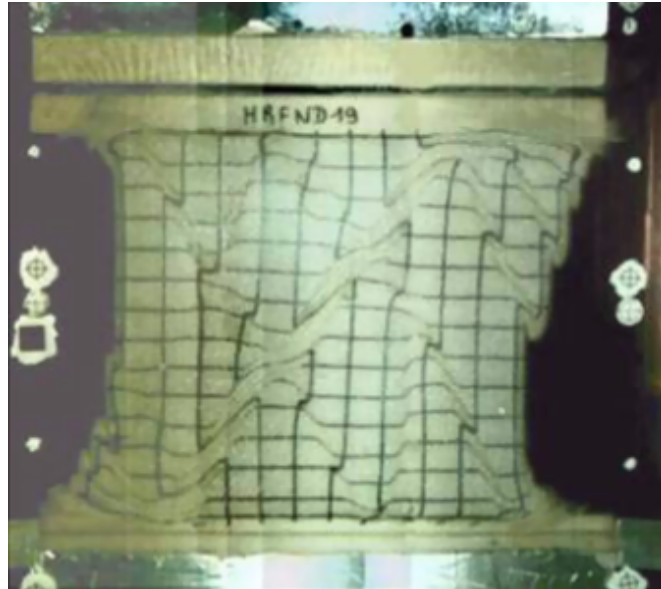


Figure 3.1: Shear bands in a sand sample distorted in a biaxial shear tester. (Jaques Desrues and co-workers [52], Laboratoire 3S, Grenoble, France.)

“criticality” of strain localization. At the end of this Chapter, we outline some recent experimental results obtained in triaxial shear tests, one of the most interesting and most complex techniques used to study the properties of soils and the effects of strain localization in granular media. We focus mainly on shear band morphologies and on changes in packing density. These topics are further developed and extended in Chapter 7 and 8.

3.1 Shear bands

The first study of shear bands dates back to the nineteenth century [189] and since then it has been investigated in many different geometries and specially designed laboratory tests [179, 130, 207, 52]. Within sheared granular samples a reach variety of phenomena such as dilation or compaction, slow relaxation, segregation, rotation of the grains, as well as nontrivial density and velocity profiles can be observed [1, 100]. The experimentally found shear band morphologies (for an example see Fig. 3.1) and the internal properties of shear bands are presently far from being understood.

Strain localization in loose granular materials is modeled by evolving shear bands, which can change their positions as the system slowly deforms, but the existence of such shear bands is not at all a triviality [228]. In dense granular samples, the location of the shear bands is usually fixed. The orientation of these bands depends on the friction between the grains. A simple theoretical description of this is given by the Mohr-Coulomb theory, however in many cases corrections are needed [259, 130]. Based on theoretical considerations, Unger [236] suggested that shear zones are refracted at material interfaces of different packing density in analogy with refraction of light beams in optics.

Sand microstructure characterized by grain size distribution and degree of uniformity can in general greatly affect shear banding characteristics, although the orientation of shear bands was found to be mainly independent of these factors [249]. Furthermore,

many observations show that shear bands in conventional granular systems have a width of about 10 grain diameters independently of grain size [249]. This seems to be sustained by theoretical considerations too [1, 100].

Among experimental arrangements [207] used to study sheared granular materials, Couette cells [247, 157] are maybe the most simple and the most popular ones. In this setup, the material is continuously sheared between two concentric cylinders rotating compared to each other. Shear bands are usually formed close to the inner cylinder. Experiments using the Couette geometry revealed intermittent long radial force chains in loose packings and a tangled network of force chains in dense systems, with a continuous transition between the two [106]. Since the network of force chains is sensitive to grain rearrangements, sheared samples exhibit strong stress fluctuations [248].

A modified Couette cell [78, 77], having a bottom split into an outer ring and a stationary disk in the center, provides a shear band of nontrivial shape far from the confining walls. The shear band starts at the perimeter of the stationary bottom disk and extends through the material, delimiting an inner and an outer part. The outer part rotates around the inner part. Depending on the height of the sample, the shear band can either reach the surface of the specimen or close within it [38]. The shape of the shear band could be explained based on the principle of least dissipation [240].

Engineering investigations use standard experimental setups based on plane strain, biaxial, and triaxial arrangements. They focus mainly on the load bearing capacity of soils and on identifying the stress-strain relation characteristic to the tested particular soil [130]. For an example of shear bands obtained in a sand sample undergoing a biaxial shear test see Fig. 3.1. We do not attempt a full review of the engineering literature because this goes beyond the purpose of this work. However, we summarize some recent results obtained in triaxial shear tests in Section 3.4.

3.2 Granular packings

The problem of packing objects in compact configurations has implications for a broad range of scientific disciplines including granular media and discrete geometry, as well as glass formation and properties of ceramics. In our daily lives, stacking fruits, vegetables, or cannon balls is usually done by preparing a bottom layer consisting of objects arranged closely in a triangular lattice and fitting each next layer in the hollows of the layer below. In 1609, Kepler suggested that for identical spheres this face-centered cubic (FCC) packing, which fills the space with a volume fraction of $\eta = \pi/(3\sqrt{2}) \approx 0.74$, is the most compact of all possible arrangements.

Even though, intuitively, this has been known and applied since antiquity, it turned out to be hard to confirm it with mathematical certainty [40, 12, 254]. For a periodic packing, it was first proved by Gauss in 1831. One century later, in 1953, László Fejes Tóth succeeded to reduce the conjecture to a series of numerous special cases, suggesting that computers can be used to finish the proof. Thomas C. Hales has recently worked out a strategy which implemented this approach [93].¹

Different random arrangements have much lower densities than the crystalline FCC packing [40, 12]. Experiments and computer simulations revealed that the largest obtain-

¹The referees of Hales's work agreed that the correctness of the method is 99% sure, hence the Kepler conjecture has almost certainly been proved.

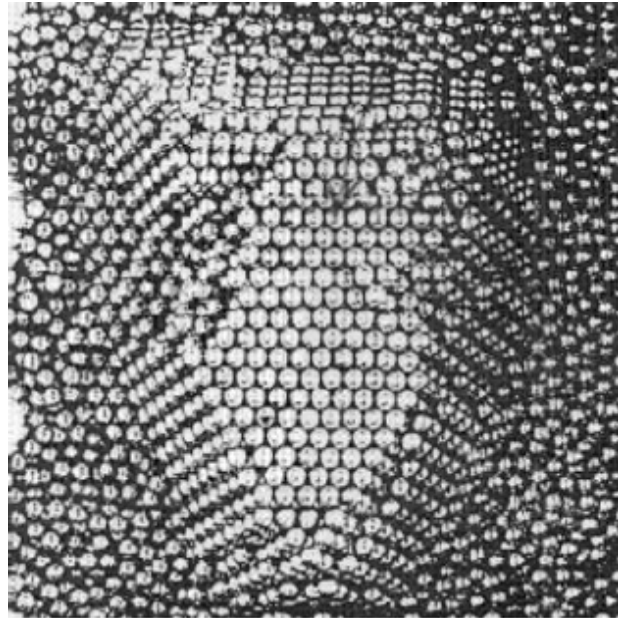


Figure 3.2: Packing of steel beads: A crystalline packing ($\eta \approx 0.74$) on top of a random close packing ($\eta \approx 0.64$) [19, 37].

able volume fraction of randomly placed identical spheres is around $\eta = 0.64$ [208, 11]. This is known as the *random close packing* (RCP) limit (see Fig. 3.2). A mathematically precise definition of this limit can be given through the concept of *maximally random jammed* state [230], however, this is still open for investigation [122, 170].

Reaching the RCP limit needs careful preparation such as simultaneous tapping and compression. If glass or marble beads are simply poured into a container, the volume fraction is usually only around $\eta = 0.6$ [208]. A *random loose packing* (RLP) at its limit of mechanical stability obtained by immersing spheres in a fluid and letting them settle has a volume fraction of $\eta = 0.555$ [171].

The different volume fractions of loose random packings obtained with different preparation methods, in both experimental and numerical approach, testify that the RLP limit is even less well defined than the RCP limit. Attempts made in order to relate the RLP conditions to the dilatancy onset and to rigidity percolation [171], as well as to the still debated transition from liquid to glassy state in hard sphere systems [265], show the complexity of this packing limit.

The situation is further complicated by the fact that the packing fraction of grains is affected by friction [262] and cohesion [76, 81, 260, 54, 242]. Zhang and Makse [262] have shown that for infinitely rough cohesionless particles the packing density of a loose system can be as low as $\eta = 0.554$, even if the gravity is dominant. For frictionless particles no significantly looser packing can be obtained than $\eta = 0.64$ [262, 169], meaning that in this ideal case the RLP and RCP states are very close to each other.

In case of cohesive grains interacting with strong van der Waals forces, the packing density decreases with increasing strength of the interparticle force, approaching zero when the cohesion is infinitely strong [54, 242]. The same behavior is expected to govern the packing properties in the case of other types of cohesion such as cohesion induced by capillary [76, 260] or magnetic [81] forces.

Another astonishing aspect of the packing property of granular materials is the strong dependence on the shape of the grains [254]. Recent experimental and computational results [53] demonstrate that the packing density of non-spherical grains can be significantly larger than the packing density of identical spheres. Surprisingly, the packing property of spheres is the exception rather than the rule. Results obtained for ellipsoidal objects – M&M’s chocolate candies [53], in fact – suggest that the value of the RCP volume fraction of irregular objects is around $\eta = 0.72$. This drops sharply to 0.64 as the shape approaches spherical symmetry.

This behavior can be understood based on a simple argument: The forces exerted by neighbors on a perfect frictionless sphere cause only translation, while on an irregular object it can also cause rotation. To ensure that all the forces and torques sum up to zero, on average, larger number of neighbors are required for irregular objects than for spheres, which in turn requires a higher volume fraction. Indeed, the average number of contacts per particle – the coordination number – for ellipsoids was found to be $Z = 10$, while this is only $Z = 6$ for spheres.

The volume fraction η of a granular packing gives a direct measure of the packing density. In engineering fields such as soil sciences, geology, and hydrogeology, instead of η the void ratio $\nu = 1/\eta - 1$ or the porosity $1 - \eta$ is used more often. There are many experimental techniques which can measure these quantities. The most simple way to determine the overall packing density of a granular sample is to measure its weight and volume and compare the ratio of these two with the material density of the grains. More sophisticated techniques such as Magnetic Resonance Imaging, X-Ray Radiography, and Computer Tomography can measure the packing density locally.

3.3 Criticality of strain localization

Walking on the beach, the surprising effect can be observed that wet sand dries out around one’s feet [113]. This is due to the pressure exerted on the ground, which causes the sand to expand and the water to drain away. As a general observation, dense granular samples dilate under distortions [189]. At the same time, experiments [261, 166] and theoretical considerations [146, 227, 228] reveal that loose samples densify during continuous shearing. The above findings suggest that at a specific density granular materials could be deformed without changing their volume.

This specific packing state, in accordance with experiments [32, 51, 50, 8, 17], mathematical models [178], and computer simulations [266, 195], seems to be reached, independently of the initial packing conditions, as a result of strain localization. It is widely assumed that a slowly driven granular system “self-organizes” its packing density to a “critical” value [155]. This hypothesis formulated a long time ago by Casagrande [32], forms the basis of many continuum constitutive models of Soil Mechanics [205], however, the nature of this property is not yet clearly understood. Currently, it is not known whether the spontaneously reached unique state of a slowly deformed granular system is really a *critical* state in a statistical-physical sense or not.

Mapping an oversimplified mathematical model of sheared granular media to a well-understood percolation model, Piccioni et al. [178] suggest that the packing state reached during strain localization exhibits a power-law behavior, although this has not been demonstrated in experiments or more realistic models. Evesque [63] introduces a new aspect by

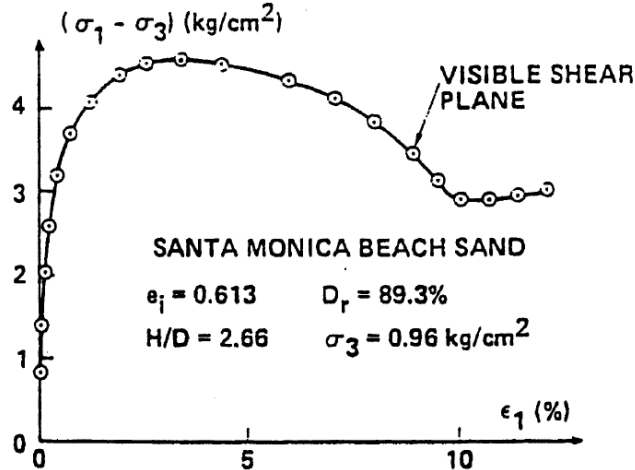


Figure 3.3: Experimental stress-strain relation from a triaxial compression test exhibiting strain softening and development of shear plane. (Courtesy of Poul V. Lade [130].)

making a connection to avalanche formation mechanisms. He suggests that avalanches appearing on sand piles exhibit self-organized criticality if and only if the packing density of the pile is at a critical value coinciding with the critical density developed during strain localization. This result needs further investigations too.

Zhang and Makse [150, 262] have recently presented results on the jamming transition of granular materials. The importance of these findings lie in the fact that jamming [141, 231, 190] is a concept which can connect granular matters with a variety of other systems including dense particulate suspensions exhibiting a diverging viscosity at a given packing fraction [216, 174]. As far as jamming of infinitely rough grains and strain localization in the same limit are related, the critical density reported by Zhang and Makse [150, 262] makes the picture even more complex.

In spite of the above results, according to general opinion, the critical behavior of a granular system, manifesting itself in strain localization and a specific packing density reached spontaneously during this process, is not *self-organized criticality* in a strict sense [13, 14] (see Section 2.2). In strain localization, clear evidence of a continuous phase transition exhibiting a broad distribution of scales has not been found.

3.4 Triaxial shear tests

Triaxial shear tests [96, 131, 52, 50, 17] are usually performed to obtain mechanical properties of soils. A triaxial shear test usually consists of a cylindrical specimen surrounded by a rubber membrane and placed between two platens closing off the top and the bottom ends. The platens can either tilt or have a fixed orientation. An external lateral confining pressure is applied on the sample by placing it into a bath of water or by creating a relative vacuum inside the system. The end platens are driven mechanically along the axis of the cylinder – usually with constant velocity or constant force. A constant velocity induces constant strain, while a constant force assures constant stress.

During the experiments, the force resulting on the platens or the displacement rate of the platens as well as the volume change of the specimen is recorded. To measure the upper

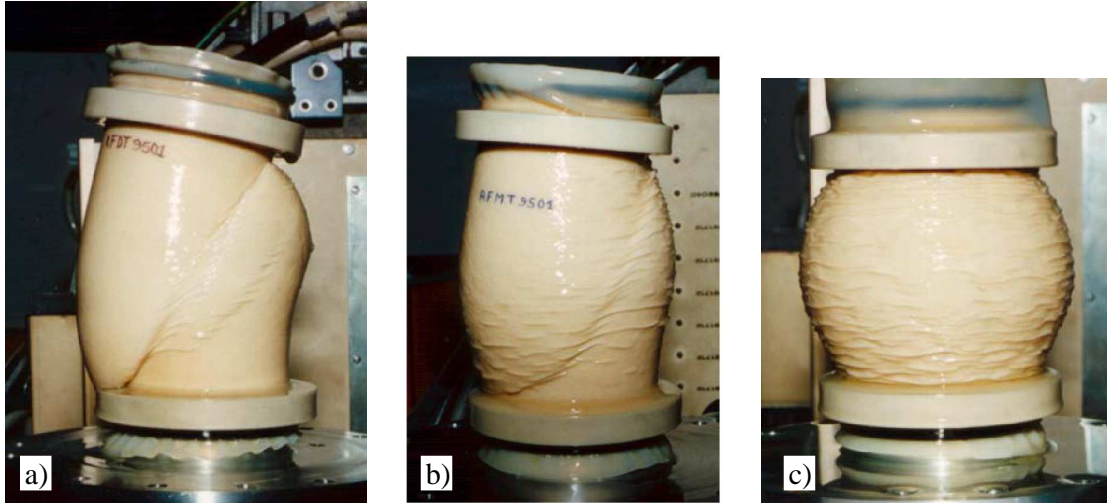


Figure 3.4: Results of triaxial shear tests on (a) dense, (b) medium, and (c) loose sand samples. (Jaques Desrues and co-workers [50], Laboratoire 3S, Grenoble, France.)

limit of how much shear stress a material can support, the stress on the platens is increased until the material in the cylinder fails (see Fig. 3.3) and forms sliding regions (shear bands) within itself. From the collected data, fundamental material parameters are extracted (e.g. the angle of internal friction, the apparent cohesion, and the angle of dilatancy). These material parameters are then used in computer models to help engineering decisions prior constructions, for example, by predicting soil stability on a slope.

In plane strain or biaxial tests, which use a quasi-two-dimensional arrangement, direct observation is usually sufficient to evaluate the geometrical and physical properties of shear bands (see Fig. 3.1). In triaxial tests, however, it is difficult to get information from inside the samples. The study of localization patterns building up in strained three-dimensional specimens gained more attention only after nondestructive experimental techniques such as accurate X-Ray Radiography, Magnetic Resonance Imaging (MRI), and Computer Tomography (CT) became available.

Based on X-Ray absorption, with a carefull calibration, a CT apparatus – probably the most accurate method of those mentioned above – can measure the packing density at any point inside a sample. Such measurements [50, 17] revealed complex shear band morphologies and provided quantitative information on the inhomogeneous distribution of the packing density inside sheared specimens.

Desrues and his co-workers (Laboratoire 3S, Grenoble, France), since the 1980's, have executed numerous experiments on different kinds of sand, clay, and clayey rocks [49]. They have used the European Synchrotron facility (ESRF, Grenoble), which provides high energy X-Ray beams for high resolution CT imaging. This made possible to detect shear bands developed in triaxial shear tests and to quantify their properties [50].

Under slow compression and specific geometric conditions, if tilting of the upper platen was allowed, the tested dense specimens formed a planar shear band spanning across the whole sample (see Fig. 3.4). If the specimen was less dense or the symmetry was enforced with non-tilting end platens, more complex shear band morphologies developed. These were usually dominated by two conical surfaces near the top and the bottom ends and complex radial structures around them.

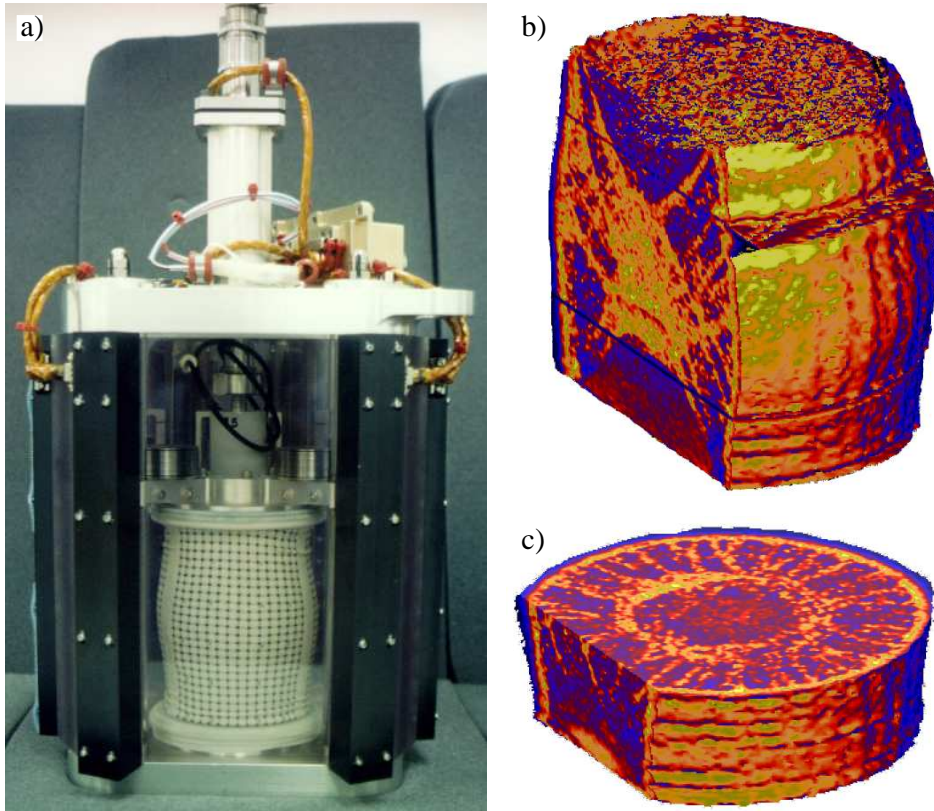


Figure 3.5: Triaxial shear tests executed in microgravity conditions aboard a NASA space shuttle: (a) Experimental setup, (b, c) CT scans. (Stein Sture and co-workers [8, 17], University of Colorado, Boulder, USA.)

Similar results were obtained by Sture and his co-workers (University of Colorado, Boulder, USA). In collaboration with the NASA, they have executed triaxial shear tests (see Fig. 3.5 (a)) [8, 17] at low effective stresses in microgravity aboard space shuttles (missions STS-79 in September 1996 and STS-89 in January 1998) and – for reference – in terrestrial laboratories. They have also used CT scans to quantify the distribution of packing density inside the sheared samples, and to track the onset, propagation, thickness, and inclination angle of the formed shear bands.

The tested specimens [8, 17] had large initial densities and during the triaxial tests the end platens could not tilt, i.e. the system had an enforced axial symmetry. This symmetry provoked multiple shear bands to form at nearly the same time after the peak stress and the maximum strength level was reached. The samples formed shear bands with thicknesses of mean and median between 8 and 16 grain diameters.

The shear cones (see Fig. 3.5 (b)) developed during the tests occupied approximately one-third of the sample's volume. Radial shear bands (see Fig. 3.5 (c)) were initiated in the distant post-peak stress regime. The tested specimens had many regions that could produce further shear bands. The geometrical constraints prevented sliding regions from fully developing. Diffuse dilation was found even when zones of high strain localization were already formed. In numerous places the shear bands were relatively short, crossing each other at large angles, and showing strong discontinuities. There were also many isolated areas being cut off by shear bands from the rest of the specimen.

These results are in good agreement with the results of Desrues et al. [50], even though the latter were obtained under normal gravity and large confining pressure. Similar shear band morphologies, obtained in computer simulations, at zero gravity and small confining pressure, are going to be discussed in Chapter 7.

In shear tests, the stabilization of the overall volume change is often considered an indication that a critical (or limiting) state has been reached, and conclusions regarding the process leading to this state are drawn from the evolution of the global volumetric strain. Recently several authors have questioned the physical relevance of such arguments (see for example [50]), and indeed, the experimental results using quantitative density measurements based on CT scans of both Desrues et al. [50, 17] and Sture et al. [8, 17] suggest that a critical state can be reached inside and only inside the shear bands, while global measurements can be misleading. We return to this question in Chapter 8.

Chapter 4

Distinct element simulations

Because of the highly discontinuous nature of granular materials, it seems straightforward to treat them in discrete models. Many computational methods – including the different variants of the *Distinct Element Method* (DEM) introduced by Cundall and Strack [44] – use this approach [145, 181]. Computer simulations do not only replicate experimental results but they are also capable of predicting the behavior of granular materials in several conditions [103]. Simulations facilitate the study of phenomena which are expensive or barely, if at all, accessible to experiments.

Computer simulations based on DEM incorporate concepts from various domains of discrete geometry, theoretical physics, and numerical computing. In these, so called, *distinct element simulations* the trajectory of each participating element is calculated from its interaction with the other elements (grains or boundary objects), the interstitial fluid or gas (if any), and external factors such as gravity or electric and magnetic fields. The relation between micromechanical properties and macroscopic effects can be studied in a natural way with such simulations. This makes them extremely useful for testing new theoretical concepts and ideas. The capability of realistically capturing the characteristics of granular materials makes distinct element simulations a common tool used to design, analyze, and optimize industrial processes.

In what follows, in Section 4.1, we give a brief overview of the general framework adapted by simulations based on DEM with an outlook to other computational methods used to simulate the behavior of granular materials. In Sections 4.2, 4.3, and 4.4, we discuss the details of three key steps of distinct element simulations: (1) Identifying the possibly interacting element pairs based on discrete geometry considerations, (2) calculating the interaction of colliding elements based on different contact models, and (3) computing the motion of each element based on numerical integration of Newton's equations. We focus mainly on the techniques used in our computational investigations which are going to be presented in Part II and III of this Thesis.

4.1 Overview and outlook

Distinct element simulations start from an initial configuration of a virtual physical system. The usual simulated systems have open boundaries, however, in several studies, in order to imitate infinitely large particle systems, periodic boundary conditions are considered. In most of the cases, the system consists of spherical particles and planar or cylindrical walls. However, more complex objects such as polygonal [159], polyhedral [164, 165], or

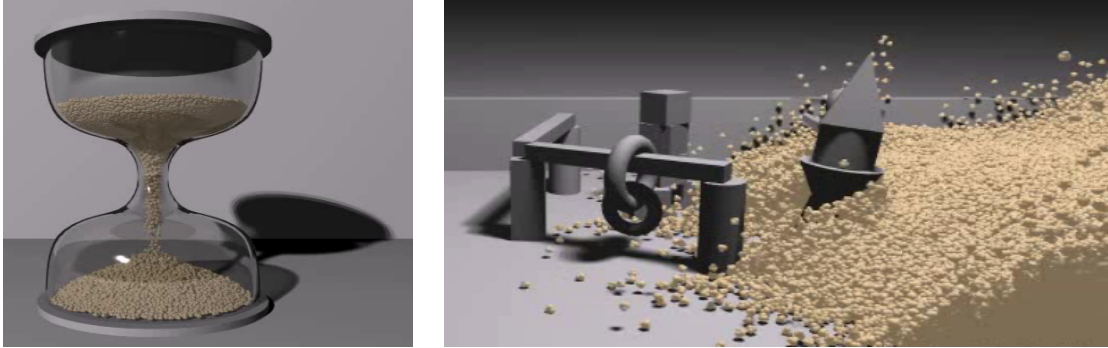


Figure 4.1: Distinct element simulations in computer graphics [18]. Granular systems are used in building virtual environments and animating natural phenomena.

ring-shaped [160, 18] elements can be also encountered. The easiest way to obtain complex objects is to glue together spherical particles. Objects with higher order geometrical shape, such as an ellipsoid, are avoided because checking whether they are in contact or not leads to a difficult and slow numerical problem.

In distinct element simulations, the interaction of the objects is usually computed explicitly. In simple systems only elastoplastic contact forces are present. In complex systems, cohesive, hydrodynamic, electric, and magnetic interactions can also play a role. Some objects can have controlled trajectories independent of the forces and torques acting on them. All the other objects, are moved to new locations by solving Newton's equations. The force calculation and integration procedure is repeated several times. This can be used either to create computer animations of artistic value (see Fig. 4.1) or to make investigations based on measurements on the simulated system. The data can be either processed during the simulation or it can be stored for later evaluation.

Regarding their approach, distinct element simulations are very close to simulations based on Molecular Dynamics (MD) [225, 187], which deals with particles at atomic level and time scales of nano and microseconds. However, in MD, external factors such as constant pressure and constant temperature are important and the particles usually follow the gradient of a complex potential depending on the relative position of many other particles. Unlike molecular systems, ordinary granular materials evolve on time scales of milliseconds (or larger) and they are usually free of thermodynamic effects, while the interactions are normally restricted to pairwise interactions. Many different contact models were introduced to describe the interaction of the grains.

Despite of the numerous differences, distinct element simulations of granular materials, in the older literature, are sometimes called MD simulations [191, 145], which is misleading. Even though it is clear that simulations based on DEM are influenced by the MD methodology and they are algorithmically very close to each other, we consider it important to distinguish the two. For the same reason, distinct element simulations of granular systems are also referred as Granular Dynamics [191, 181]. In this Thesis, we follow the naming introduced by Cundall and Strack [44]. In the literature, the same method is also denoted as *Discrete Element Method*.

Variants of distinct element simulations differ mainly in the way how the interactions are calculated. One can distinguish “hard” and “soft-body” simulations. In this Thesis we focus on “soft-body” methods [44, 145, 181], which are probably the most reliable and the

most popular. Soft-body models allow overlaps between the objects and calculate contact forces from the measure of these overlaps and the relative velocity of the bodies in contact (see Section 4.3). The main advantage of soft-body models over other approaches is that they can in a natural way incorporate long range interactions such as particle-particle hydrodynamic, electric, and magnetic interactions.

In usual soft-body distinct element simulations [44, 145, 181], the forces acting between the participating elements are calculated explicitly and Newton's equations are solved numerically. There are also some special soft-body methods, which avoid solving Newton's equations explicitly. Instead, an iterative relaxation scheme is used [266]. This eliminates the maximum unbalanced force by making the minimal adjustment to particle positions. This simplification can result in a faster computer program, however, it is known to introduce nonphysical effects in certain conditions [266].

The so called Contact Dynamics (CD) simulations [116] use a similar relaxation technique. In addition, CD simulations assume infinitely hard particles and not only the force balance but also the exclusion of body overlaps is prescribed. In these hard-body simulations, the force in a given contact depends on the forces acting in the other contacts, and thus the force calculation is more a global rather than a local task. Finding the appropriate forces and body positions, which do not violate the prescribed dynamical and geometrical constraints, is achieved iteratively through a directed random search [156, 116, 237, 235] resembling the non-linear Gauss-Seidel iterative scheme used to solve general non-linear systems of equations.

Another type of hard-body simulation technique, the so called Event Driven (ED) method [91, 181], makes further simplifications and does not calculate forces at all, but considers instantaneous collisions and computes post-collision velocities directly from the velocities present before the collisions. In this approach, the simulated granular system evolves from collision to collision through free falling states inbetween. The ED method proved to be useful in modeling the kinetic behavior of dissipative granular gases (see cluster formation) [91, 29]. However, in specific cases, ED simulations can lead to the undesired effect of infinitely many collisions, the so called *inelastic collapse* [153, 29], which manifests itself in infinitely long execution time on a computer.

Lattice gas methods go even further and allow the particles to move only on a lattice [124, 67, 115]. In addition, the particles are allowed to take only discrete velocities and strict collision rules decide the time evolution of the system similar to a stochastic cellular automata. Dissipative collision rules are introduced in order to model the inelasticity of particle contacts. In lattice gas simulations, a triangular lattice proved to perform better than a square lattice because of the higher degree of symmetry of the former, which assures higher order statistical variance in the system's state space. A lattice-gas model of granular avalanches could reproduce specific bounded outflow statistics and finite-size effects [124] as well as non-Newtonian flow properties [67, 115].

Other discrete simulation techniques used to model specific aspects of the behavior of granular systems do also exist. For example, Török et al. [227, 228, 229] developed a statistical model of sheared granular media and explained characteristics of shear bands such as self-organization, localization, and aging. One further model, the Tetris model, discussed by Piccioni et al. [178], was used to associate the directed percolation problem with the dilatancy angle of a granular system.

We must also mention the Finite Element (FE) simulations, which – apart from the above models – are based on continuum models [259, 205]. FE simulations, used mainly

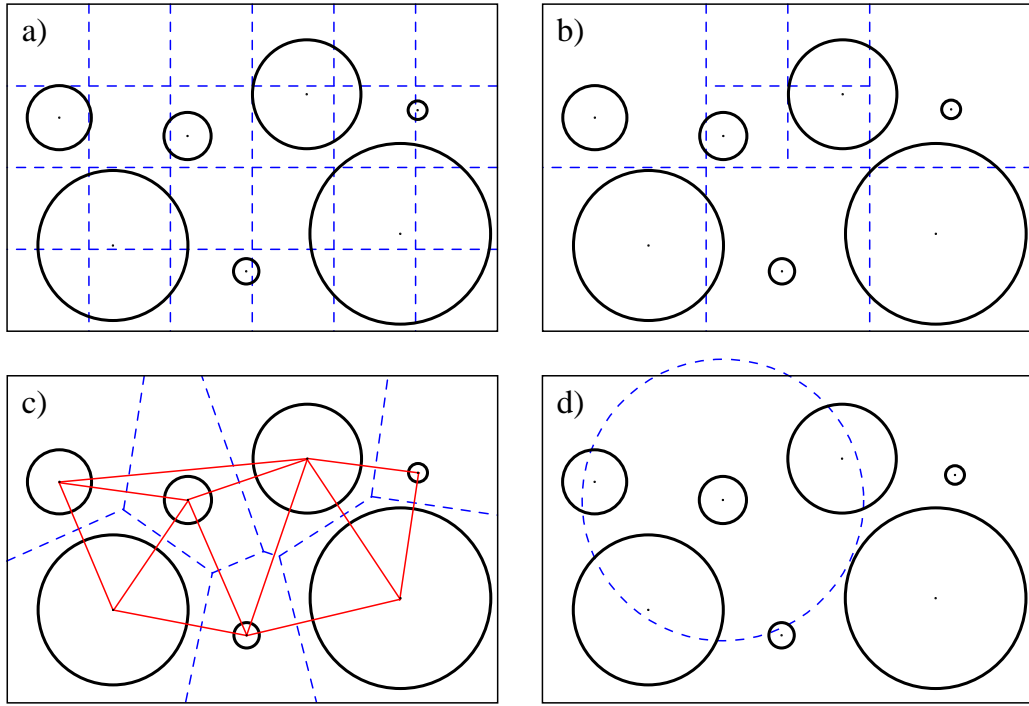


Figure 4.2: Geometric constructs used to speed up the detection of interacting element pairs: (a) lookup grid, (b) hierarchical subdivision, (c) regular triangulation, (d) list of closest neighbors.

in engineering applications, can reproduce many effects of sheared granular media such as strain localization, strain softening, and failure [130, 224]. For further information and a comparison with distinct element simulations see [126].

4.2 Discrete geometry

Handling the high level of discreteness of granular systems, which is further emphasized by practically always “hard” contact interactions¹, makes distinct element simulations algorithmically complex. Finding the element pairs which are “close” to each other is computationally the most challenging part. Solving this purely geometrical problem, which is mostly independent of the way the interactions are calculated, should not affect the outcome of the simulations. It is only meant to increase their efficiency. Indeed, the overall performance of a distinct element simulation program dependence very much on building – as fast as possible – a sufficiently tight set of *possibly* interacting element pairs and applying the interaction model only on these pairs.

In practice, it makes no sense to find the *tightest* set of such element pairs because the condition whether they are interacting or not is inevitably tested once more when the interactions are calculated. In fact, one could also consider all the possible pairs and let the interaction model select those which are really interacting and neglect the others. This naive $\mathcal{O}(N^2)$ method (where N is the number of participating elements) is very

¹Usual granular systems, such as sand, consist of hard grains. Even in soft-body simulations the stiffness of the particles is usually set to a high value.

inefficient even for relatively small systems. Below we present some algorithms, which can improve the speed of interaction calculation to $\mathcal{O}(N)$. For a two-dimensional system of disks which interact only when they come into contact, the geometric constructs used by these algorithms are outlined in Fig. 4.2.

Probably the simplest way to find particles, which are close to each other, is to divide the space into cells of a given size and “assign” each particle to the cell in which its center point is located (see Fig. 4.2 (a)). Then, finding the possibly interacting particles is done by checking the neighboring cells. Because of its simplicity, this method is widely used in distinct element simulations. If the particles and the cells have more or less the same size and thus in average each cell contains one single particle, this lookup grid gives a solution close to optimum. However, if there are both very small and very large particles in the simulated system, then this becomes less efficient.

In case of a fine grid, having a cell size close to the size of the smallest particle, not only the adjacent cells but also second or higher order neighbors are to be considered. In a region where the particles are predominantly small, this is needless and a waste of time. If we have a coarse grid, having a cell size close to the size of the largest particle, then a grid cell can contain many small particles. In a region where the size of the particles is again predominantly small, the large majority of the particles in one cell is not in contact with any particle in the adjacent cells. Consequently, applying the contact model between these particles is again no more than a waste of CPU time.

The above problems are solved by using an adaptive cell size [160, 104]. Starting from a sufficiently large box, containing all the particles, the space is divided into smaller boxes. Each box, which contains more than one particle, is further divided into even smaller boxes. The procedure is repeated until each box contains no more than one particle. This leads to a hierarchical structure. At least on the highest level, this should accommodate the shape of the simulated system (see Fig. 4.2 (b)).² Neighboring particles are found by considering nodes which are hierarchically close to each other. This method is more efficient than a lookup grid only when the particles have a wide (e.g. power law or exponential) size distribution. Otherwise, updating the hierarchical structure as the particles move is more time consuming than updating the lookup grid and – even more – finding the neighbors of a particle is algorithmically more complex.

Finding the regular triangulation (also known as the weighted Delaunay triangulation) [135, 59] of a particle system leads to an optimum adaptive cell size (see Fig. 4.2 (c)). This is neither algorithmically nor computationally easy and dynamically updating the structure requires specific care [159, 79].³ An important property of the regular triangulation is that the corresponding regular Voronoi cells assure that the particles are completely inside their own cell, except if they overlap, in which case the cell boundary passes through the intersection points.⁴ According to this property the connected elements of the triangulation are good candidates for interacting particle pairs. For a dense system, the set of pairs identified in this way is tighter than the set of possibly interacting particle pairs obtained with any other method presented before. However, because of its complexity, this

²If the space is divided in exactly four parts on each level, then the resulting hierarchical structure is a so called quadtree. This is typical for two-dimensional simulations.

³Updating the triangulation is done by moving the particles one-by-one and assuring the consistency through local modifications (so called flips). It is assumed that the particles do not move too fast.

⁴Notice that this is not necessarily true for the (normal) Voronoi cells of the center points. However, if the particles have identical size, the normal and the weighted Delaunay triangulations are identical.

method is rarely used.

Based on the fact that in certain conditions the local geometrical structures change slowly, one can assign each particle a list of other particles which are closer than a given distance and use these lists for interaction calculation (see Fig. 4.2 (d)).⁵ If the lists of closest neighbors are in average short and they are updated only in large time intervals, then the efficiency of this method is comparable to the efficiency of the other methods presented above. However, finding the adequate “cutoff” distance and the number of simulation steps after which the lists must be updated is not an easy task.

The temporal latency of topological changes can be exploited with any of the methods presented before. Updating the used constructs (grid, subdivision, or triangulation) can be neglected for some simulation steps, providing that between two updates the corresponding set of particle pairs contains all the pairs of interacting elements, even if the encoded geometrical information can become meanwhile corrupted. To speed up the access to the particle pairs, their list can be stored explicitly (i.e. cached). This gives a more elegant but practically equivalent method to the last method presented above. Storing the list of possibly interacting particle pairs and delaying its update for some number of simulation steps is a powerfull but very dangerous technique. One is faced with the difficult trade off between the update time, which should be as large as possible, and the number of closest neighbors, which should be as small as possible.

Usually it is difficult to predict the dynamical time scale of a granular system and in many cases there are more characteristic time scales. For example, a slowly evolving system might suddenly produce rapidly moving parts such as an avalanche. If the refresh rate was not chosen correctly, some particle pairs, which are in fact interacting, are not detected and thus some forces are not calculated. This can lead to nonphysical artifacts. A possible outcome is that the particles pass through each other without noticing this fact or they get too close to each other, produce huge overlaps resulting in huge forces, and the system virtually explodes.

Extending the algorithms outlined in Fig. 4.2 to three-dimensions (i.e. to spheres) is usually straightforward. Incorporating long range interactions (such as magnetic or electric forces) is also easy, provided that they are restricted to a cutoff value. If no cutoff value is imposed, long range interaction can be handled on an all-to-all basis or by using a hierarchical structure and multipole approximations [15]. Working with non-spherical grains is in general more difficult. Elements having a shape of certain spherical symmetry can be processed by considering their circumscribing spheres first, then refining the results based on their specific shape. Elements having extreme shapes such as a planar or cylindrical wall usually must be handled separately, making use of their specific geometrical properties.⁶

4.3 Contact models

The physical essence of soft-body distinct element simulations is given by models defining the contact interaction of the participating objects. These are obtained from the measure of geometrical overlaps and the relative velocity of the bodies in contact. The

⁵The method was introduced by Verlet for Molecular Dynamics simulations [225, 187].

⁶For example, in case of a grid based method, one can assign the list of neighboring cells to the wall and check its contact with the particle by visiting these cells.

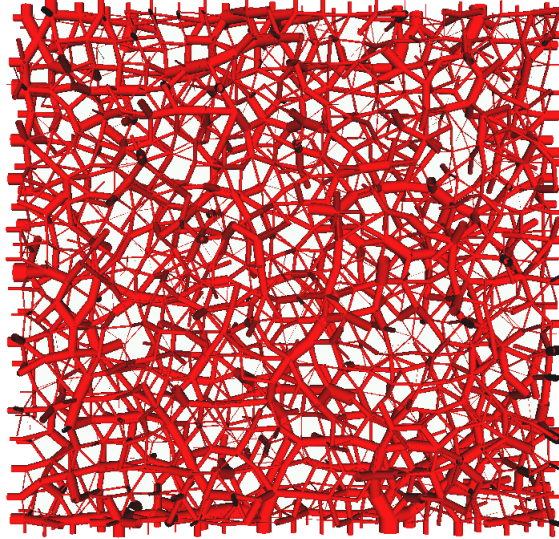


Figure 4.3: Network of force chains obtained in a distinct element simulation. The slice was taken from the middle of a homogeneously stressed large three-dimensional sample composed of equally sized spheres. (See also Fig. 6.3.)

contact models and their parameters are the main factors which determine the outcome of a simulation. In engineering applications, parameters such as the stiffness of the bodies, the restitution coefficient of the collisions⁷, and the internal friction are carefully calibrated in order to reproduce the behavior of a given specimen as closely as possible.

Regarding theoretical aspects, it is widely accepted that properties such as the packing density, the coordination number, and the characteristics of force chains (see Fig. 4.3) are the most important factors for the general behavior of a granular system. Even though a contact model, its parameters, or the size of a simulated sample cannot reproduce exactly an experimental situation, the outcome of the simulations should be comparable with experiments (at least) in the above properties.

Probably the most widespread contact model used in distinct element simulations is the so called *linear spring-dashpot model*. This model was introduced by Cundall and Strack [44] almost 30 years ago. It is based on the idea that when an overlap is established between two bodies, relative to the surface orientation of the objects, a normal and a tangential spring is created at the initial contact point. The motion of the bodies is governed by the elongation of these imaginary springs. The springs act until the bodies depart from each other and come out of contact.

In the linear spring-dashpot model [181], the normal and tangential components of the force, which the objects in contact exert on each other, is

$$F_n = -\kappa_n u_n - \gamma_n v_n, \quad (4.1)$$

$$\mathbf{F}_t = -\kappa_t \mathbf{u}_t - \gamma_t \mathbf{v}_t, \quad (4.2)$$

where $\kappa_{n,t}$ and $\gamma_{n,t}$ are normal and tangential stiffness and damping coefficients, u_n and \mathbf{u}_t are normal and tangential displacements relative to the initial contact point (elongation

⁷The restitution coefficient is defined by the ratio of the final and the initial relative velocity of two objects undergoing a collision.

of the springs), and v_n and \mathbf{v}_t are the relative velocities at contact point of arbitrarily translating and rotating objects.

The normal displacement, measured along the direction perpendicular to the surface of the bodies in contact, depends on the relative position, size, and shape of the objects. For example, in the case of two spheres this is calculated as

$$u_n = R_1 + R_2 - \|\mathbf{r}_1 - \mathbf{r}_2\|, \quad (4.3)$$

where $R_{1,2}$ are the radii of the spheres and $\mathbf{r}_{1,2}$ are the center points of the spheres. This is non-negative as long as the spheres overlap. When u_n becomes negative, the bodies do not touch each other any more and no contact force should act between them.

The tangential displacement \mathbf{u}_t can be calculated by integrating the tangential velocity \mathbf{v}_t in the contact plane during the lifetime of the contact, i.e.

$$\mathbf{u}_t(t) = \int \mathbf{v}_t(t) dt. \quad (4.4)$$

In a two-dimensional case both the tangential displacement and the tangential velocity can be represented as scalars and thus the above vector integral reduces to a simple scalar integral. In three-dimensions, the situation is a bit more complicated because care must be taken in order to keep \mathbf{u}_t in the contact plane (see Appendix A).

The physical relevance of computing a tangential force lies in the fact that it can model static and sliding friction between the bodies. Care must be taken in order to avoid “ghost forces”, instabilities, and spurious dissipation [27]. According to the Coulomb rule, as any friction force, \mathbf{F}_t must obey the constraint

$$\|\mathbf{F}_t\| \leq \mu \|\mathbf{F}_n\|, \quad (4.5)$$

where μ is the coefficient of friction. In order to satisfy this rule, \mathbf{F}_t is shortened when its magnitude becomes too large, while its direction is kept.⁸ For modeling sliding contacts, the elongation of the tangential spring is also relaxed to $\mu \|\mathbf{F}_n\| / \kappa_t$, accordingly. Many distinct element simulations make no difference between the coefficients of static and sliding friction, even though such an extention is easy to implement.

A more simple and computationally more efficient model of friction can be obtained by assuming viscous dumping at small relative velocities and using the largest friction force allowed by the Coulomb rule otherwise (see Fig. 4.4). In this model, the frictional force is calculated as

$$\mathbf{F}_f = -\min(\mu \|\mathbf{F}_n\|, \lambda \|\mathbf{v}_t\|) \mathbf{v}_t / \|\mathbf{v}_t\|, \quad (4.6)$$

where λ is the coefficient of viscous friction active for small tangential velocities. Notice that there is a continuous but non-smooth transition between the two working regimes at small and large relative velocities.

This approach eliminates the computationally expensive book-keeping required for simulating the tangential springs and it can speed up the computation significantly. However, in turn, the model handles only sliding friction. Furthermore, finding an appropriate λ parameter or alternatively choosing a suitable relative tangential velocity, which decides

⁸One could also change the direction of \mathbf{F}_t to be opposite to the tangential velocity. However, this can introduce discontinuities, while on a larger time scale the same result is achieved smoothly if the tangential velocity does not change too fast.

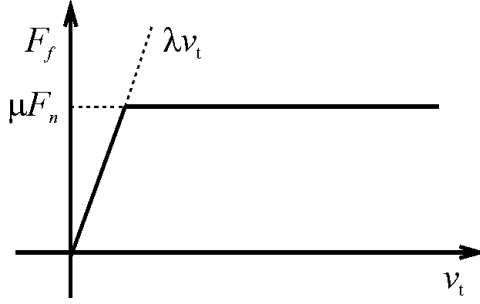


Figure 4.4: Simple model of sliding friction. The frictional force \mathbf{F}_f is oriented oppositely to the relative tangential velocity \mathbf{v}_t . Viscous friction is assumed at small v_t .

between the viscous and sliding regimes, is not a straightforward task. One possibility is to consider the velocity a particle can reach in free falling state during the time an average collision lasts and assume viscous friction below this limit and sliding above it. Based on our experience, this choice avoids non-physical artifacts and has a beneficial effect on the numerical stability of the simulation.

A more sophisticated approach to calculate contact forces between two objects is given by the Hertz model [133] combined with an appropriate damping term. The most widely accepted form of this model [129, 30, 181] defines the normal contact force as

$$F_n = -\kappa_n u_n^{3/2} - \gamma_n u_n^{1/2} v_n, \quad (4.7)$$

where u_n and v_n denote normal displacement and relative velocity, while κ_n and γ_n are again stiffness and damping coefficients. This model is basically a *non-linear* spring-dashpot model. Notice, however, that κ_n and γ_n are not interchangeable with the similar parameters of the *linear* spring-dashpot model.

Similar to the linear model of Cundall and Strack [44], the non-linear Hertz model should be combined with a suitable friction model. One can either consider an imaginary tangential spring – linear or non-linear – or the simple sliding friction model presented before. Care must be taken, however, in choosing the friction model and setting its parameters, in order to avoid anomalies originating from the different time scales characteristic to the normal and tangential forces [181].⁹ Further extenstions can also incorporate rolling friction [263, 117] and coupling between sliding and spinning motion [66, 16] or viscous friction with the interstitial medium [181].

One advantage of the linear spring-dashpot model over the non-linear Hertz model (and its extenstions) is that the exact relation between the model parameters (i.e. the stiffness and damping coefficients) and the collision time as well as the restitution coefficient of an individual collision can be found analytically, while the Hertz model can be solved only numerically. Even though rough estimates exist [133, 181], the difficulty of predicting the characteristic collision times and restitution coefficients makes the design and implementation of distinct element simulations based on the Hertz model more challenging than the original method of Cundall and Strack [44].

Still, in many cases, it's worth the effort, because the Hertz model is much more realistic and much more deliberate in giving a theoretical foundation of its parameters,

⁹If the particles are too soft, the model may result in unphysical behavior where the braking force of collisions becomes too small (brake failure effect) [202].

which are reduced to the shape of the surfaces in contact and to material parameters such as Young's modulus and Poisson's ratio [133, 181]. Regarding engineering applications, the importance of this lies in the fact that such material parameters are well known (or they can be measured), and thus setting the model parameters to values close to those which reproduce the properties of a specific sample becomes possible.

There are further contact models based on more elaborate elastoplastic considerations [250, 182]. In general, these are characterized by dissimilar loading and unloading behavior. Many excellent monographs [191, 192, 79, 145] and text books [56, 181] present them and show their applicability. Here, we do not go in details regarding these models because discussing them goes beyond the scope of this Thesis.

4.4 Motion integration

The general position of an arbitrary object can be given with a combination of translation and rotation. The motion is usually described with the translation of the body's center of mass and a rotation around an axis passing through this point.¹⁰ Here, we consider soft-body distinct element simulations and we first restrict ourselves to computing the translational motion of the elements. Later, we turn to rotation integration.

Solving Newton's equation through a numerical scheme moves the particles to new position from simulation step to simulation step. Considering the total force \mathbf{F} acting on a body of mass m , the acceleration is

$$\mathbf{a} = \mathbf{F}/m. \quad (4.8)$$

With the simplest possible method, known as Euler's method, the new position and velocity of the object is obtained as

$$\mathbf{r}(t + \delta t) = \mathbf{r}(t) + \mathbf{v}(t) \delta t, \quad (4.9)$$

$$\mathbf{v}(t + \delta t) = \mathbf{v}(t) + \mathbf{a}(t) \delta t, \quad (4.10)$$

where δt is a small time step. The new positions and velocities can be used to update the forces, repeating the procedure as many times as needed. The integration time step δt can be either fixed or adapted to the dynamical time scale of the simulated system.

The above method tends to "produce" kinetic energy as a result of integration errors. Even though this is usually not critical for granular systems, which are strongly dissipative and thus the energy gained through numerical errors is balanced by the energy dissipated in collisions, for physical correctness, in some cases, a more accurate integration scheme might be required. However, the more accurate an integration scheme is, the more computation it needs. Some higher order methods [225, 187], such as the Predictor-Corrector method or the Runge-Kutta method, provide higher accuracy but in turn they are much slower than Euler's method. In this respect, Verlet's Leap-Frog method is a good compromise: It is both sufficiently accurate and computationally efficient.

The Leap-Frog method, originally developed for MD simulations [225, 187], calculates the velocity in an intermediate state

$$\mathbf{v}(t + \delta t/2) = \mathbf{v}(t - \delta t/2) + \mathbf{a}(t) \delta t, \quad (4.11)$$

¹⁰In fact, any point could be used. Using the center of mass, simplifies the physical equations.

where $\mathbf{v}(t - \delta t/2)$, in the first simulation step, is obtained as

$$\mathbf{v}(t - \delta t/2) = \mathbf{v}(t) - \mathbf{a}(t) \delta t/2. \quad (4.12)$$

The new position and velocity of the bodies is then calculated as

$$\mathbf{r}(t + \delta t) = \mathbf{r}(t) + \mathbf{v}(t + \delta t/2) \delta t, \quad (4.13)$$

$$\mathbf{v}(t + \delta t) = 2\mathbf{v}(t + \delta t/2) - \mathbf{v}(t). \quad (4.14)$$

Because of its simplicity, Verlet's Leap-Frog method is the most popular and the most widely used integration scheme in distinct element simulations.

The rotation of objects can be calculated in a similar way as their translation. In general, both the orientation and the angular velocity of the objects is computed step-by-step. However, in several cases, one can make use of the fact that the orientation of spherical objects is insignificant. If visualization of the rotation is not needed, it is usually enough to compute the angular velocity by integrating the equation

$$\dot{\boldsymbol{\omega}} = \mathbf{I}^{-1} (\mathbf{T} - \boldsymbol{\omega} \times (\mathbf{I} \boldsymbol{\omega})), \quad (4.15)$$

where $\boldsymbol{\omega}$ is the angular velocity, \mathbf{T} is the torque acting on the body, and \mathbf{I} is the moment of inertia tensor in the observational coordinate system.¹¹ The integration schemes mentioned above (Euler, Leap-Frog, etc.) can be adapted to solve this equation.

In two-dimensions, the orientation of arbitrarily shaped bodies can be described by a rotation angle relative to a fixed direction and the methods used for computing the translational motion can be easily applied to compute the rotational motion too. However, in three-dimensions, finding an efficient representation of orientation and updating it as the bodies roll and tumble through space is a bit more difficult.

The straightforward way to represent the orientation of a three-dimensional object is to use a matrix describing a rotation which brings the object into its current state from a fixed reference state. This representation is very redundant: It stores nine values instead of the strictly necessary three. Using the angles of three rotations executed around fixed axes, such as the Euler angles, would be a significant improvement, however, these are numerically unstable and practically useless in distinct element simulations. The best choice seems to be the use of a quaternion representation. This provides both compact and numerically stable description of orientation. Integrating the rotation of bodies in quaternion representation can be done by using either Euler's method or the Leap-Frog method. The details of these are presented in Appendix B.

¹¹The moment of inertia tensor \mathbf{I} is fully defined by its eigenvalues. In the body fixed eigensystem, \mathbf{I} is diagonal. This must be transformed according to body orientation, in order to find \mathbf{I} in the observational coordinate system.

Part II

Magnetized grains

Chapter 5

Introducing an interaction cutoff

Long range interaction presents a major challenge for computer simulations of different particulate systems. At each discrete simulation time step the order of N^2 calculations (where N is the number of particles) are to be carried out, which limits the size of the tractable systems, though for many purposes large systems (meaning large N values) need to be studied for many simulations steps. If allowed by the geometry and possible due to screening, periodic boundary conditions, which are often helpful, can be implemented only by using sophisticated summation algorithms. In principle these problems occur in so called “short range” interaction models as well, like in the most extensively studied Lennard-Jones system. For this system, a cutoff is usually introduced, making the original short range model explicitly finite range. It is generally accepted that the error introduced by the cutoff is negligible provided that the cutoff distance is large enough [225].

In many physical systems, e.g. in electrostatic systems, the long range interaction potential falls off as $1/r$, where r is the distance between the particles. In the Lennard-Jones system, where it is assumed that the attractive part of that potential is due to induced dipole-dipole interactions, the potential decreases as $1/r^6$. In this Chapter, we focus on the question of cutting off a potential which is in between the above two cases. We consider a two-dimensional ensemble of dipolar magnetic particles interacting with an $1/r^3$ potential, which – due to the characteristic dipole-dipole interactions – has also an orientation dependence. It is crucial from the point of view of efficient computer simulations to know if a reasonable cutoff can be introduced in such a system. We investigate the question by comparing the stability of static configurations.

As we will see later, in two-dimensional arrangements of dense dipolar particle systems there are two main local dipole arrangements: (1) a ferromagnetic state with dipoles organized in a triangular lattice, and (2) an anti-ferromagnetic state with dipoles organized in a square lattice. Such local orderings can be simply reproduced in distinct element simulations. In such simulations, to check the characteristics of deposited magnetic granular systems, under normal gravitational conditions ($g = 9.8 \text{ m/s}^2$), we have thrown spherical magnetic particles of diameter 1 mm, density 7.5 g/cm^3 , and magnetization 153 emu/cm^3 in a quasi-two-dimensional Hele-Shaw cell filled with a fluid of viscosity 0.1 kg/ms . For simplicity, only the Stoke’s friction was taken into consideration. Particle-particle friction and complex hydrodynamic interactions were neglected.

In accordance with well known results [255, 20, 21, 246, 253, 211], we found that the particles form chains which collapse and fold into structures shown on Fig. 5.1 (a). Experiments devoted to the direct measurement of magnetic interparticle forces [218] suggested

that configurations of two particles can be considered a basic building block of more complex arrangements. However, cutting off the magnetic interaction to 2 particle diameters (Fig. 5.1 (b)), we found that the character of local orderings changes significantly. At the same time, for a cutoff distance as large as 4 particle diameters (Fig. 5.1 (c)) the local orderings are already very similar to the long range case (Fig. 5.1 (a)).



Figure 5.1: Dipolar magnetic particles interacting with (a) infinite range forces and with forces cut off at (b) 2 and (c) 4 particle diameters.

Examining the magnetic orientations (see Fig. 5.2), we found that in case of infinite range forces (Fig. 5.2 (a)) and in case of an interaction cutoff of 4 particle diameters (Fig. 5.2 (c)) the neighboring particle chains have more likely the same magnetic orientation, while in the case of an interaction cutoff of 2 particle diameters (Fig. 5.2 (b)) the orientation changes from line to line. In other words, for infinite range forces and for sufficiently large interaction cutoff, the particles in general form ferromagnetic arrangements in compact triangular structures, while for too small interaction cutoff values the particles organize themselves into anti-ferromagnetic domains with sparse square-lattice structures.

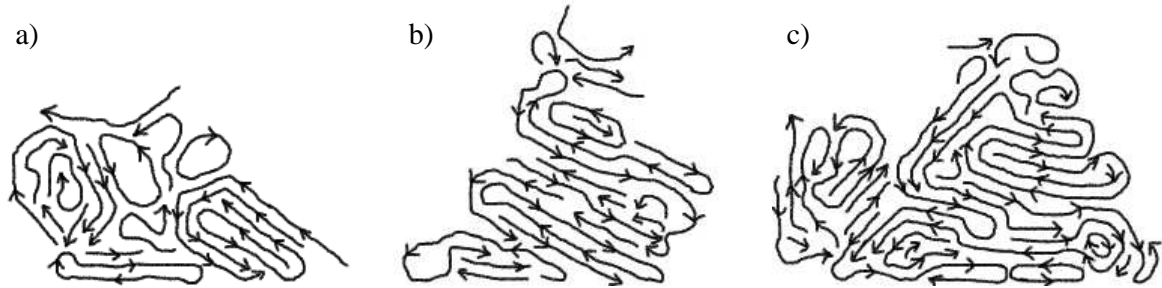


Figure 5.2: Magnetic orientation of dipolar particle chains for (a) infinite range forces and at interaction cutoff values of (b) 2 and (c) 4 particle diameters.

In the next Sections, we first present a theoretical framework for calculating the magnetic ground state of two-dimensional particle arrays, then we discuss in detail the effect of the interaction cutoff on a two-line system. Our numerical calculations led to the observation that the ferromagnetic state is much more sensitive to the interaction cutoff than the corresponding anti-ferromagnetic state. For infinite range interactions the ferromagnetic state dominates energetically over the anti-ferromagnetic state. The situation is reversed rapidly at low interaction cutoff values leading to the disappearance of the ferromagnetic ground state. Studying the effect of bending ferromagnetic and anti-ferromagnetic two-line

systems we show that the cutoff has a major impact on the energetically favorable magnetic state. Based on these, being interested in local orderings of two-dimensional dipolar granular systems, we derive a lowest reasonable choice for dipole-dipole interaction cutoff. At the end of this Chapter we discuss the limitations of our approach and the possible higher order corrections.

5.1 The Luttinger-Tisza method

The Hamiltonian of a dipolar system is

$$H = \frac{1}{2} \sum_{i \neq j} \mathbf{s}_i^T \mathbf{J}_{ij} \mathbf{s}_j, \quad (5.1)$$

where i and j are dipole indices, \mathbf{s} denotes the dipole momentum vector, \mathbf{s}^T is the transpose of \mathbf{s} , and

$$\mathbf{J}_{ij} = \frac{1}{\|\mathbf{r}_{ij}\|^3} \left[\mathbf{I} - 3 \frac{\mathbf{r}_{ij} \mathbf{r}_{ij}^T}{\|\mathbf{r}_{ij}\|^2} \right], \quad (5.2)$$

where \mathbf{I} is the identity matrix, \mathbf{r}_{ij} is the relative position of two dipoles, and $\|\cdot\|$ denotes vector length. The $1/2$ factor in Eq. (5.1) avoids double counting of dipole pairs.

The Luttinger-Tisza method [148], widely used to study the crystalline state of a dipolar system, is based on the assumption that the ground state of such systems exhibits some discrete translational symmetry. Let $\Gamma(i)$ denote the set of points generated from a point i with discrete translations belonging to a symmetry group Γ . The mentioned ground state symmetry is equivalent to the condition $\forall i' \in \Gamma(i) : \mathbf{s}_i = \mathbf{s}_{i'}$. Based on this, the system can be broken into identical cells and the summation in Eq. (5.1) can be transformed into a summation over one single cell. Consequently, the energy per dipole can be calculated as

$$E = \frac{1}{2n} \sum_{i,j=1}^n \mathbf{s}_i^T \mathbf{A}_{ij} \mathbf{s}_j, \quad (5.3)$$

where n is the number of dipoles per cell and \mathbf{A}_{ij} are symmetric matrices defined as

$$\mathbf{A}_{ij} = \sum_{\substack{j' \in \Gamma(j) \\ j' \neq i}} \mathbf{J}_{ij'}. \quad (5.4)$$

The expression of the energy per dipole in Eq. (5.3) can be given in a more compact form by considering the $\hat{\mathbf{s}} = (\mathbf{s}_i)_{i=1}^n$ hyper-vector and the $\hat{\mathbf{A}} = (\mathbf{A}_{ij})_{i,j=1}^n$ hyper-matrix. Using these, E can be written as

$$E = \frac{1}{2n} \hat{\mathbf{s}}^T \hat{\mathbf{A}} \hat{\mathbf{s}}. \quad (5.5)$$

Solving the eigenvalue problem of the nd dimensional symmetric matrix $\hat{\mathbf{A}}$, where d is the dimension of the dipoles, we find the ε_k eigenvalues and the $\hat{\mathbf{e}}_k$ orthogonal eigenvector system normalized to $\|\hat{\mathbf{e}}_k\| = \sqrt{n}$. Considering a dipole state $\hat{\mathbf{s}} = \sum_k b_k \hat{\mathbf{e}}_k$ given in the eigenvector system $\hat{\mathbf{e}}_k$, the energy per dipole can be calculated as

$$E = \frac{1}{2} \sum_{k=1}^{nd} \varepsilon_k b_k^2. \quad (5.6)$$

$\alpha = 60^\circ$	$E = -2.758$	Continuously degenerate ferromagnetic state
	$E = -2.047$	Six-fold degenerate anti-ferromagnetic state
$\alpha = 90^\circ$	$E = -2.549$	Continuously degenerate microvortex state including a four-fold Degenerate anti-ferromagnetic state
	$E = -2.258$	Continuously degenerate ferromagnetic state

Table 5.1: Ground state dipole arrangements and states with second lowest energy per dipole on an infinite rhombic lattice with rhombicity angle α . The energy is measured in S^2/a^3 units.

If the dipoles have identical scalar strength S , i.e. $\|\mathbf{s}_i\| = S$, then b_k must satisfy for all $i = 1 \dots n$ the condition

$$\left\| \sum_{k=1}^{nd} b_k \mathbf{e}_{k,i} \right\| = S, \quad (5.7)$$

where the vector $\mathbf{e}_{k,i}$ is the component belonging to dipole i in the hyper-vector $\hat{\mathbf{e}}_k$. Summing up the square of the above equations and taking into consideration that $\{\hat{\mathbf{e}}_k\}_{k=1}^{nd}$ forms an orthogonal system, we conclude that b_k must also satisfy the condition

$$\sum_{k=1}^{nd} b_k^2 = S^2. \quad (5.8)$$

In the framework of the Luttinger-Tisza method these two conditions are known as the strong (Eq. (5.7)) and the weak (Eq. (5.8)) condition. From the weak condition and Eq. (5.6) it can be derived that the energy per dipole in the ground state is $E_{min} = 1/2 \varepsilon_{min} S^2$, where ε_{min} is the value of the smallest eigenvalue of $\hat{\mathbf{A}}$. If there is one single eigenvalue equal to ε_{min} the ground state dipole arrangement is given by the corresponding eigenvector. If there are more eigenvalues equal to ε_{min} , then the ground state dipole arrangements are given by the linear combinations of the corresponding eigenvectors. However, only those linear combinations are physically relevant which satisfy the strong condition (Eq. (5.7)).

5.2 Two-dimensional array of magnetic particles

The above method was applied by Brankov and Danchev [26] to a system of two-dimensional dipole moments with identical scalar strength located at the sites of an infinite rhombic lattice with an arbitrary rhombicity angle. They considered that the ground state of this system has a translational symmetry corresponding to discrete translations along the lattice lines with multiples of $2a$, where a is the lattice constant. They have found that the ground state depends on the rhombicity angle.

We repeated their calculations (see Appendix C) with the consideration that the dipoles are carried by identical hard spherical particles of diameter equal to the lattice constant. According to this geometrical constraint, we limited the rhombicity angle to $60^\circ \leq \alpha \leq 90^\circ$. In accordance with the earlier results, we found that the system has a ferromagnetic ground state for $60^\circ \leq \alpha \lesssim 79.38^\circ$ and an anti-ferromagnetic ground state for $79.38^\circ \lesssim \alpha \leq 90^\circ$. The ground state for $\alpha = 60^\circ$ is a continuously degenerate ferromagnetic

$\alpha = 60^\circ$	$E = -2.582$	Two-fold degenerate ferromagnetic state
	$E = -2.226$	Two-fold degenerate anti-ferromagnetic state
$\alpha = 90^\circ$	$E = -2.477$	Two-fold degenerate anti-ferromagnetic state
	$E = -2.331$	Two-fold degenerate ferromagnetic state

Table 5.2: Ground state dipole arrangements and states with second lowest energy per dipole on two neighboring lines of an infinite rhombic lattice with rhombicity angle α . The energy is measured in S^2/a^3 units.

state and for $\alpha = 90^\circ$ is a continuously degenerate microvortex state including a four-fold degenerate anti-ferromagnetic state, where the microvortex state is defined as two anti-ferromagnetic sublattices making an arbitrary angle with each other. We have also identified the states with the second lowest energy per dipole. The results for $\alpha = 60^\circ$ and $\alpha = 90^\circ$ are summarized in Tab. 5.1.

In addition, we executed calculations taking into consideration the interaction of only two neighboring lines on the rhombic lattice. This corresponds to the interaction of two lines of dipolar hard spheres shifted according to the α rhombicity angle. The Luttinger-Tisza method can be applied in a straightforward way also in this case. The ground state depends on the rhombicity angle α similarly to the previous case. The system has a ferromagnetic ground state for $60^\circ \leq \alpha \lesssim 75.67^\circ$ and an anti-ferromagnetic ground state for $75.67^\circ \lesssim \alpha \leq 90^\circ$. The ground state for $\alpha = 60^\circ$ is a two-fold degenerate ferromagnetic state and for $\alpha = 90^\circ$ is a two-fold degenerate anti-ferromagnetic state. We summarized the results in Tab. 5.2.

It is not surprising that taking into consideration only two lines of the rhombic lattice reduces significantly the symmetry of the solution. In particular, the two-line system has no continuously degenerate ground state, and thus the ground state is always defined by the Luttinger-Tisza basic arrangement with the lowest eigenvalue. In particular there is a special ferromagnetic and an anti-ferromagnetic state, one of which – depending on the α rhombicity angle – defines the ground state.

Comparing the results in Tab. 5.1 and Tab. 5.2, it can be seen that the interaction of two neighboring lines almost saturates the long range dipole-dipole interaction. It is widely known that dipolar spheres due to dipole-dipole interactions tend to aggregate into chain like structures (see for example [256, 252] and references therein) in which the energies of intrachain interactions are much greater than those of interchain interactions [196]. These findings confirm that a two-line system, at least for local orderings, captures the most important properties of random dipole-dipole systems.

5.3 The effects of an interaction cutoff

Brankov and Danchev [26] observed that the ground state of a system of dipoles on an infinite rhombic lattice is sensitive to the dipole-dipole interaction range. An interaction cutoff distance R can be introduced in a natural way with a slight modification of Eq. (5.4) as

$$\mathbf{A}_{ij} = \sum_{\substack{j' \in \Gamma(j) \\ j' \neq i}} \mathbf{J}_{ij'} \Big|_{r_{ij'} < R} , \quad (5.9)$$

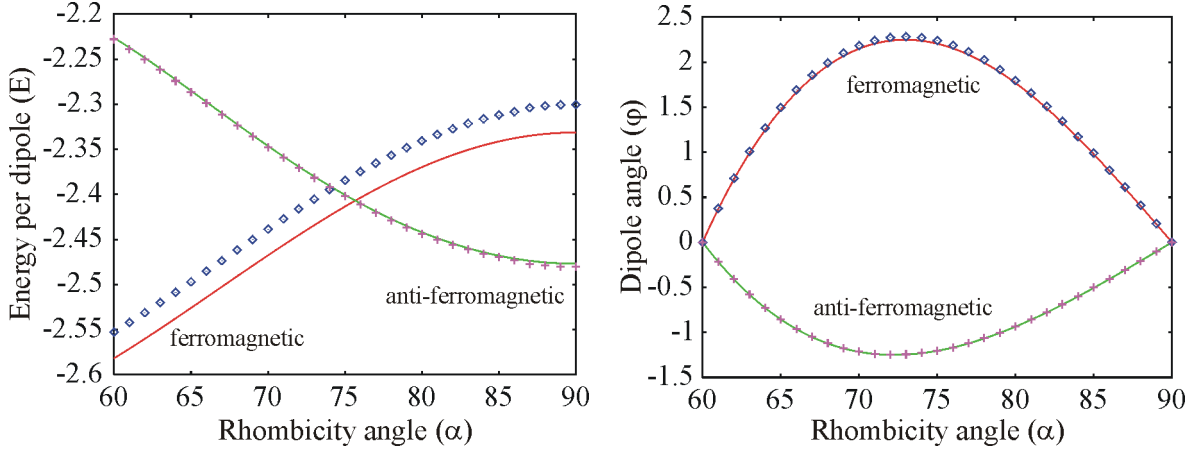


Figure 5.3: Numerical results for the two-line system at R equal to 10^6 (solid curves) and 8 (points). The left panel shows the lowest energy per dipole of the ferromagnetic and the anti-ferromagnetic state as function of the rhombicity angle. The energy is measured in units S^2/a^3 . The right panel shows the angle in degrees which the dipoles form with the direction of the longest linear dimension of the system.

where $r_{ij'}$ denotes the distance of two dipoles and the constraint $r_{ij'} < R$ limits the summation to pairs of dipoles which are closer to each other than the cutoff distance R . We measure the interaction cutoff in particle diameters equal to the lattice constant a .

The magnetic dipole-dipole potential decays with $1/r^3$ (where r is the distance of two dipoles), and thus the above expression for large R can be arbitrarily close to the long range limit. In fact, numerically the long range Luttinger-Tisza states are also calculated based on Eq. (5.9) using a very large R . Our numerical results for the two-line system at R equal to 10^6 and 8 are shown on Fig. 5.3. The results corresponding to $R = 10^6$ are close to the long range interaction limit within the numerical errors of 64 bit floating point arithmetic. Intuitively one may expect that in the ground state of the two-line system the dipoles are oriented parallel to the lines in both ferromagnetic and anti-ferromagnetic state. However, this is true only for $\alpha = 60^\circ$ and $\alpha = 90^\circ$. For any other α , the dipoles form a small angle with the lines.

Below a certain α , as can be seen on Fig. 5.3, the ground state of the system corresponds to the ferromagnetic order and above it to the anti-ferromagnetic order. The anti-ferromagnetic state remains almost unchanged as a consequence of the strong coupling of neighboring dipoles of opposite orientation, which seems to make the interaction cutoff irrelevant. As expected, the ferromagnetic state at $\alpha = 60^\circ$ and the anti-ferromagnetic state at $\alpha = 90^\circ$ are stable configurations independent of R , however, as R decreases the crossover point gets slightly shifted. E.g. at $R = 8$, the angle at which the transition from ferromagnetic to anti-ferromagnetic ground state takes place is shifted by 3%.

At low interaction cutoff distances ($R \lesssim 8$) the discrete nature of the system becomes more and more relevant and both the ferromagnetic and anti-ferromagnetic energy per dipole begin to exhibit sudden jumps in function of the rhombicity angle (see Fig. 5.4). As the interaction cutoff decreases the energy jumps become more and more relevant. This behavior can introduce spurious effects in simulations using a badly chosen cutoff distance. It must be noted, however, that one should not overestimate the importance of these effects

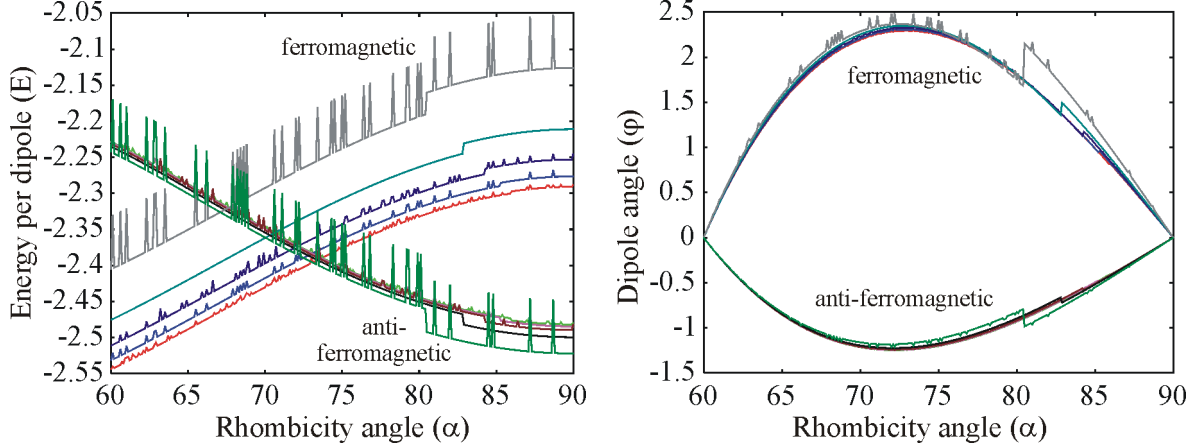


Figure 5.4: Numerical results for the two-line system at R equal to 7, 6, 5, 4, and 3. The left panel shows the lowest energy per dipole (in units S^2/a^3) of the ferromagnetic and the anti-ferromagnetic state as function of the rhombicity angle. In ferromagnetic state the curves are shifted upward as R decreases. The right panel shows the angle in degrees which the dipoles form with the direction of the longest linear dimension of the system.

as the energy jumps are relatively small.

According to Fig. 5.3 and Fig. 5.4, the ferromagnetic curve is shifted upward as R decreases. At the same time the anti-ferromagnetic state remains close to its long range limit, which means that the anti-ferromagnetic state becomes more and more dominant. For large R the ferromagnetic state at $\alpha = 60^\circ$ has lower energy per dipole than the anti-ferromagnetic state at $\alpha = 90^\circ$. Consequently, for long range forces in random systems ferromagnetic local arrangements are expected to occur more frequently. Our numerical results show that at $R \approx 4$ the situation is reversed. Therefore, at lower interaction cutoff values anti-ferromagnetic arrangements are more frequent. We have also noticed this in simulations presented at the beginning of this Chapter. In the two-line system, the ferromagnetic ground state disappears totally at $R \approx 2$. Brankov and Danchev [26] found that in case of an infinite rhombic lattice with rhombicity angle $\alpha = 60^\circ$ the ferromagnetic ground state disappears at $R \approx 3$.

5.4 Finite size correction

We have also investigated the finite size correction of the energy per dipole of the two-line system in ferromagnetic and anti-ferromagnetic states. In these states, the infinite system can be decomposed into identical finite segments. Consequently, the energy per dipole can be written as

$$E = \frac{1}{2N} \left[\frac{1}{2} \sum_{\substack{i,j \in \sigma(N) \\ i \neq j}} \mathbf{s}_i^T \mathbf{J}_{ij} \mathbf{s}_j \right] + \frac{1}{2N} \left[\frac{1}{2} \sum_{\substack{i \in \sigma(N) \\ j \in \sigma(N)^c}} \mathbf{s}_i^T \mathbf{J}_{ij} \mathbf{s}_j \right], \quad (5.10)$$

where N is the number of dipoles per line in a finite segment, $\sigma(N)$ denotes the dipoles belonging to one segment and $\sigma(N)^c$ is the complementer of $\sigma(N)$ (i.e. the rest of the

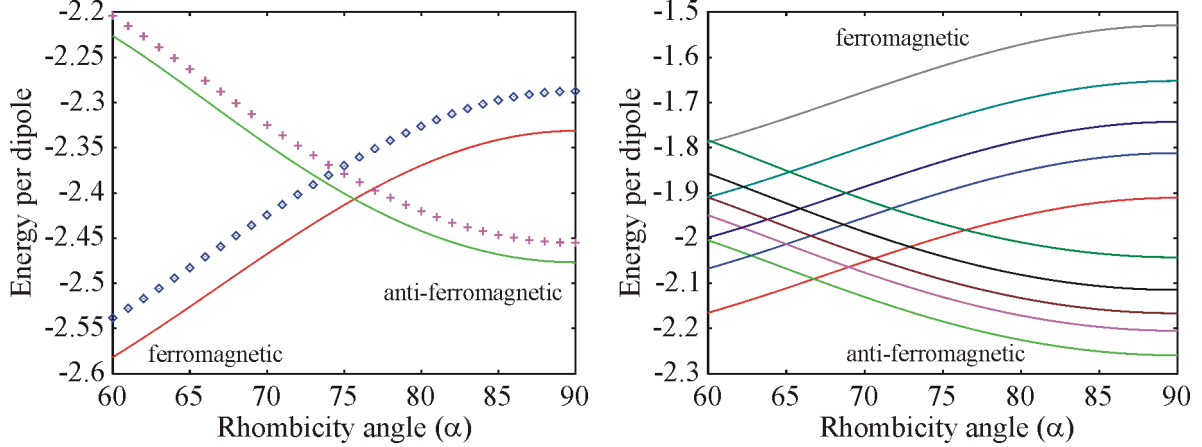


Figure 5.5: Dependence of the energy per dipole of the two-line system on the system size in the long range limit. The energy is measured in units S^2/a^3 . The left panel shows results for number of particles per line N equal to 10^5 (solid curves) and 100 (points). The right panel shows results for N equal to $10, 8, 7, 6$, and 5 . Both the ferromagnetic and the anti-ferromagnetic curves move upward as N decreases. (Note the different scales on the vertical axes.)

dipoles). The first part in the above expression can be recognized as the energy per dipole $\mathcal{E}(N)$ of a finite segment.

We define the quantity of energy dimension

$$\partial\mathcal{E}(N) = N \left[\mathcal{E}(N) - E \right] = -\frac{1}{4} \sum_{\substack{i \in \sigma(N) \\ j \in \sigma(N)^c}} \mathbf{s}_i^T \mathbf{J}_{ij} \mathbf{s}_j, \quad (5.11)$$

where, in case of an interaction cutoff R , similarly to Eq. (5.9), one may also add the constraint $r_{ij} < R$. Because \mathbf{J}_{ij} is proportional to $1/r_{ij}^3$ (see Eq. (5.2)) the limit

$$\partial E = \lim_{N \rightarrow \infty} \partial\mathcal{E}(N), \quad (5.12)$$

exists and is finite. Numerical calculations confirmed this statement. The convergence of $\partial\mathcal{E}(N)$ is of order $1/N$ in the ferromagnetic case and is of order $1/N^3$ in the anti-ferromagnetic case. For large N the energy per dipole of a finite system can be approximated as

$$\mathcal{E}(N) \approx E + \partial E/N. \quad (5.13)$$

Therefore we call ∂E the *finite size coefficient*.

In accordance with Eq. (5.13), $\mathcal{E}(N)$ for $N = 10^5$ gives a good approximation of E (see Fig. 5.5). It is, however, a surprising result that Eq. (5.13) works even for small N . As it can be seen on Fig. 5.6, the value of ∂E does not depend significantly on the rhombicity angle. This explains how the energy per dipole curve of a finite system on Fig. 5.5 is simply shifted upward as N decreases. The finite size coefficient of the ferromagnetic state is approximately two times larger than the finite size coefficient of the anti-ferromagnetic state, and thus the ferromagnetic curve moves upward approximately two times faster than the anti-ferromagnetic curve. For large N the ferromagnetic state at $\alpha = 60^\circ$ has lower

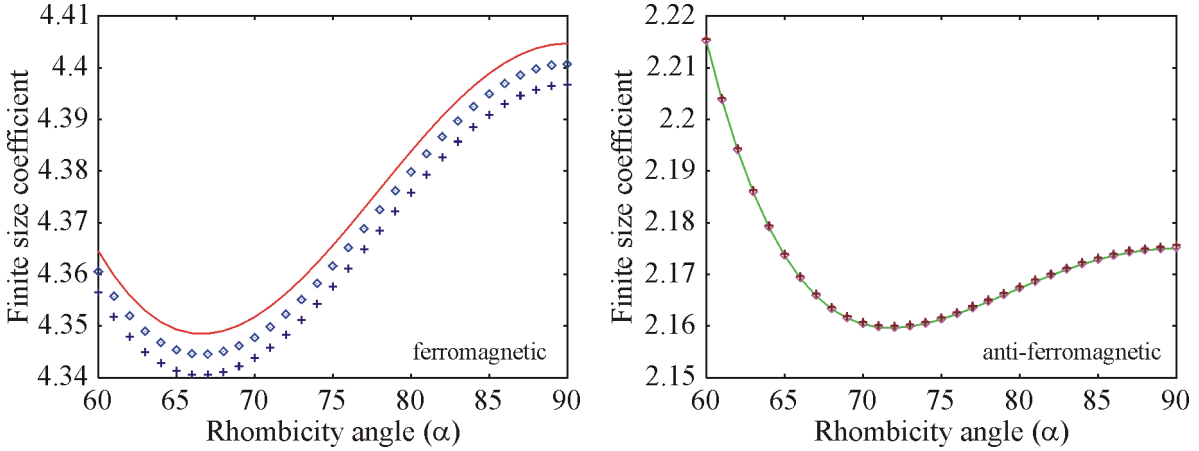


Figure 5.6: Finite size coefficient of ferromagnetic (left) and anti-ferromagnetic (right) states. The solid curve on both panels corresponds to $R = 10^6$. The points on the left panel correspond to R equal to 1000 and 500, and on the right panel to R equal to 100 and 50. The finite size coefficient is measured in units S^2/a^3 . In the ferromagnetic case the curves move downward as R decreases. (Note the different scales on the vertical axes.)

energy per dipole than the anti-ferromagnetic state at $\alpha = 90^\circ$. At $N = 20$ the situation is reversed and at $N = 5$ the ferromagnetic ground state disappears. This means that long chains (touching each other on long segments) prefer ferromagnetic arrangements, while short chains (or long chains touching each other on short segments) are more likely in an anti-ferromagnetic arrangement. This could be also observed in the simulations of dipolar particles presented at the beginning of this Chapter.

The finite size coefficient does also depend on the interaction cutoff. Fig. 5.6 and

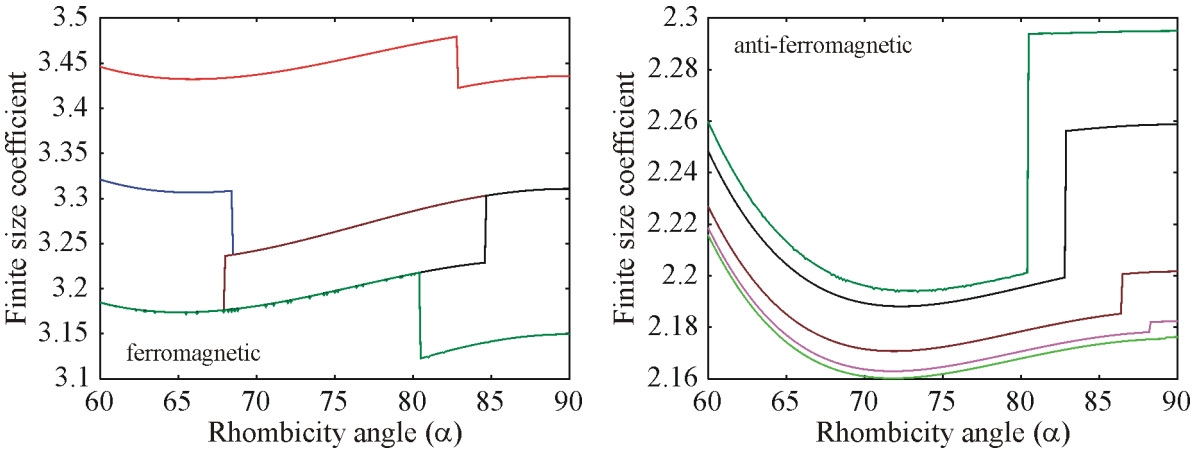


Figure 5.7: Finite size coefficient at low interaction cutoff distances. The left panel shows the finite size coefficient of the ferromagnetic state as function of the rhombicity angle at R equal to 4, 3.75, 3.5, 3.25, and 3. The curves move downward as R decreases. The right panel shows the finite size coefficient of the anti-ferromagnetic state at R equal to 40, 16, 8, 4, and 3. The curves are shifted upward as R decreases. (Note the different scales on the vertical axes.)

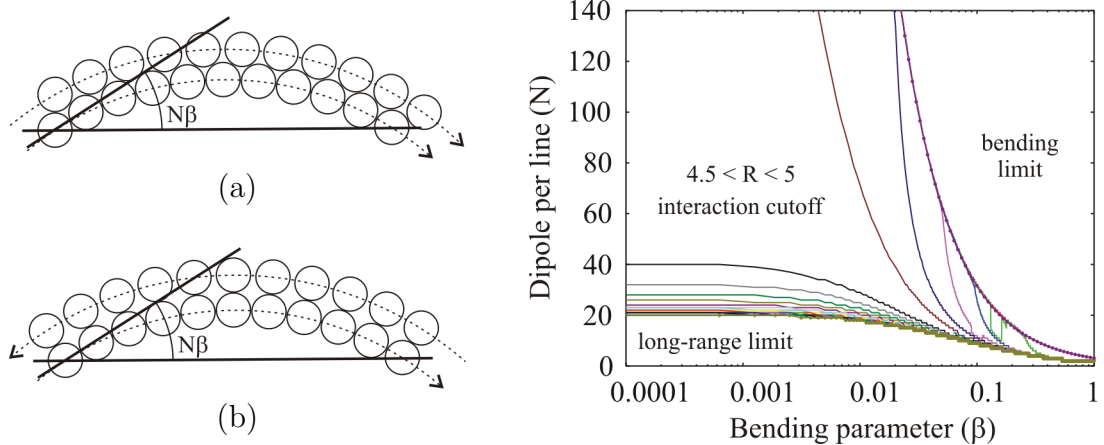


Figure 5.8: Bending a two-line system at different interaction cutoff values. Panels (a) and (b) show a finite system of bent two lines of dipolar hard spheres in ferromagnetic and anti-ferromagnetic states. The right panel shows (β, N) state diagrams (see text for description) for R ranging from 2 to ∞ . The curves move upward and right as R decreases.

Fig. 5.7 present results on this dependence. We calculated the finite size coefficient by evaluating the expression in Eq. (5.11) for $N = 10^5$. The results for $R = 10^6$ are close to the long range limit within the errors of 64 bit floating point arithmetic. As R is lowered in the anti-ferromagnetic case the finite size coefficient remains almost unchanged even for $R \approx 50$, while in the ferromagnetic case it decreases significantly already at $R \approx 1000$. This shows again that the ferromagnetic state is much more sensitive to the interaction cutoff than the anti-ferromagnetic state.

At lower interaction cutoff distances (at $R \lesssim 50$) the discrete nature of the system manifests itself in sudden jumps (see Fig. 5.7). The jumps in the finite size coefficient become bigger as the interaction cutoff decreases. These jumps are not relevant at large N , but they could introduce spurious effects at lower dipole numbers. However, we note again that these effects should not be overestimated as the introduced energy jumps are relatively small.

5.5 Bending two lines of magnetic particles

The finite size study presented before gives a good description of finite dipole systems for large N . At small N , for a better understanding of the system, we studied numerically the effect of bending two lines of dipolar hard spheres in ferromagnetic and anti-ferromagnetic states (see Fig. 5.8 (a) and (b)). In unbent case these correspond to the previously studied ferromagnetic state at $\alpha = 60^\circ$ and anti-ferromagnetic state at $\alpha = 90^\circ$. We introduce the bending parameter β and we define the bent system as composed of particles placed on an arc of angle $2N\beta$ and having dipoles tangential to the arc (see definition of β on Fig. 5.8 (a) and (b)). This involves a so called “bending limit” as the arc’s angle is limited to 2π , and thus β must satisfy the constraint $\beta \leq \pi/N$.

The numerical results show that for bending either a ferromagnetic or an anti-ferromagnetic two-line system some physical effort is needed. The two-line system in ferromagnetic state can be bent easier than in the corresponding anti-ferromagnetic state.

This is a consequence of the strong coupling of neighboring dipoles oriented anti-parallel. However, as the anti-ferromagnetic state is bent it becomes less and less stable. At different β and N , we compared the energy per dipole of the ferromagnetic and anti-ferromagnetic states and we identified (β, N) pairs at which these two states are energetically equivalent. We repeated this procedure at different R interaction cutoff values. The right panel of Fig. 5.8 shows the corresponding (β, N) state diagrams.

In the long range limit for small system size N and small bending parameter β the anti-ferromagnetic state has lower energy per dipole, and thus in random systems the anti-ferromagnetic segments are likely to be short and straight, while in general the local orderings are dominated by ferromagnetic arrangements. This is in accordance with our previous findings including distinct element simulations. It is, however, a surprising result that for interaction cutoff values between 4 and 5 this behavior is rapidly changed. For $R \lesssim 4$ the anti-ferromagnetic state remains more stable also at large N even for significantly large β . This means that the general characteristics of an arbitrary dipole system for $R \lesssim 4$ are substantially changed and local orderings are dominated by anti-ferromagnetic arrangements.

5.6 Conclusions and discussion

Theoretical results and distinct element simulations of magnetic granular systems show that there are two relevant dipole arrangements: (1) a ferromagnetic state with dipoles organized in a triangular lattice, and (2) an anti-ferromagnetic state with dipoles organized in a square lattice. Based on the fact that dipolar spheres due to dipole-dipole interaction tend to aggregate into chains in which the ratio of interchain-to-intrachain interactions is small and the interaction of parallel chains of dipolar hard spheres almost saturates the dipole-dipole interaction in two-dimensional dense systems, we argue that a system of two parallel dipole lines is a characteristic local structure which captures the main aspects of the behavior of general random dipolar granular systems.

Our numerical results on dipolar two-line systems show that the ferromagnetic state is much more sensitive to the interaction cutoff R than the corresponding anti-ferromagnetic state. This can be explained by the efficient coupling of dipoles oriented anti-parallel. For large R (e.g. $R \gtrsim 8$ particle diameters) there is no substantial change in the energetic balance of the ferromagnetic and anti-ferromagnetic states and the ferromagnetic state slightly dominates over the anti-ferromagnetic state. This is reversed for low interaction cutoff values. The ferromagnetic ground state in a two-line system disappears completely at $R \approx 2$ (measured in particle diameters). Brankov and Danchev [26] found that in case of an infinite triangular lattice the ferromagnetic ground state disappears at $R \approx 3$. Based on our numerical calculations and on distinct element simulations, for $R < 4$ the anti-ferromagnetic arrangements occur more frequently in random systems.

We have also introduced a so called “finite size coefficient”, which describes the finite size behavior of a sufficiently long two-line system in ferromagnetic or anti-ferromagnetic state. We observed that the finite size coefficient is sensitive to the interaction cutoff for both ferromagnetic and anti-ferromagnetic states, being more sensitive for the ferromagnetic state. We found that for infinite range interactions long chains prefer ferromagnetic arrangements, while short chains are more likely in an anti-ferromagnetic arrangement. The transition point is around a chain length of 20 particles. Introducing an interaction

cutoff, makes the anti-ferromagnetic arrangements less stable and enables longer chain pairs in anti-ferromagnetic state. This effect was further evidenced by bending finite ferromagnetic and anti-ferromagnetic two-line systems with N number of dipoles per line. We characterized the bending angle with a parameter β , and created (β, N) state diagrams separating energetically favorable ferromagnetic and anti-ferromagnetic states. We observed that there is a substantial change on these state diagrams around $R \lesssim 4$. In accordance with distinct element simulations, we argue that, if one is interested in local orderings, $R \approx 5$ (measured in particle diameters) is the lowest reasonable choice for dipole-dipole interaction cutoff in two-dimensional dipolar granular systems.

Let us note that here we focused on local particle orderings, because these are known to be crucial for the behavior of granular systems. In a more precise approach the long range magnetic correlations and the magnetic response functions should be also considered. In general, these are more strongly affected by an interaction cutoff than the local structures and energy densities considered here. In principle an Ewald summation method [64, 251] would allow to explore the response properties in the thermodynamic limit in terms of large but finite systems with periodic boundary conditions. In a recent article, Politi et al. [180], regarding the dipolar ground state of planar spins on a triangular lattice, discussed how long-range order is affected by the size and the shape of the lattice as well as what kind of higher order effects are introduced by an interaction cutoff.

Chapter 6

Granular piles and avalanches of magnetized particles

The study of granular systems with magnetic interactions forms a promising approach (see Section 2.5) to the understanding of the general behavior of cohesive systems determined by the competition between interparticle and inertial forces. The interaction between particles carrying magnetic dipoles can be viewed as an anisotropic adhesion force, and thus iron spheres placed in a magnetic field forms a model of cohesive granular systems [82, 108]. Varying the strength of the magnetic field allows to continuously vary the magnetization of the particles and hence the strength of the interparticle forces, which are in overall attractive. This makes it possible (and relatively easy) to study the transition from noncohesive to cohesive behavior. It is, however, a question to what extent is this modeling allowed, i.e., what are the similarities and the differences between magnetic and ordinary cohesive systems such as wet granular materials and dry fine powders.

In this Chapter, we present computer simulations of a magnetic system similar to the one studied experimentally by Forsyth et al. [82, 108]. We used a magnetic interaction cutoff, which – based on the results of Chapter 5 – assures that the local orderings playing a principle role in the behavior of granular systems are realistic. In order to be able to compare with experiments [82, 108], the angle of repose and the surface roughness of particle piles was measured at different magnetizations. In addition, we studied the effect of magnetization on avalanches formed on the piles. In the next Sections, we first outline the used simulation method and the simulation setup. Later, we show that in accordance with the experimental results [82, 108] both the angle of repose and the surface roughness exhibits a linear dependence on the strength of the magnetic interactions. We also show that there is a difference in avalanche formation mechanism at small and at large magnetizations. This defines two regimes. Based on a stability criteria, we give a plausible estimate of the transition point between these regimes and we discuss their characteristics.

6.1 Computational method

We performed computer simulations using a standard two-dimensional Distinct Element Method¹ (DEM) [44]. The particles were magnetized by a constant external field, all having the same magnetic orientation parallel to the field. The magnetization was modeled

¹For an overview see Chapter 4.

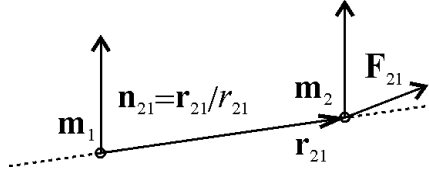


Figure 6.1: Dipoles \mathbf{m}_1 and \mathbf{m}_2 at relative position \mathbf{r}_{21} . The force acting on \mathbf{m}_2 as a result of the dipole-dipole interaction with \mathbf{m}_1 is denoted by \mathbf{F}_{21} .

with dipoles. We neglected any coupling between the magnetic orientation and particle rotation, i.e. the particles could rotate freely, while their magnetic dipole was fixed.

The magnetic force acting on a dipole \mathbf{m}_2 situated from dipole \mathbf{m}_1 at distance r_{21} along the direction $\mathbf{n}_{21} = \mathbf{r}_{21}/r_{21}$, oriented as shown on Fig. 6.1, is²

$$\mathbf{F}_{21} = \frac{\mu_0}{4\pi} \frac{3}{r_{21}^4} [(\mathbf{n}_{21}\mathbf{m}_2) \mathbf{m}_1 + (\mathbf{n}_{21}\mathbf{m}_1) \mathbf{m}_2 - 5 (\mathbf{n}_{21}\mathbf{m}_1) (\mathbf{n}_{21}\mathbf{m}_2) \mathbf{n}_{21} + (\mathbf{m}_1\mathbf{m}_2) \mathbf{n}_{21}]. \quad (6.1)$$

According to the above formula, the largest possible dipole-dipole magnetic force acting between identical hard spherical particles of diameter D and magnetic dipole S , is

$$F_m = \frac{\mu_0}{4\pi} \frac{6S^2}{D^4}. \quad (6.2)$$

This corresponds to the head-to-tail configuration of aligned dipoles. Let us note that this is the energetically most favorable configuration. Consequently, magnetic particles tend to aggregate into chain like structures [256, 252].

For characterizing the strength of the interparticle magnetic force, we introduce a dimensionless *interparticle force ratio* f defined by the ratio of the maximum magnetic force at contact F_m and the gravitational force $F_g = mg$, where m denotes the particle mass and g is the gravitational acceleration. Considering mass density ρ and magnetization M , we have $m = \rho V$, $S = MV$, $V = \pi D^3/6$, and thus

$$f = \frac{F_m}{F_g} = \frac{\mu_0}{4\pi} \frac{6S^2}{mgD^4} = \frac{\mu_0}{4\pi} \frac{\pi M^2}{\rho g D}. \quad (6.3)$$

Assuming some interparticle force ratio f , the corresponding magnetization can be calculated as

$$M = \left(f \frac{4\pi \rho g D}{\mu_0 \pi} \right)^{1/2}. \quad (6.4)$$

We used $\rho = 7.5 \text{ g/cm}^3$, i.e. approximately to the mass density of steel, normal gravity $g = 9.8 \text{ m/s}^2$, and interparticle force ratio $f \leq 24$. The particle diameters were taken from the $0.7 - 0.9 \text{ mm}$ interval. The mean particle diameter was $D = 0.8 \text{ mm}$. Consequently, the largest magnetization was around $M = 67.02 \text{ emu/cm}^3$.

The particle size distribution was given by the average of 4 independent uniformly distributed random variables (see Fig. 6.2). This approximates a Gaussian distribution

²The formula is derived in Appendix D.

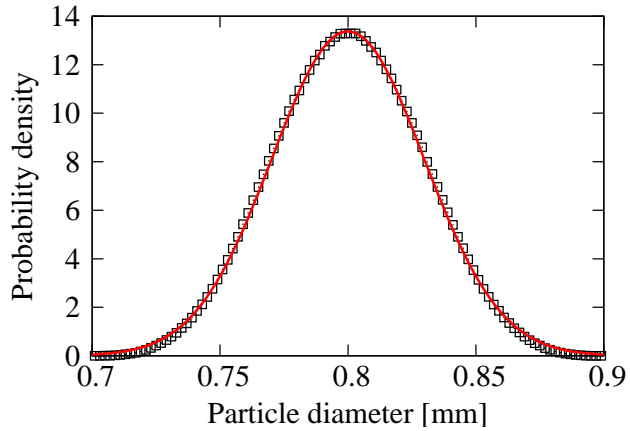


Figure 6.2: Particle diameter distribution (points) given by the average of 4 independent random variables uniformly distributed in the [0.7, 0.9] mm interval. This distribution approximates a Gaussian distribution (line).

with standard deviation $\Delta D = 29.8 \mu\text{m}$, cut at $3.35 \Delta D$ around the mean value. This weak polydispersity, resembling experimental setups, was used to avoid effects originating from symmetries of monodisperse systems. Our system is polydisperse enough that crystalline order is avoided in the absence of a magnetic field. However, let us recall, that the magnetic interaction favors a triangular lattice with ferromagnetic ordering.

The long range magnetic interaction was taken in consideration within a cutoff distance of $6.25D$. As it was noted for example by Altshuler et al. in [9], the angle of repose, the surface roughness, and the particle avalanches depend crucially on local orderings inside the pile. In Chapter 5, we have shown that regarding local ordering in two-dimensional systems a value of $5D$ would already give a reasonable interaction cutoff distance. A cutoff larger than this assures that the character of local orderings is realistic and close to the case of infinite range interactions.³ Relative to this, the estimated deviation in the magnetic energy per dipoles introduced by the interaction cutoff was less than 5%.

The choice of the interaction cutoff is further justified by the fact that even for the strongest magnetization (corresponding to $f = 24$) considered in this study the magnetic interactions beyond the cutoff are negligible as compared to the first-neighbor magnetic forces as well as the gravitational force acting on the particles. As it was already mentioned, the magnetic interaction is the largest if the dipoles are aligned into a head-to-tail configuration. The interaction force at the cutoff distance $r_{21} = 6.25D$ is smaller than the force at the most favorable contact position by a factor of $1/1525 \approx 0.65 \cdot 10^{-3}$. If the relative position of the particles is less favorable, then we have even smaller forces. This means that the magnetic forces originating from grains outside the cutoff distance are at least 3 orders of magnitude smaller than the first-neighbor forces. These forces are significantly smaller than the gravitational force too. The proportionality factor is $24/1525 \approx 1.6 \cdot 10^{-2}$ or smaller. Therefore, it is reasonable to neglect them.

For calculating the normal repulsive particle-particle contact forces we used the Hertz model [133] combined with appropriate damping [129, 30]. In addition, we implemented Coulomb sliding friction for large relative translational velocities. For numerical stability

³See Section 5.6 for a discussion on possible higher order corrections.

we used viscous friction at small velocities, with a continuous transition to sliding friction (see Fig. 4.4). The viscous friction was controlled by a coefficient $\lambda = 10 \text{ kg/s}$ chosen such that it played a role only up to velocities in the order of magnitude of velocities gained by particles in free fall during one simulation time step. For simplicity, we have not used any static or rolling friction model. A grid based lookup method was used to identify the neighboring and potentially colliding particles.

The parameters of the Hertz contact model were chosen such that they correspond to Young modulus of approximately 15 MPa and restitution coefficient of approximately 0.86. These are characteristic values for hard rubber elastomers (used for example in constructing golf ball covers). The particle-particle and the particle-wall sliding friction coefficient was 0.5 and 0.7 (characteristic to steel-steel and steel-perspex friction).

Let us note that the above Young modulus is some orders of magnitudes smaller than the Young modulus of steel. This choice was necessary for acceptable CPU times. Nevertheless, based on our detailed numerical investigations, the outcome of the simulations – as packing, coordination number, force chains, force distribution, etc., which are known to determine the behavior of granular systems – with the parameters we were using, are essentially those which are found in experiments.

The translational motion of the particles was calculated based on Newton’s equation using Verlet’s Leap-Frog method. The rotational degree of freedom was integrated with Euler’s method. The integration time step was $5 \mu\text{s}$. For the used elastic parameters, $170 \mu\text{s}$ gives a good estimate of average collision times. In such conditions, with the above integration time step good numerical stability and also fairly good response time could be reached on standard PCs with 1.8 GHz AMD AthlonTM CPUs.

6.2 Simulation setup

The simulation setup can be seen on Fig. 6.3. Similarly to the experiments of Forsyth et al. [82, 108], the external magnetic field was vertical. The particles were added one by one with constant rate along vertical trajectories at small (maximum one particle diameter) random distance from the left wall. They either reached the pile with a large velocity, i.e. *they were fired into the pile*, or their impact velocity was set to zero, i.e. *they were placed gently on the pile*. The system’s bottom wall was sticky. Any particle touching the bottom wall stucked to it. This built up a *random base*.⁴ The particles could leave the system on the right side. The particles were removed from the simulation when their distance from the bottom-right corner was larger than the magnetic interaction cutoff distance. The width of the system was $51.25D$.

The *surface particles* (marked with black on Fig. 6.3) were identified with the *weighted alpha shape algorithm* [60, 6]. Alpha shapes are generalizations of convex hull and can be used for shape reconstruction from a dense unorganized set of data points. The weighted alpha shapes are extensions of this kind of shape reconstruction to a set of circles. We used the implementation included in the Computational Geometry Algorithms Library [36]. The algorithm’s *alpha* parameter was set to the square of the mean particle size. This gave satisfactory results. The angle of repose was measured by fitting a straight line over the position of the surface particles.⁵ The surface roughness was given by the standard

⁴See the experimental setup used by Altshuler et al. described in [9].

⁵The simulation conditions made no possible to distinguish the angle of repose and the angle of stability.

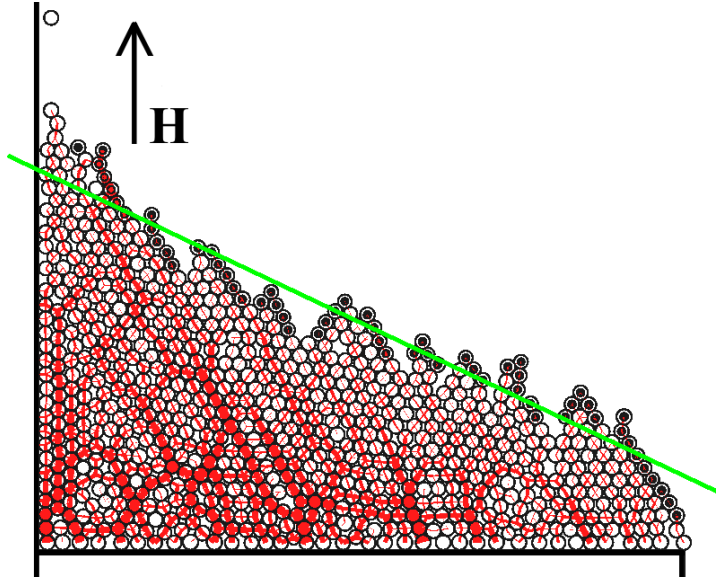


Figure 6.3: Simulation setup. The particles are introduced with constant rate one by one at small random distances from the left wall. The external magnetic field is vertical. The particles can leave the system on the right hand side. The shown snapshot corresponds to interparticle force ratio $f = 6$. The force chains are also shown.

deviation of the surface points from the fitted line.

With a special *side wall model*, we also simulated the effect of the front and back walls of a quasi-two-dimensional Hele-Shaw cell encountered in experimental studies. We took into consideration the frictional interaction with side walls by summing up the magnitude of the normal forces acting on one particle. We directed a certain percentage of this *pressure* on the walls and derived a frictional force using the already mentioned friction model. The percentage of the total force directed on the side walls was a simulation parameter.

We performed three sets of simulations: (a) the particles were fired into the pile, (b) the particles were placed gently on the pile, and (c) the particles were fired into the pile, while 4% of the internal *pressure* was directed on the *front and back walls*. In both (a) and (c) the particles reached the pile with approximately 0.5 m/s impact velocity, which corresponds to $16D$ dropping height. In all three simulation sets we executed runs at different interparticle force ratios. In each run, we started with an empty system. For $f > 0$ introducing 12000 particles, we simulated the system for 3 minutes (simulated time). Simulating at zero magnetization ($f = 0$), our computer program was about 10 times faster, because only the repulsive contact interactions had to be calculated. This permitted longer simulation runs introducing a total of 144000 particles and integrating the system for 36 minutes.

In the first part of the process the number of particles in the system increased monotonically. After a pile was built, avalanches started and moved particles out of the system in a pulsating manner. In this way the number of particles began to oscillate around some value. In this latter part of the simulation we identified the surface particles at each 500th integration step, and we measured the slope of the fitted surface line and the standard

For a definition of these two angles see Section 2.1.

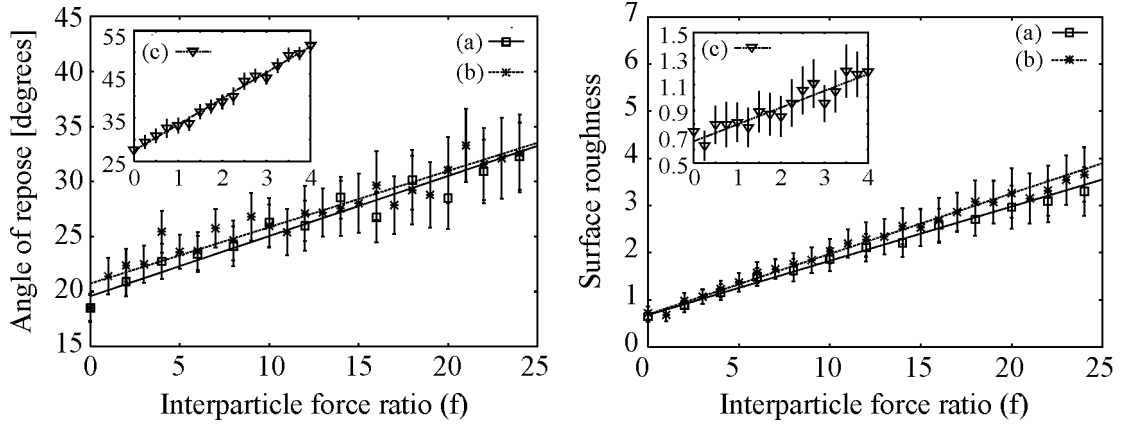


Figure 6.4: Angle of repose (left panel) and surface roughness (right panel) at different magnetic interparticle force ratios. The angle of repose is measured in degrees. The surface roughness is measured in (average) particle diameters.

deviation of the surface points from this line. The average of these quantities over the simulated time gave the angle of repose and the surface roughness.

We also measured the avalanche durations and avalanche sizes. Particles were introduced at each 3000th integration step, which means one particle in 15 ms. This was the smallest avalanche duration we recorded. By definition, two avalanches were separated by a “quiet” interval (time without particles leaving the system) of this length. The number of particles leaving the system during an avalanche defined the avalanche size.

6.3 Angle of repose and surface roughness

For the examined magnetization range, we found in all three simulation sets (a), (b), and (c) that both the angle of repose and the surface roughness has a linear dependence on the interparticle force ratio (see Fig. 6.4). The angle of repose in case (a) and (b) increases by approximately 0.5 degrees per unit change of interparticle force ratio (see left panel of Fig. 6.4). This is in very good agreement with the experimental results of Forsyth et al. [82, 108], however, the angle of repose at zero magnetization in our case is about 10 degrees smaller. This could be the result of the missing side wall effect (see for example [92, 58]) or the missing static and rolling friction (see for example [263, 264]). Switching on the side wall model in case (c), the angle of repose at zero magnetization increased with about 8 degrees in agreement with experimentally observed effects [82, 108]. We found that the side walls induce a stronger increase of the angle of repose with f (see the inset of the left panel of Fig. 6.4), however, the dependence remains linear.

Peters and Lemaire [177], measuring the increase of the angle of repose under weak rotating magnetic fields, reported a slightly sublinear dependence on f (see Section 2.5). Our simulations seem to be in agreement with the results of Peters and Lemaire [177] too: The very accurate data point at $f = 0$ lies below the linear extrapolation of the data points for $f \geq 1$ (see (a) and (b) on left panel of Fig. 6.4). This indicates that in the $0 \leq f \leq 1$ range, deviations from linearity may occur. However, the side wall effects seem to suppress this sublinearity (see (c) on left panel of Fig. 6.4).

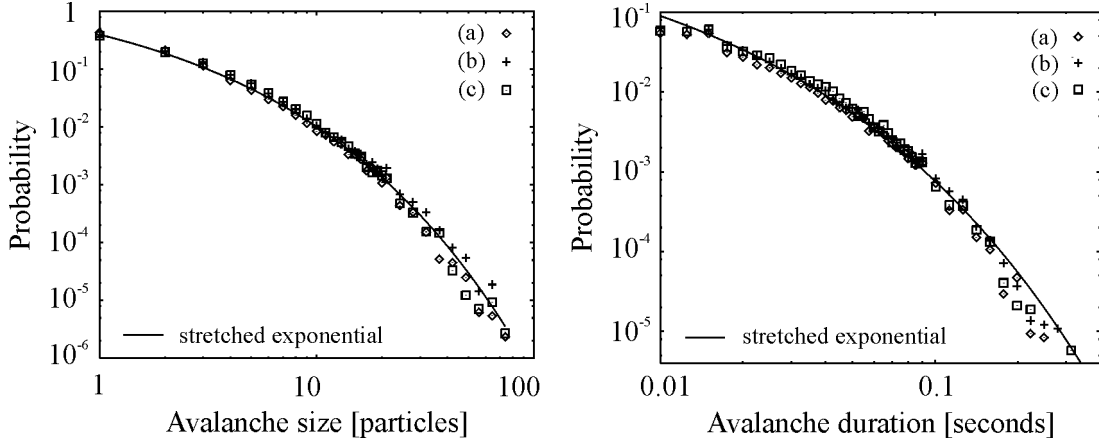


Figure 6.5: Distribution of particle avalanche sizes (left panel) and avalanche durations (right panel) at zero magnetization. At small avalanche size and duration linear binning, at large avalanche size and duration logarithmic binning was used.

Regarding the average surface roughness, we found that at zero magnetization it is about 0.7 particle diameters and in all simulation sets increases with approximately 0.12 particle diameters per unit change of the interparticle force ratio (see right panel of Fig. 6.4). This is again in agreement with the observations of Hutton [108] (from the same experiments as described by Forsyth et al. [82]) who found that as the field increases the surface becomes more and more irregular. We found that the side wall effect does not influence the surface roughness (see inset of right panel on Fig. 6.4).

The good agreement of our results with the experiments of both Forsyth et al. [82, 108] and Peters and Lemaire [177] is especially interesting in the light of the fact that our simulations employed an interaction cutoff. On one hand, this proves that the cutoff was chosen correctly. On the other hand, it suggests that at least in some aspects the infinite range of the interaction is less significant for the behavior of magnetic granular systems than it could be expected at first sight.

6.4 Particle avalanches at zero magnetization

To test the used simulation method and to validate the results which are going to be presented later, we have examined the distribution of particle avalanches at zero magnetization in all three simulation sets. We compared the results with the data available in the literature. The found size and duration statistics of avalanches are shown on Fig. 6.5. For a more clear picture of the statistics, we used linear binning at small sizes and durations and logarithmic binning at large sizes and durations.

Our simulations could not reproduce self-organized criticality. This concept, originally introduced for a sandpile model [13, 14] (see Section 2.2), inspired the description of many slowly driven nonequilibrium systems which present a scale-invariant dynamics with power-law distribution of event sizes. However, many experiments on real sandpiles [111, 184, 63] could not confirm such a scale invariant distribution.

A recent work of Costello et al. [41] presents experimental results on piling of uniform spherical glass beads, showing a power law behavior with an exponential cutoff. Costello

et al. [41] argue that the exponential cutoff depends on the height from which the particles are dropped and probably also on cohesion forces. Because of high computational needs, in our simulations the particles are introduced with a predetermined constant rate, while in the experiments a new particle was introduced only after the system was fully relaxed. Furthermore, the experiments of Costello et al. [41] were done in three dimensions, while our simulations are two-dimensional. With such differences, our simulations cannot support their findings.

Firing the particles into the pile, i.e. dropping them from a given height, or placing them gently, and switching on and off the side wall effect have not led to any qualitative difference (see Fig. 6.5). Over both the size and the duration distribution of the avalanches we could fit stretched exponentials of the form

$$P(x) = P_0 \exp[-(x/x_0)^\gamma] \quad (6.5)$$

using $\gamma = 0.43$. This is in good agreement with the experimental findings of Feder [75], who argued that a stretched exponential with γ between 0.34 and 0.44 can explain the data he analyzed. Our results are in agreement also with the results of Frette et al. [86], who found the same γ for piles of rice with small anisotropy.

6.5 Effect of magnetization on avalanches

Setting different magnetizations, we found that the magnetized particles near the free surface of the piles tend to organize into long clusters, which result in the already mentioned roughening. Such a cluster of particles during avalanching may disintegrate into narrower clusters or even into individual chains, or may be stable, depending on whether or not the magnetic interaction is strong enough to prevent the dilation necessary for the relative motion of chains within the cluster. Furthermore, we found that the avalanches are irregularly spaced in time and the larger the avalanche size, the larger is also the time interval between the avalanches because the steady state condition imposes an average flux of one particle per 3000 time steps.

Based on these, we argue that combinations of roughening and splitting determine the size of the outflowing clusters, which typically consist of w parallel chains of length N . Both w and N depend on f . Splitting can be observed on the consecutive simulation snapshots (see Fig. 6.6) taken at $f = 3$ and $f = 7$, while at $f = 24$ there is no splitting. Based on our measurements, the surface roughness increases linearly with f (see Fig. 6.4), consequently the chain length in the outflowing clusters is proportional to f . In order to check to what thickness w_{max} such a cluster is stable with respect to splitting into subclusters with less chains, we compared numerically the magnetic energy loss with the gravitational energy gained, when one chain is blocked while the rest of the cluster moves down by half particle diameter (see inset of Fig. 6.7).

The points on Fig. 6.7 correspond to equal magnetic energy loss and gravitational energy gain calculated at different chain lengths N and cluster widths w . Our numerical results show that the dipole-dipole interaction can only prevent cluster splitting if the cluster consists of less than $w \approx 1 + f/6$ chains. This means that a cluster of two chains can be stable only for $f > f_c \approx 6$. Below this value one expects strong splitting. This argument is certainly oversimplified: Taking it literally, we could conclude that there should be a sequence of transitions from avalanches consisting of individual chains to those

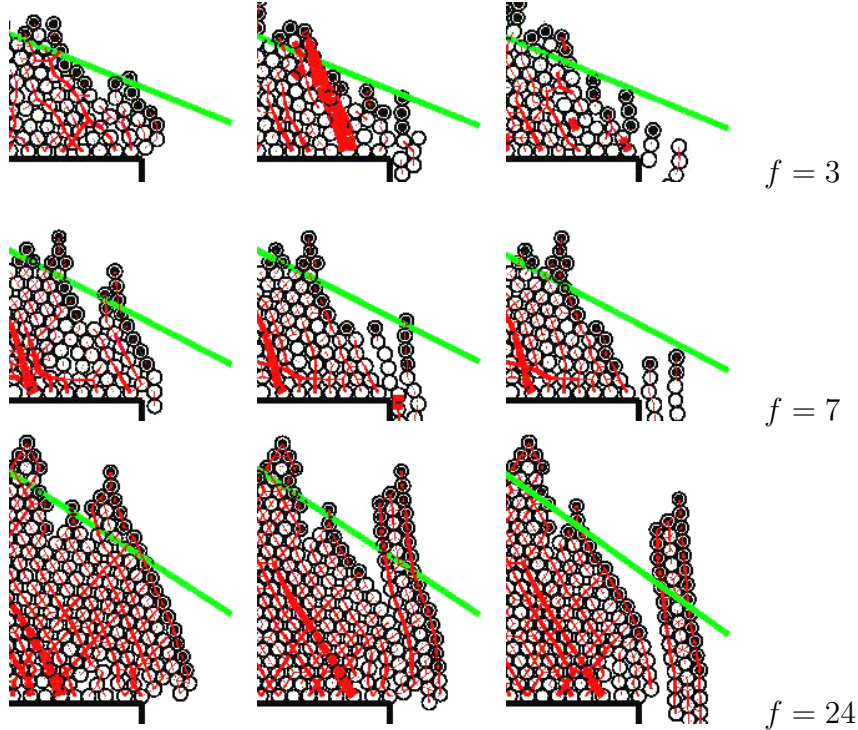


Figure 6.6: Consecutive simulation snapshots. Each row corresponds to a different value of f . Only the system's lower right corner is shown. The external magnetic field is vertical. The particles are placed gently on the pile (see the (b) simulation set). Particles leave the system, falling at the system's boundary on the right hand side.

of chain pairs, then to triples and so forth. We do not find any evidence for this. In fact, many other effects can also influence the width of a large cluster such as crack propagation, reorientation, and buckling, which suppress the further transitions.

Based on the above results we can describe the avalanche formation process as follows: Already at small magnetizations the surface roughness allows for coherent motion of larger clusters up to chain length $N_{max} \propto f$. For $f < f_c \approx 6$ clusters consisting of more than one chain of particles can easily dilate and will disintegrate into isolated chains, forming a quasi-continuous flow, which defines a *granular regime*. For $f > f_c$, large clusters consisting of $w > 1$ chains can fall. This defines a *correlated regime*. These results are close to the observations made in the simulations where the transition between the two regimes was found at $f_c \approx 7$. Some animations from our simulations revealing this transition were made public on the Internet [69].

To present the difference between these regimes, at given f , for each avalanche size we determined the average avalanche duration. We found that, in the granular regime the avalanche sizes are proportional to the corresponding average avalanche durations (see left panel of Fig. 6.8). The proportionality factors (i.e. the slope of the lines on the left panel of Fig. 6.8) decrease with f . Contrary, in the correlated regime the avalanche sizes are proportional to the square of the average avalanche durations, with no further dependence on f (see right panel of Fig. 6.8). In the next Sections, we present more details on the characteristics of the two regimes and we demonstrate that they exhibit different properties of avalanche size and duration statistics.

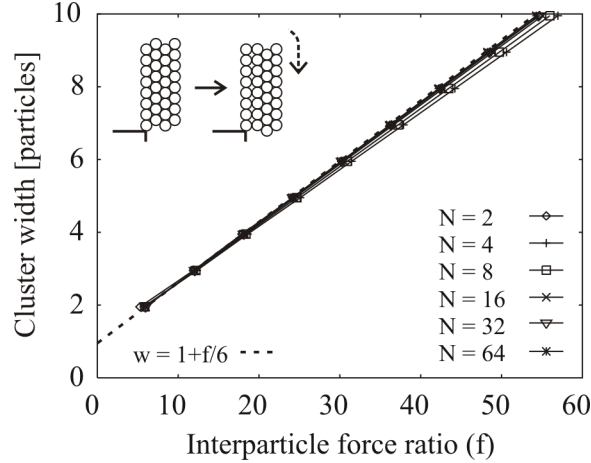


Figure 6.7: Numerical results on cluster stability. At different chain lengths N and cluster width w the loss in magnetic energy and the gain in gravitational energy was compared when one chain is blocked while the rest of the cluster moves down by half particle diameter (see inset). The dashed line shows the $w = 1 + f/6$ function.

6.6 The granular regime

In the granular regime, the large avalanches consist of many individual chains dropping consecutively over the edge (see the simulation snapshots taken at $f = 3$ on Fig. 6.6). The avalanche duration is dominated by the number of these chains, rather than their length which is proportional to f . Therefore one expects that the avalanche duration τ behaves as s/f , where s denotes an avalanche size. In full agreement with this, we observe (see left panel of Fig. 6.8) that the average duration of avalanches is proportional to their size (measured in number of particles) and the proportionality factor (i.e. the slope of the

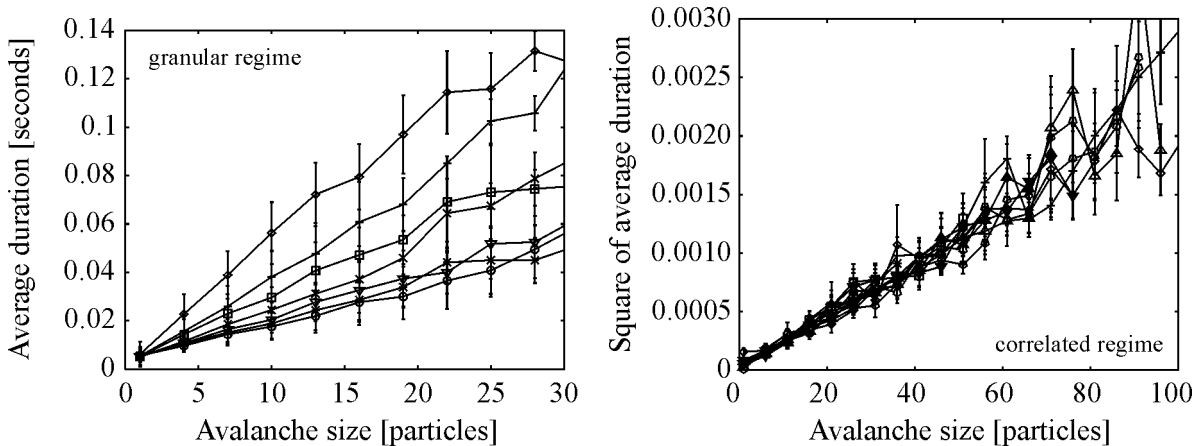


Figure 6.8: Dependence of average avalanche duration on avalanche size. The connected points correspond to equal f values. The error bars show standard deviation. Observe that on the right panel the square of the avalanche duration is shown. The data corresponds to the simulation set (b). Similar results were also found for the simulation set (a).

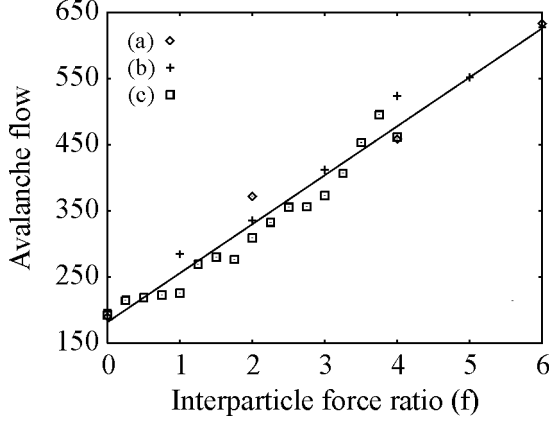


Figure 6.9: Average avalanche flow (s/τ) as function of the interparticle force ratio (f) in the granular regime. The flow is measured in particle per seconds. We observe the same linear dependence in all the three simulation sets (a), (b), and (c).

lines) decreases as $1/f$. This is also proved by the found linear dependence on f of the average avalanche flow s/τ (see Fig. 6.9).

The avalanche size distribution at interparticle force ratios $1 < f < 7$ can be scaled together reasonably well (see Fig. 6.10) using the ansatz

$$P(s, f) = f^{-1}Q(s/f), \quad (6.6)$$

where $P(s, f)$ is the probability associated with the avalanche size s at a given f , and Q is a function with unit integral on $[0, +\infty)$. Based on the shape of the scaled distributions shown on Fig. 6.10, we argue that the magnetic cohesion introduces a characteristic avalanche size. From the scaling property, we conclude that this characteristic size increases linearly with the strength of the interparticle forces. Qualitatively similar results were found in experiments by Szalmás et al. [217].

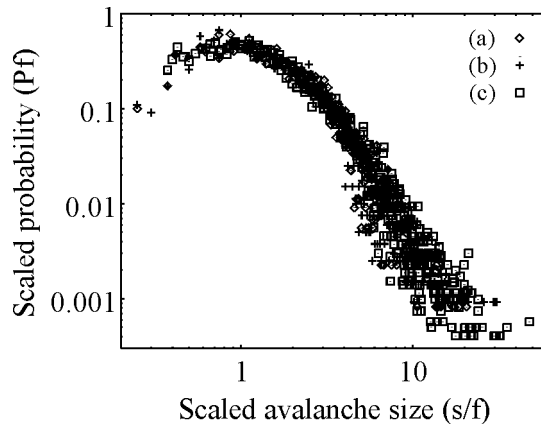


Figure 6.10: Scaled avalanche size distribution in granular regime. We examined three different simulation setups ((a), (b), and (c)). The avalanche size distribution at interparticle force ratios $1 < f < 7$ are scaled together using the ansatz $P(s, f) = f^{-1}Q(s/f)$, where s denotes avalanche size.

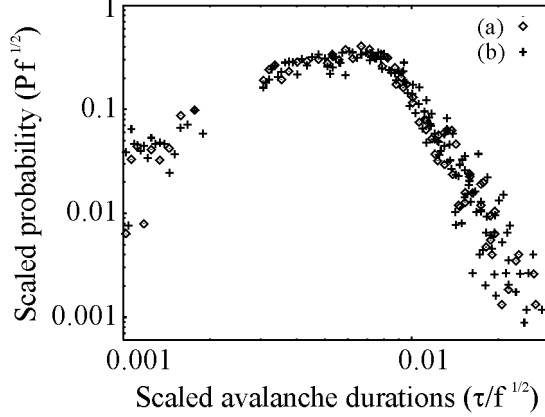


Figure 6.11: Scaled avalanche duration distribution in correlated regime. We examined two simulation setups ((a) and (b)). The avalanche duration distribution at interparticle force ratios $7 < f \leq 24$ are scaled together using the ansatz $P(\tau, f) = f^{-1/2}Q(\tau/f^{1/2})$, where τ denotes avalanche durations.

6.7 The correlated regime

For $f > 7$ the average duration τ of avalanches of size s behaves markedly different than in granular regime: It is proportional to \sqrt{s} and has no further dependence on f (see right panel of Fig. 6.8). The reason is that in the correlated regime a typical avalanche duration is determined by the free fall of a long cluster (see the simulation snapshots taken at $f = 24$ on Fig. 6.6). Accordingly, the square of the avalanche duration is proportional to the vertical extent (i.e. the length) of the falling cluster. Though, it can fluctuate, the width w of a falling cluster is mainly independent of magnetization, while the length of the clusters is determined by roughness scaling linearly with f . Therefore, the average cluster size is $s \propto wf \propto f$ and hence $\tau \propto \sqrt{f}$, which is indeed verified by the data collapse of the avalanche duration statistics shown on Fig. 6.11.

The avalanche duration distributions $P(\tau, f)$ at interparticle force ratios $7 < f \leq 24$ can be scaled together (see Fig. 6.11) using the ansatz

$$P(\tau, f) = f^{-1/2}Q(\tau/f^{1/2}), \quad (6.7)$$

where Q has unit integral on $[0, +\infty)$. The shape of the scaled duration distributions shows a characteristic avalanche duration. According to the above scaling property, we argue that this characteristic duration is proportional to \sqrt{f} .

During transition from granular regime to correlated regime, as the magnetization increases, the characteristic avalanche size (measured in number of particles) found in the granular regime is suppressed more and more and practically disappears in the correlated regime. The avalanche sizes in this regime present high fluctuations. This made their study mainly unaccessible to our simulations. However, the roughening process, the avalanche formation mechanism, the scaling property of the avalanche durations presented above, as well as our direct observations [69] suggest that in the correlated regime the clusters taking part in avalanches have a characteristic length. This length increases linearly with the strength of the interparticle forces.

6.8 Conclusions and discussion

We studied two-dimensional granular piles of magnetized particles in distinct element simulations similar to the experiments of Forsyth et al. [82, 108]. Regarding the magnetization dependence of the angle of repose and surface roughness of the piles, we obtained good agreement with these experiments and also with the slightly different experiments of Peters and Lemaire [177] (see Section 2.5). We found that in the analyzed magnetization range, both the angle of repose and the surface roughness increases linearly⁶ with the strength of the interparticle forces characterized by the dimensionless quantity f , defined by the ratio of the maximum magnetic force at contact and the gravitational force. In the studied regime of cohesiveness, both wet granular materials (Section 2.3) and dry fine powders (Section 2.4) exhibit a similar behavior. The saturation effect reported for wet granular materials [221, 167] could not be reproduced, most probably, because the used magnetizations and hence the interparticle forces were not strong enough.

Our results are particularly interesting regarding the fact that we used an interaction cutoff in calculating the magnetic dipole-dipole interactions. The good agreement with the experimental results [82, 108, 177] demonstrates that the cutoff, which was chosen based on the arguments presented in Chapter 5, leads to an acceptable level of physical correctness in distinct element simulations and suggests that the cohesive behavior of magnetic granular systems is mainly independent of the fact that the magnetic interactions are of infinite range. However, we cannot exclude the possibility that long range correlations induced by infinite range interactions have higher order effects, even though these could not be captured so far neither in experiments [82, 108, 177] nor in simulations.

The anisotropy of the magnetic interactions seems to be the main source of differences between magnetic and other types of cohesive systems. As it was already noticed by Forsyth et al. [82, 108], f overestimates the effective cohesion. Currently it is not clear whether an appropriate dimensionless quantity describing accurately the level of cohesion in a magnetic granular system exists. As a matter of fact, the angle of repose in our simulations increased much more slowly with f than expected from a stability criteria [7] and experiments on wet granular materials [221]. However, our two-dimensional simulations and the experimental results of Forsyth et al. are in good accordance, though the angle of repose at zero magnetization in our case was smaller. This difference could be reduced by considering the effects of the front and back walls of the quasi-two-dimensional experimental setup used by Forsyth et al. [82, 108]. We found that the side wall effects also introduce a stronger dependence of the angle of repose on f . Taking into consideration the static and rolling friction of the particles could probably reproduce even more closely the experimental results.

Regarding avalanche formation as particles were added on the top of the piles, at small magnetizations we found that the avalanches are composed of small vertical chains following each other at short times, while, for magnetizations larger than a critical value, typical avalanches consisted of one large particle cluster. Based on a plausible stability criteria we gave an estimate for the transition point, which was justified by simulations. Based on avalanche characteristics, we could identify two regimes depending on magnetization: a *granular* and a *correlated regime*.

In the granular regime the average avalanche durations are found to be proportional to the avalanche sizes. The ratio of the avalanche sizes to the corresponding average durations,

⁶This corresponds to a quadratic dependence on magnetization.

which can be interpreted also as an average avalanche flow, has a linear dependence on f . Analyzing the avalanche size distribution, we could identify a characteristic avalanche size (measured in number of particles). Based on the observed scaling of the avalanche size distributions with f , we argue that the characteristic avalanche size increases linearly with the strength of the interparticle forces. This is in qualitative agreement with the experiments of Szalmás et al. [217].

In the correlated regime the average avalanche durations are proportional to the square root of avalanche sizes with no further dependence on f . This is explained by the free fall of long particle clusters. The scaling property of the avalanche duration statistics demonstrates a characteristic avalanche duration proportional to \sqrt{f} . Based on our observations, the characteristic size of the avalanches found in the granular regime, quantified with the number of participating particles, is suppressed by large fluctuations at the transition to the correlated regime. Instead, the avalanches in the correlated regime have a characteristic cluster length which increases linearly with f .

In a paper presenting flow properties of magnetized particles, Forsyth et al. [80], have also reported evidence for a critical magnetization at which the system undergoes a transition from free-flowing to stick-slip behavior. This could correspond to the transition from the granular regime to the correlated regime identified in our simulations. These regimes are similar to the moisture-induced regimes affecting the avalanches of wet granular materials found by Tegzes et al. [221, 223].

However, due to the anisotropy of the magnetic interactions, differences in the characteristics of avalanches and avalanche formation mechanisms exist. The long range nature – even if it is practically limited to a few particle diameters – can affect the order inside the avalanches. Furthermore, at very large liquid content, Tegzes et al. [223] could also identify a *plastic regime* in which the grains flow coherently. It is not clear whether such a regime exists for magnetic systems.

In our simulations, we used both gently positioned and dropped particles. As a sign of robustness, the results were mainly unaffected by the small impact energies introduced in the latter case by each particle “fired into the pile”. We have also introduced a *side wall model* simulating the effect of the front and back walls of a quasi-two-dimensional Hele-Shaw cell arrangement. With the used parameters this gave no qualitative difference in avalanche statistics, but influenced the dependence of the angle of repose on f similarly to experimentally observed effects [82, 108].

As a final remark, let us note that the results on avalanche sizes and durations may slightly depend on the chosen time scale on which the avalanches are observed. However, we argue that a much coarser or finer time scale would both lead to nonphysical results, while a small correction would not lead to a qualitative difference.

Part III

Shear bands

Chapter 7

Morphologies of three-dimensional shear bands

The rheological properties of granular media is a key question which controls the ability of handling these materials. A central effect related to this is the tendency of granular systems undergoing slow deformations to localize the strain to narrow domains called *shear bands*. The morphology of these failure zones is far from being understood. Different two-dimensional and boundary induced shear bands have a vast literature including both numerical and experimental studies (see Section 3.1). The three-dimensional case is, however, in both computational and experimental point of view much more difficult. In simulations, the number and the shape of the particles is limited because of large computational needs, while the experiments have a major drawback in the difficulty of getting information from inside the sample. Strain localization in three-dimensional samples gained more attention when experimental tools such as Computer Tomography (CT) became available. Axisymmetric triaxial shear tests (see Section 3.4), used mainly to obtain mechanical properties of soils, revealed complex localization patterns and shear band morphologies depending on test conditions [51, 50, 8, 17].

In this Chapter, we are going to discuss shear band morphologies obtained with three-dimensional distinct element simulations. We report results on two simulation setups: One which exhibits a spontaneous symmetry breaking strain localization and one which keeps the original symmetry of the system. We discuss the formation mechanism of the shear bands in the light of our observations and compare the results with known experiments. We identify the shear bands by calculating a local shear intensity. We show that this is correlated with the angular velocity of the grains and also with the local void ratio and the coordination number, which give alternative ways to detect the shear bands as well as further information on the strain localization.

7.1 Simulations

With a standard Distinct Element Method¹ (DEM) [44] using the Hertz contact model [133] and appropriate damping [129, 30] combined with a frictional spring-dashpot model [145, 181], axisymmetric triaxial shear tests were performed on vertical cylindrical samples of diameter $D = 22$ mm and height $H = 46$ mm (see Fig. 7.1 (a)). The slenderness

¹For an overview see Chapter 4.

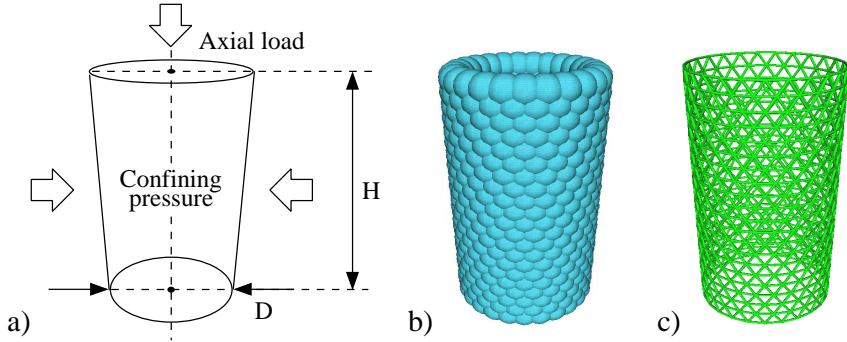


Figure 7.1: a) A granular sample is subjected to a vertical load and a lateral confining pressure. b) The rubber membrane surrounding the sample is simulated by overlapping spheres initially arranged in a triangular lattice. c) The neighboring spheres are interconnected with linear springs. The confining pressure acts on the formed triangular facets.

of the samples was $H/D \approx 2.1$ similarly to most experiments.² Each sample consisted of 27000 spherical particles with the same mass density $\varrho = 7.5 \cdot 10^3 \text{ kg/m}^3$. To avoid symmetries of monodispersed systems, the particle sizes were set randomly according to a narrow Gaussian distribution. The mean particle diameter was $d = 0.9 \text{ mm}$ and the standard deviation was 2.77%. This particle size distribution imitates distributions encountered in experiments using idealized granular materials (e.g. steel beads).

For simplicity we made no difference between particle-particle and particle-wall contacts. The normal F_n and tangential \mathbf{F}_t component of contact forces were calculated as

$$F_n = -\kappa_n u_n^{3/2} - \gamma_n u_n^{1/2} v_n, \quad (7.1)$$

$$\mathbf{F}_t = -\kappa_t \mathbf{u}_t - \gamma_t \mathbf{v}_t, \quad (7.2)$$

where $\kappa_n = 10^6 \text{ N/m}^{3/2}$, $\kappa_t = 10^4 \text{ N/m}$, $\gamma_n = 1 \text{ N s/m}^{3/2}$, and $\gamma_t = 1 \text{ N s/m}$ are the normal and tangential stiffness and damping coefficients, u_n and \mathbf{u}_t are the normal and tangential displacements, and v_n and \mathbf{v}_t are the relative velocities.

The normal displacement, the normal velocity, and the normal force are scalars measured along the normal vector of the contact plane, while the tangential displacement, the tangential velocity and the tangential force are two-dimensional vectors embedded in the contact plane. The normal displacement was calculated from the relative position, the size, and the shape of the bodies in contact. The tangential displacement was calculated by integrating the tangential velocity in the contact plane during the lifetime of the contact. The tangential force models the friction force limited by the Coulomb law to μF_n , where μ is the coefficient of friction. We used $\mu = 0.5$. To allow for sliding contacts, we limited the length of the tangential displacement to $\mu F_n / \kappa_t$.

The simulations were run at zero gravity. The motion of the bodies was calculated by solving numerically the Newton equations. The translational motion was solved with Verlet's Leap-Frog method. The rotational degree of freedom was integrated in quaternion representation with Euler's method. With the above stiffness and damping coefficients, the inverse of the average eigenfrequency of the contacts, in both normal and tangential direction, was more than one order of magnitude larger than the used integration time

²We used conditions as realistic as possible in order to allow for direct comparison with experiments.

step $\Delta t = 10^{-6}$ s. This assured that the noise level induced by numerical errors and grain elasticity was low.

We prepared homogeneous initial configurations with a deposition method.³ The grains were first placed in a tall solid cylinder of width D delimited by two horizontal platens at $h = 3H$ distance from each other. The maximum allowed initial grain overlap was 1%. Each grain and the upper platen were given a downward velocity $v = v_0 z/h$, where $v_0 = 80 \cdot 10^{-2}$ m/s and z is the vertical distance measured from the fixed bottom platen. These velocities led to an almost simultaneous first contact of the bodies. The system was stabilized with a force ($F_0 = 200 \cdot 10^{-3}$ N) applied on the upper platen. This was switched on when the inner pressure of the sample could compensate it. At the end of the preparation phase, we waited until the system relaxed and the kinetic energy of the bodies became sufficiently small in order not to disturb the upcoming tests. The friction of the particles was switched off during this preparation phase in order to allow for generation of dense samples. The volume fraction at the end of the preparation phase was $\eta_0 = 0.643$. This is close to the random close packing value [12, 254], however, it is slightly larger, as expected for a system with small size distribution.

The solid cylinder used in preparation was replaced by an *elastic membrane* in the tests (see Fig. 7.1 (b, c)). The elastic membrane was modeled with 14904 overlapping spheres having equal diameter $d_m = 1$ mm and equal mass density $\varrho_m = 100$ kg/m³, and initially forming a triangular lattice on the external surface of the cylinder. The upper and lower row of the “membrane nodes” was stucked to the upper and lower platen. The “membrane nodes” interacted with the grains according to the already presented contact model and their motion was computed the same way as for the grains, however, they could not rotate and they had no repulsive contacts with each other, instead they were connected with linear springs. The attractive force F_s acting between two nodes was

$$F_s = -\kappa_s u_s - \gamma_s v_s, \quad (7.3)$$

where $\kappa_s = 0.5$ N/m and $\gamma_s = 10^{-3}$ N s/m are stiffness and damping coefficients, u_s is the spring’s elongation, and v_s is the relative velocity of the nodes. At any time the spring’s elongation was equal to the relative distance of the nodes, initially 0.5 mm.

The stiffness of the springs was chosen such that the particles could not escape by passing through the membrane. In addition a homogeneous confining pressure $\sigma_c = 500$ N/m² was applied on the membrane. This was simulated by considering the triangular facets formed by connected membrane nodes. We assumed that these triangular facets are made of a solid material. From their area and the value of the confining pressure, the forces acting on them were calculated. These force were then transferred to the corresponding “membrane nodes” which are in contact with the grains. The effective external pressure was larger than σ_c , because the springs had their own contribution too, however, this contribution was small compared to σ_c .

In similar simulations, Sakaguchi and Mühlhaus [197] used a membrane model similar to ours but without an explicit confining pressure, relying only on the stiffness of the springs. The problem of this approach, which we have also tested, is that it works only for large σ_c . In a slightly different approach, Tsunekawa and Iwashita [232] applied a confining pressure directly on the external particles. This requires the computationally expensive identification of the external particles and a Delaunay triangulation computed

³For other methods see [210, 143, 144].

	Compression	Tilting
A	Base velocity	Enabled
B	Base velocity	Disabled
C	Two times faster	Enabled
D	Two times faster	Disabled

Table 7.1: Simulation runs. The upper platen is moved downward either with a base velocity or two times faster, while its tilting is either enabled or disabled.

for them. A similar model was also used by Cui and O’Sullivan [43], who in addition used special periodic boundary conditions in order to speed up the calculations by computing only a section of the cylindrical sample. This allows for larger samples but requires that the symmetry of the system is kept during compression.

In order to achieve different shear band morphologies, we have executed several simulation runs, using slightly different boundary conditions. The upper platen (having mass $M = 10^{-2}$ kg) could not tilt in the preparation phase, but in certain tests it could freely tilt along any horizontal axis with moment of inertia $I = 10^{-7}$ kg m². The bottom platen was fixed during both preparation and test phase. During the tests, the samples were compressed by moving the upper platen in vertical direction downwards with a constant velocity (i.e. in a strain controlled way). Starting from the same initial condition, four different runs – denoted by (A), (B), (C), and (D) – were executed (see Tab. 7.1). Two different compression velocities were used: $u_1 = 10$ mm/s in tests (A) and (B) and $u_2 = 2u_1$ in tests (C) and (D). Tilting of the upper platen was enabled in tests (A) and (C) and disabled in tests (B) and (D).

7.2 Local shear intensity

For shear band identification, we calculated the local shear intensity S generalized from a two-dimensional definition given by Daudon et al. [46]. First, the regular triangulation [59] of the particle system was calculated [36]. The displacements of the particles (relative to a previous state) are known from the DEM simulation. We extended the displacement field to the whole volume of the sample with a linear interpolation over each tetrahedron of the triangulation. For each particle we identified the incident triangulation cells (tetrahedra) and the surrounding polyhedron formed by the center points of the neighboring particles. The particles at the sample’s boundary, having infinite incident cells, were skipped, i.e. no local shear intensity was defined for them.

We calculated the *local deformation gradient tensor* defined by the space derivatives $\partial_i u_j$ of the displacement vector \mathbf{u} . In a neighborhood Ω of volume V , the components of this tensor are calculated as

$$\langle u_{ij} \rangle = \frac{1}{V} \int_{\Omega} \partial_i u_j dV. \quad (7.4)$$

Using the Gauss-Ostrogradski theorem the volume integral can be transformed into a closed surface integral over the boundary $\partial\Omega$ of Ω , leading to

$$\langle u_{ij} \rangle = \frac{1}{V} \oint_{\partial\Omega} n_i u_j dS, \quad (7.5)$$

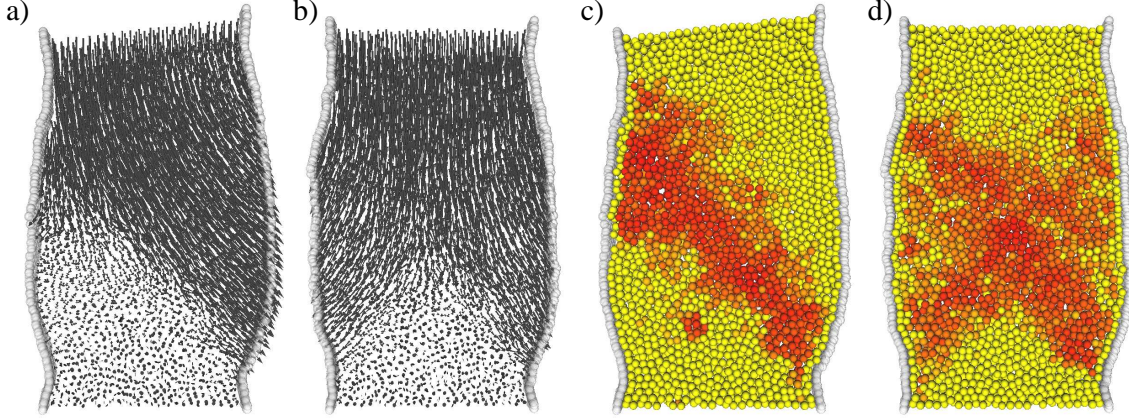


Figure 7.2: Vertical cross sections taken at the middle of samples (C) and (D) at 10% axial strain. The panels (a) and (c) show sample (C). The panels (b) and (d) show sample (D). Panels (a) and (b) outline the grain displacements. The red color on panels (c) and (d) encodes the local shear intensity.

where \mathbf{n} is the exterior normal along the boundary. Applying the above formula to discrete particle neighborhoods and to the linear interpolation of the particle displacements, the integral can be reduced to a summation over triangular facets.

The symmetric part of the local deformation gradient tensor is a *macroscopic strain tensor*.⁴ Using the eigenvalues ε_i of this tensor, we defined the dilation rate of the particle neighborhoods

$$K = \frac{1}{3} \sum_{i=1}^3 \varepsilon_i \quad (7.6)$$

and the local shear intensity

$$S = \max_{i=1..3} |\varepsilon_i - K|. \quad (7.7)$$

Notice that the K and S are derived exclusively from particle rearrangements. In their definition, we disregarded elastic deformation and rotation of the grains since we are mainly interested in identification of the shear bands, which are strongly linked to geometric effects. For constitutive models (which we do not discuss here), a more complete treatment of the strain, and consequently a more precise definition of the shear intensity would be needed (see for example [172]).

7.3 Shear band morphologies

Taking cross sections of the sheared samples and coloring the grains according to the local shear intensity S , we could identify shear bands (see Fig. 7.2 and Fig. 7.3). In accordance with the experiments of Desrues et al. [50], we found that internal instabilities develop into a localized deformation along a narrow failure plane of width of about 10 particle diameters when tilting of the upper platen is enabled (see panels (a) and (c) of Fig. 7.2). This means that the absence of enforced axisymmetry leads to spontaneous

⁴The anti-symmetric part encodes the angular velocity of macroscopic rotations.

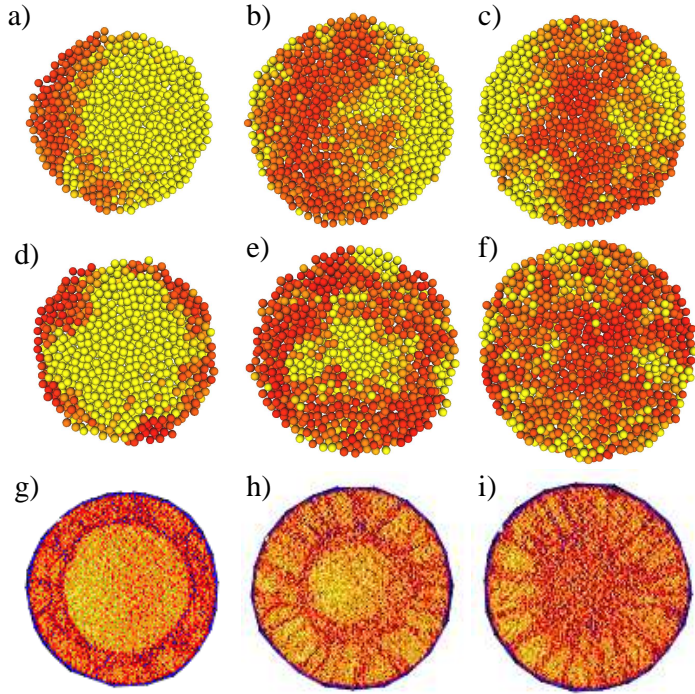


Figure 7.3: Horizontal cross sections. The panels (a), (b), and (c) show sample (C). The panels (d), (e), and (f) show sample (D). The cross sections were taken at 10% axial strain. Panels (g), (h), and (i) present CT scans (F2075) [17]. The cross sections were taken at different heights: Close to the top (a, d, g), at the middle (c, f, i), and in between (b, e, h). The red color encodes the local shear intensity on the panels (a-f) and the local void ratio on the CT scans (g-i).

symmetry breaking strain localization.⁵ At the same time, in full accordance with [50, 17], nontilting platens act as a stabilizing factor and lead to an axisymmetric hourglass shaped shear band with two conical surfaces and complex localization patterns around them (see panels (b) and (d) of Fig. 7.2).

The horizontal cross sections (d, e, f) presented on Fig. 7.2 can be compared to the experimental results of Batiste et al. [17]. The panels (g), (h), and (i) of Fig. 7.3 show CT scans from one of their axisymmetric triaxial shear tests executed in microgravity aboard a NASA Space Shuttle. In the presented case, they have applied a confining pressure of 0.52 kPa [17]. Good agreement of shear band shapes, including their nontrivial structure, can be recognized in spite of the rather limited number of grains in our simulations. It is worth also mentioning that in the tilting case, as it can be noticed on the horizontal cross section taken close to the top platen (shown on Fig. 7.3 (a)), the shear bands are not totally plane but at extremities they follow the curvature of the boundary. The same was observed experimentally by Desrues et al. [50].

In simulations, Tsunekawa and Iwashita [232] found localization patterns for the nontilting case similar to the one reported above, however, they have not investigated the case of tilting platens. Cui and O’Sullivan [43] focused mainly on validating their simulation

⁵We discuss some further aspects, including the friction and density dependence of this spontaneous strain localization, in Section 8.2 of the next Chapter.

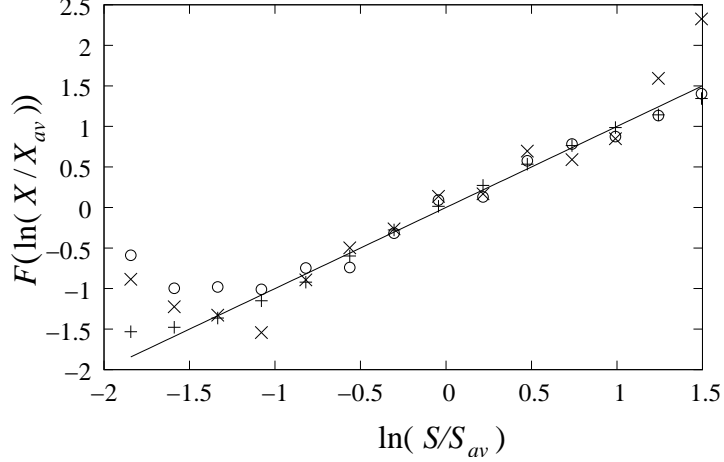


Figure 7.4: Correlation of the local shear intensity S with the local void ratio (ν , \circ), the coordination number (Z , \times), and the angular velocity of the grains (R , $+$). F denotes a linear transformation different for each data set. X is one of ν , Z , and R . All quantities are scaled by average values (X_{av} , S_{av}). The data is collected from four samples at 10% axial strain. See text for more details.

technique and have not presented results on strain localization. Their simulations were not suitable for studying the tilting case. Sakaguchi and Mühlhaus [197] investigated the stress-strain relation in nontilting case at very large confining pressures, which did not lead to strain localization.

7.4 Alternative ways of shear band identification

The shear bands observed on the vertical cross sections presented on panels (c) and (d) of Fig. 7.2 are in good agreement with changes in the velocity field shown on the panels (a) and (b). This already gives a justification of the used shear band identification method based on local shear intensity. In this Section, we present further justification through alternative ways of shear band identification which we have investigated in order to test our method and also to reveal the behavior of other local quantities. For this, we have checked the correlation of local shear intensity S with the local void ratio ν , the coordination number Z , and the angular velocity R .

It is widely known that frictional dense granular materials dilate during shear. In some experiments (e.g. experiments based on CT [51, 50, 8, 17]) the local void ratio is used to identify the shear bands. We measured the void ratio using the regular triangulation [59, 36] of the spherical particles. The volume of the regular Voronoi cells V_c and the volume of the grains V_g define the local void ratio $\nu = (V_c - V_g)/V_g$.

In numerical simulations using spheres of equal or nearly equal size, a good alternative to the local void ratio ν is the coordination number Z defined by the number of contacts, which decreases as ν increases. Its main advantage is that it can be defined exactly and calculated fast, however, if the size distribution is wide also a nontrivial particle size scaling has to be taken into account.

The existence of particle rotations in shear bands of frictional granular systems is

known to experimentalists for a long time (see e.g. [168]). It was evidenced in simulations by several groups (see e.g. Herrmann et al. [101]). In our simulations, we have also measured for each grain the absolute value of the angular velocity R . In general, this was found to be large in the shear bands and small outside of them.

All the quantities mentioned above, i.e. the local void ratio ν , the coordination number Z , the angular velocity R , and the local shear intensity S are defined for each particle. We checked their correlation with a histogram technique using the values calculated for different particles as different statistical samples. The ν , Z , and R values were averaged for each logarithmic histogram bin of S . We have also calculated the total averages ν_{av} , Z_{av} , R_{av} , and S_{av} . On the quantities $\xi = \ln(X/X_{av})$, where X is one of ν , Z , and R , we applied different linear transformations $F(\xi) = \alpha(\xi - \xi_0)$ (shift and scaling) to achieve data collapse of $F(\ln(X/X_{av}))$ as function of $\ln(S/S_{av})$ (see Fig. 7.4).

The appropriate scaling term α of the linear transformation F shows the sensitivity of the R , Z , and ν quantities with respect to the local shear intensity S . We found $\alpha = 1$ for the angular velocity, $\alpha = -9$ for the coordination number (decreasing as S increases), and $\alpha = 27$ for the local void ratio. The fluctuations of R , Z , and ν relative to S proved to be proportional to $\sqrt{|\alpha|}$. Regarding shear band identification, this means that the angular velocity R is essentially equivalent with the local shear intensity S . However, the coordination number Z and the local void ratio ν are less sensitive and they exhibit large fluctuations due to random packing and rearrangements, therefore, they need more spatial and/or temporal averaging to achieve the same accuracy.

7.5 Stress-strain relation

In order to compare to most common experimental results, we have measured the axial stress σ on the upper platen and calculated the stress ratio σ/σ_0 , where σ_0 denotes the initial stress. We found that with increasing axial strain the stress ratio (i.e. the response of the sample) increases until it reaches a peak value, then it decreases (see Fig. 7.5). This decrease of axial stress – usually called *strain softening* – is well known from triaxial shear tests of dense granular specimens (see for example [130]).

Strain softening is explained by the fact that local deformation due to shear is accompanied by dilatation resulting in decrease of the force bearing capacity of the material. This further intensifies the deformation and leads to failure and shear bands. In good agreement with the experimental results, we observed shear bands around 10% axial strain.

Up to about 15% axial strain, indifferent of strain rate and tilting of the upper platen, there is no significant difference in stress-strain relation measured in different simulation runs. Dependence on different material parameters and confining pressures was not tested, however, based on experimental results [51, 50, 8, 17], we do not expect strong dependence on these parameters. After about 15% axial strain the different boundary conditions and shear band shapes result in different stress-strain curves (see Fig. 7.5).

In the tilting case, the upper part of the sample moves as a single block. The formed planar shear band allows for a stable slipping mode with nearly constant stress until boundary effects come into play (see curves (a) and (c) on Fig. 7.5). In the nontilting case, the geometry and the hourglass-shaped shear band forces the particles to enter and to leave the failure zone. In this case, a stable slipping mode cannot be formed. As the test sample is further compressed it opposes more and more firmly to compression (see

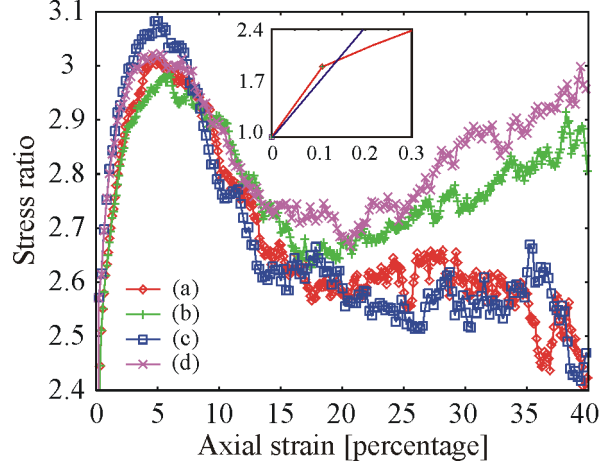


Figure 7.5: Stress-strain relation. The stress ratio σ/σ_0 , where σ_0 denotes the initial stress measured on the upper platen is shown as function of the axial strain, for different simulation runs. See inset for low strains. For the lower two curves (a, c) tilting of the upper platen was enabled, and for the upper two (b, d) it was disabled. In case of curves (c, d) the samples were compressed two times faster than in case of curves (a, b).

curves (b) and (d) on Fig. 7.5). This *strain hardening*, manifesting itself in increasing axial stress, appears mainly due to geometric constraints appearing at large axial strains.

7.6 Conclusions and discussion

We have presented simulations of axisymmetric triaxial shear tests based on a standard distinct element method. Two different shear band morphologies known from experiments were presented. Studying such localization patterns with simulations proves to be important because of several reasons: On one hand it helps the understanding of the strain localization process and on the other hand the simulations make possible studies which are difficult to control in experiments (e.g. density and friction dependence of the localization⁶). We have shown that in axisymmetric triaxial shear tests, symmetry breaking strain localization can develop spontaneously if the axial symmetry is not enforced by nontilting platens. To our knowledge it is the first time that this was demonstrated in distinct element simulations. If tilting of the upper platen was not enabled, we could not find symmetry breaking strain localization.

We generalized the shear intensity definition of Daudon et al. [46] to three-dimensions and used it to identify shear bands. In order to check our method and to be able to compare to well-known experimental and numerical results, we have also tested alternative methods of shear band identification. We found strong correlation of the local shear intensity with the angular velocity of the grains, the coordination number, and the local void ratio. This result justifies our method and proves that the shear bands of dense frictional granular systems are characterized by dilation and rotation of the grains.⁷ Regarding shear band

⁶See next Chapter.

⁷This is true only for dense frictional samples! It is known that loose samples densify and when there is no friction the grains do not rotate while the shear intensity can be still significant.

identification, the coordination number and the local void ratio are found to be less sensitive than the local shear intensity and the angular velocity of the grains.

We have also measured the stress-strain relation of the compressed samples. Strain softening was identified in good agreement with experimental results.⁸ We have also found a strain hardening effect at large strains in the nontilting case and explained it in terms of geometric constraints, strain localization, and shear band morphology. This result might depend on the tested material parameters and confining pressure, however, we expect that this dependence is not strong as it is mainly determined by geometric constraints. We have no knowledge of experiments focusing on this particular question, however, some results indicate the validity of our findings (see e.g. the upper panel of Fig. 10 in [130]).

The simulations were run at zero gravity and low confining pressure. We could successfully compare our results with the experimental results of Batiste et al. [17] and Desrues et al. [50]. The experiments of Batiste et al. [17] were executed in microgravity with a similar confining pressure to ours, while Desrues et al. [50] presented experiments at normal gravity and larger confining pressures. Based on the nice agreement with both experiments, we believe that the results presented in this Chapter are not unique to zero gravity and low confining pressures.

In the simulations presented here, we have ignored the rolling resistance of the grains (see e.g. [117]). Our results demonstrate that this is not crucial for the qualitative description of triaxial shear tests. In general, the agreement of our numerical results with experimental results is very good, even though our study is restricted to idealized granular materials composed of spherical grains and the system size (i.e. the number of particles) was much smaller than in usual experiments.

⁸For friction and density dependence, see Section 8.5 of the next Chapter.

Chapter 8

Critical packing density in granular shear bands

Packing density plays an important role in the dynamics of granular materials. Under slow deformation, dense granular samples dilate [189], loose samples densify [261, 227], while the strain is usually localized to shear bands. It is assumed that inside the shear bands the system self-organizes its density to a critical value¹ independent of the initial packing conditions. Even though it forms the basis of many continuum constitutive models of Soil Mechanics [205], this hypothesis formulated a long time ago [32], was not yet proved on a satisfactory level and the underlying mechanisms leading to criticality are not fully understood. A general micromechanical theory of strain localization and shear bands is currently missing. The aim of this Chapter is to study the emergence of critical packing density in sheared granular media and to discuss its relation to strain localization as well as its dependence on the friction between the grains.

The existence of a critical density is suggested by both experiments [51, 50, 8, 17] and computer simulations [266, 178, 195]. In experiments, it is problematic to assure a uniform packing density and it is difficult to control the friction between the grains. Even more, in realistic three-dimensional cases, it is not easy to get information from inside the samples. These factors make it difficult to study experimentally the properties of the shear bands and in general to study the packing and friction dependence of strain localization. Computer simulations do not have such limitations, however, the number and the shape of the particles is limited through large computational needs. Many numerical studies, so far, focused only on special conditions in which shearing extends to the whole volume of the samples [266, 178, 195]. This allowed for discussing the criticality based simply on global behavior (e.g. dilatancy). Such studies neglected the involved localization phenomena inevitable in real situations and disregarded the self-organizing manner in which the packing state of the shear bands is usually formed.

Relying on three-dimensional distinct element simulations of systems composed of spherical grains undergoing axisymmetric triaxial shear tests, in this Chapter, we study the behavior of samples having different initial packing densities and different friction properties. Following the self-organization of a spontaneous strain localization process, we present evidence for the existence of a critical packing density η_c inside shear bands. We demonstrate that the criticality is restricted to the shear bands. The critical state is found to be independent of the initial packing conditions but dependent on the friction acting

¹See a discussion on this criticality in Section 3.3.

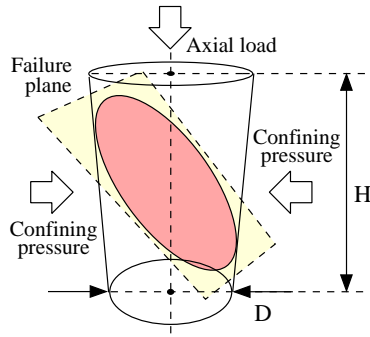


Figure 8.1: Grains placed between two horizontal platens and surrounded by an elastic membrane were subjected to a vertical load and a lateral confining pressure. The upper platen could tilt. A planar shear band was formed which allowed for a stable slipping of the upper part of the sample. (See also Sections 7.1 and 7.3).

between the grains.

We show that the coefficient of friction (μ) is a principal parameter which controls the critical packing state arising in fully developed shear bands as a result of the local dynamic equilibrium between dilation and compaction. A frictionless system can be sheared at a large packing density very close to the random close packing (RCP) limit, because the grains can easily rearrange in compact configurations. This is not possible at large μ , where the rearrangement of the grains is hindered by friction. Consequently, in frictional systems, the shear bands approach a low density state, namely a *dynamic random loose packing* (DRLP) state. We define the DRLP state, estimate its particle density based on the found dependence of η_c on μ , and show that it has to be distinguished from the (static) random loose packing (RLP) limit.²

At the end of this Chapter, we discuss global effects such as the volume change of the samples and the evolution of the axial stress as well as their density and friction dependence. We demonstrate that dense samples dilate while loose samples densify during compression and we show that strain softening, along with shear band formation, appears and amplifies with increasing initial density and friction between the grains.

8.1 Simulations

Our simulations of axisymmetric triaxial shear tests are based on a standard three-dimensional Distinct Element Method³ (DEM) and spherical grains. The used simulation setup (see Fig. 8.1) is similar to the one presented in detail in Chapter 7. We recall that an axisymmetric triaxial shear test consists of slow compression of a cylindrical sample enclosed between two end platens and surrounded by an elastic membrane on which an external confining pressure is applied. In what follows, we summarize the simulation setup, highlighting the differences relative to Chapter 7. If not otherwise stated, the used algorithms and parameter values are the same as those already presented there.

With the deposition method described in Section 7.1, using different coefficients of

²For a description of the RLP and RCP states see Section 3.2.

³For an overview see Chapter 4.

μ_0	0.8	0.5	0.3	0.2	0.1	0.0
η_0	0.555	0.562	0.578	0.599	0.621	0.641

Table 8.1: Volume fraction η_0 of samples prepared with different coefficients of friction μ_0 . With each μ_0 we prepared 2 samples having the same η_0 within 0.2% relative error.

friction μ_0 , we prepared homogeneous initial configurations of different volume fractions.⁴ The volume fraction of the samples η_0 (summarized in Tab. 8.1) could be controlled by μ_0 in the full range of packing densities from random loose packing (RLP) to random close packing (RCP).

The spherical particles had equal mass density and identical elastic and frictional properties. The particle diameters were set according to a narrow Gaussian distribution having mean $d = 0.9$ mm and standard deviation 2.77%. This served to avoid symmetries of monodispersed systems. The prepared cylindrical samples⁵ had diameter $D = 23.3 d$ and height $H \approx 2.2 D$. The samples consisted approximately of 27000 particles as required by the fixed H/D geometry factor.

After preparation, the friction coefficient of the particles was set to a new value μ independent of μ_0 . Similarly to the simulations presented in Chapter 7, we compressed the samples vertically at zero gravity and 0.5 kPa confining pressure. The bottom platen was fixed. The upper platen moved downward with a constant velocity inducing an axial strain rate of 20 mm/s. During this it could freely tilt along any horizontal axis.

The lateral elastic membrane surrounding the samples was modeled with approximately 15000 overlapping, non-rotating, frictional spheres connected with elastic springs and initially forming a triangular lattice (see Fig. 7.1 (b)). The confining pressure was applied on the triangular facets formed by the neighboring “membrane nodes” as described in Section 7.1. The grain-platen and grain-membrane contacts were calculated similarly to grain-grain contacts including the friction properties.

First, we intended to check whether starting from different packing conditions we end up with the same packing density in the shear bands (i.e. a critical state exists). Therefore, the samples of different initial volume fractions (see Tab. 8.1) were compressed using the same coefficient of friction $\mu = 0.5$. Later, to check the friction dependence of the critical state, we compressed the densest samples ($\eta_0 = 0.641$) with 10 different friction coefficients $\mu \in \{0, 0.1, \dots, 0.9\}$. For each set of parameters, two simulation runs were executed using specimens prepared with different random seeds.

During simulations, we calculated *locally* the shear intensity S and the volume fraction η . The regular triangulation of the spherical grains [59, 36] was used to define these quantities. The local shear intensity S was calculated from the macroscopic strain tensor derived from particle displacements as described in Section 7.2. The local volume fraction $\eta = V_g/V_c$, was given by the ratio of a grain’s volume V_g and the volume V_c of its regular Voronoi cell. This provided a measure of local packing density.⁶ To overcome the local fluctuations due to random packing and rearrangements, we calculated spatial averages up to 3rd order neighbors along the regular triangulation.

⁴In Chapter 7, we studied only dense samples prepared with $\mu_0 = 0$.

⁵These are new samples which are similar but different from those studied in Chapter 7.

⁶Notice that the void ratio ν , which we studied in Section 7.4, satisfies the equation $\nu = 1/\eta - 1$, and thus forms an inverse measure of packing density.

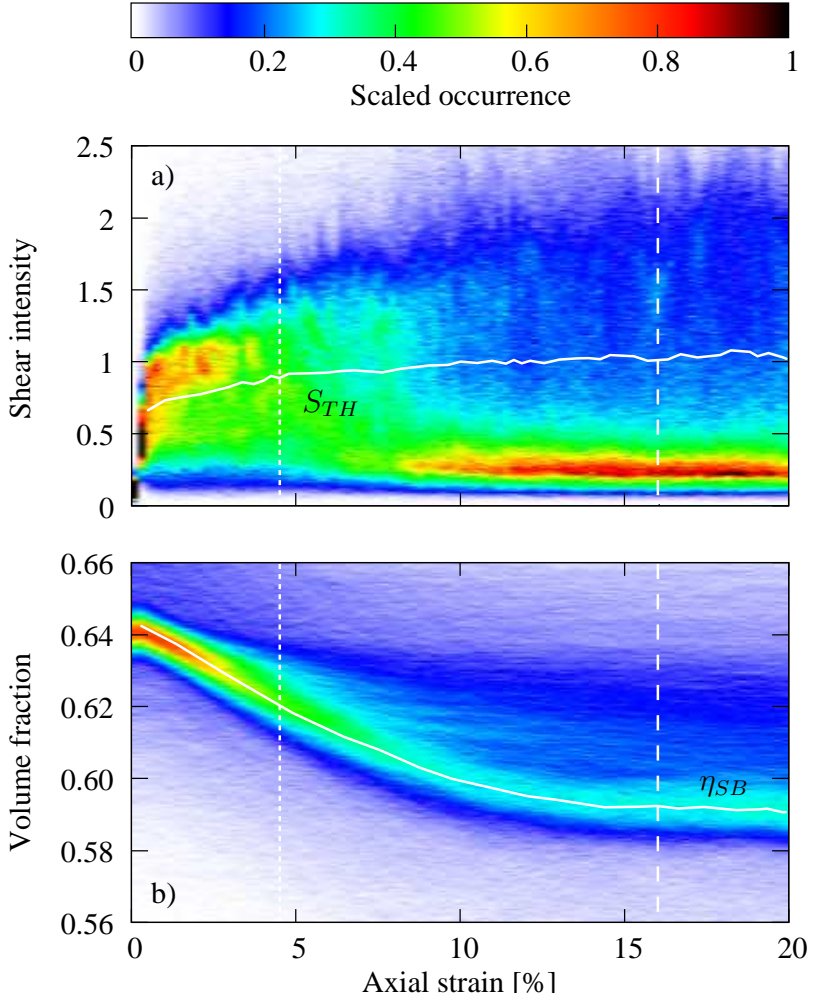


Figure 8.2: Example of shear intensity and volume fraction histogram maps ($\eta_0 = 0.641$, $\mu = 0.5$). The shear intensity is measured in arbitrary units. The scaled occurrences are encoded with the colors shown at the top. On (a) the white curve marks the shear intensity threshold S_{TH} . On (b) it marks the shear band volume fraction η_{SB} . The dotted and dashed vertical lines mark the position of the histograms shown on Fig. 8.3.

8.2 Spontaneous strain localization

Strain localization in dense and loose samples shows substantial differences (see [50] and references therein). In dense samples shear bands are usually formed after a short plastic deformation and inside the shear bands the local packing density is typically lower than in the bulk (i.e. the regions outside of the shear bands). Since denser parts are more stable, the position of the shear bands remains unchanged for the whole duration of the shear tests. Contrary, in loose samples the shear bands have a slightly higher packing density than the bulk and hence the location of the shear bands is likely to change. This leads to more or less homogeneous samples with local packing densities close everywhere to the packing density of the shear bands.

It worth also mentioning that – as it was already discussed in Section 7.4 – in dense frictional systems there is a strong correlation between the local shear intensity and the

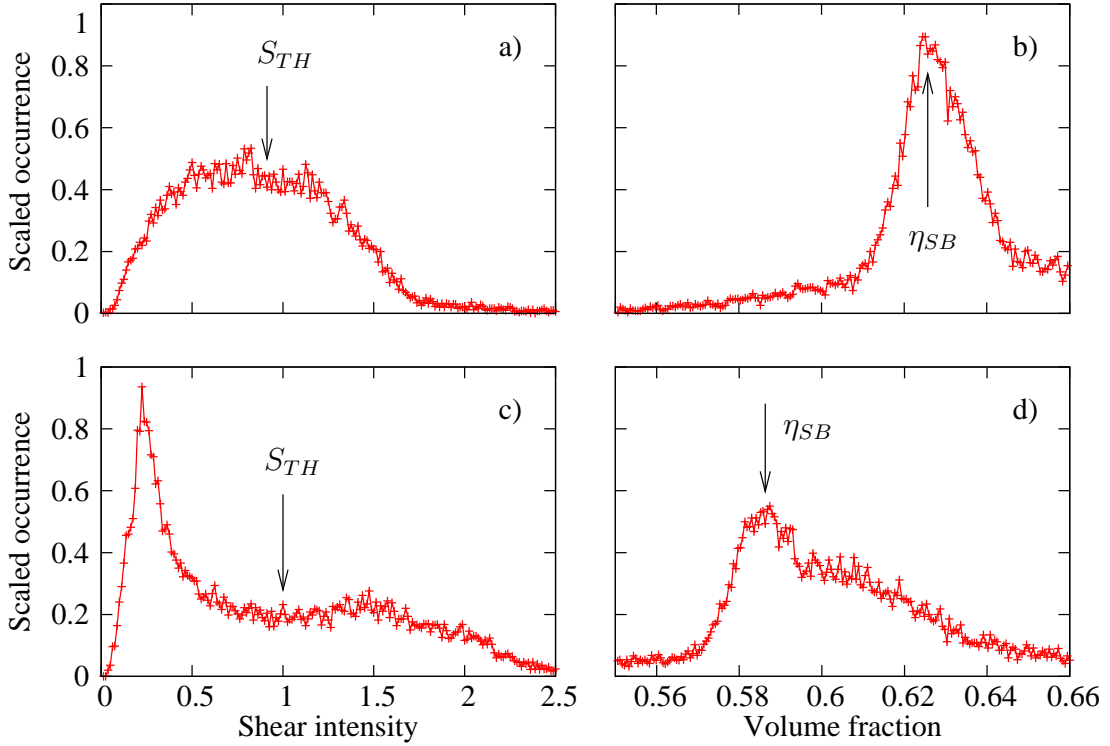


Figure 8.3: Shear intensity and volume fraction histograms. The upper two panels correspond to 4.4% axial strain. The lower two correspond to 16% axial strain. The arrows on (a) and (c) mark the shear intensity threshold S_{TH} (measured in arbitrary units). On (b) and (d) they point to the shear band volume fraction η_{SB} . (See also Fig. 8.2.)

angular velocity of the grains, i.e. the high shear intensity regions and hence the shear bands are characterized by rotating grains. It is clear that this correlation can exist only if the coefficient of friction is large enough. When there is no friction the grains do not rotate while the shear intensity can be still significant. We found that the correlation of shear intensity and grain rotation decays fast for small μ .

In order to understand the main aspects of the spontaneous strain localization process which could be observed in our simulations, let us consider in details the example of a dense sample having $\eta_0 = 0.641$ and $\mu = 0.5$. At the beginning of the compression test, up to approximately 6% axial strain, in shear intensity histograms, we find a peak at high S (see Fig. 8.2 (a) and Fig. 8.3 (a)). This means that almost all particles are involved in rearrangements and the sample experiences a more or less plastic deformation.

Later, at axial strain larger than 6%, a shear band having a width of about 10 particle diameters is formed. In accordance with Chapter 7, this shear band is characterized by much higher S than the bulk and it is localized around a failure plane. In the bulk, composed by the majority of the particles, the shear intensity fluctuations are small, while these fluctuations are large in the shear band. Consequently, in shear intensity histograms (see Fig. 8.3 (c)), we find a strong narrow peak at low S corresponding to the bulk and a small wide peak at high S corresponding to the shear band.

In general, as the samples were compressed, the upper platen gradually tilted, resulting in strain localization and leading to specific packing densities in certain regions of the

samples. The tilting developed spontaneously. We found tilting for both dense and loose samples and at both small and large friction. However, in case of loose samples and samples with small friction the tilting angle was small and regarding its direction the system explored more possibilities. This resulted in more complex failure zones. As the coefficient of friction and the density increased, the tilting direction became more and more stable, which was favorable for a large tilting angle and a well defined shear band.

Therefore, in case of dense specimens and sufficiently large friction coefficients we found a narrow planar shear band as described above. In case of loose specimens or specimens with small friction, the high shear intensity regions occupied large percentage of the samples' volume, had complex shapes, and were not stable. In this latter case, the geometry of high shear intensity regions could not be captured precisely by our simulations because of the limited number of grains allowed by the computational power of the computers available to us at the time of writing.

8.3 Identification of high shear intensity regions

An algorithm which would identify the shear bands geometrically rises several technical problems such as stability and robustness similarly to most geometric algorithms working in three-dimensions. Consequently, the identification of the shear bands – the main goal of our study – could not be based on a geometric method. However, the high shear intensity regions, could be easily found with a histogram technique and the calculation of an appropriate lower limit of S . The high shear intensity regions at large axial strains correspond to failure zones and thus the local properties which emerge in these regions are characteristic to fully developed shear bands.

Motivated by the separation of shear intensity values characteristic to bulk and shear band, which was observed in shear intensity histograms (see Fig. 8.3 (c)), we computed an appropriate shear intensity threshold S_{TH} . This could be used to define two classes of shear intensity values (high and low) and to classify the grains accordingly into shear band and bulk. For this we used Otsu's threshold selection method [173] borrowed from Digital Image Processing. This histogram technique, presented in details in Appendix E, minimizes the within-class variance and maximizes the separation of classes, and thus gives an ideal solution to our problem. We have also tested another threshold selection method modeling the histograms with the sum of two Gaussian functions, however Otsu's method proved to be more stable and more reliable.

The shear intensity threshold S_{TH} , with the condition $S > S_{TH}$, made it possible to identify the grains in high shear intensity regions, which at large axial strains correspond to the shear bands. The average volume fraction η_{SB} around the location of these grains could be calculated. Based on our results, the local volume fraction in shear bands has small fluctuations and gives a peak in the volume fraction histograms (see Fig. 8.2 (b) and Fig. 8.3 (d)). This coincides with η_{SB} calculated with the above procedure, giving a self-validation of the method.

Even though the separation of the shear intensity values shown on Fig. 8.3 (c) does not suggest a *clean* separation of grains into those within and those outside the shear bands, i.e. there isn't a shear intensity gap between the two classes, based on our numerical investigations, this is not crucial for the measured η_{SB} . Adding an artificial random noise of 10% to S_{TH} does influence the resulting η_{SB} only within 0.5%.

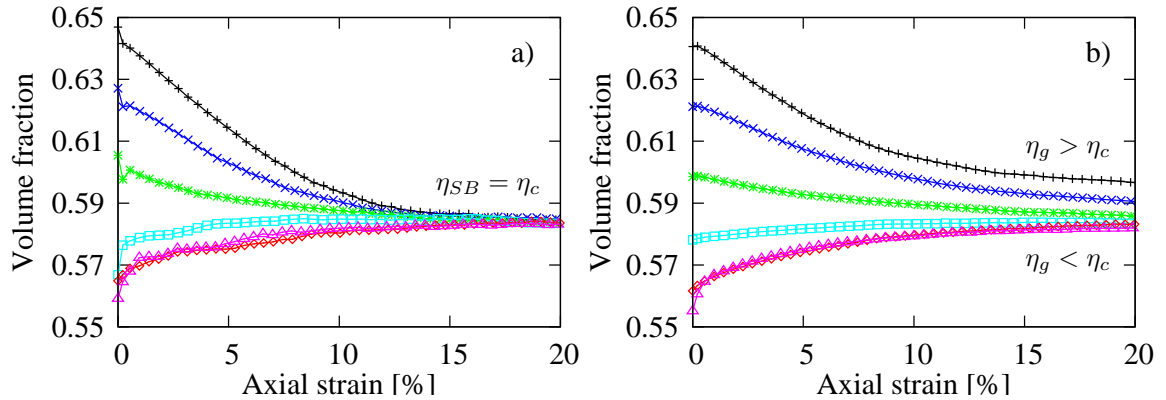


Figure 8.4: Volume fraction of the high shear intensity regions (a) and the global volume fraction (b) as function of the axial strain. The different lines correspond to initial densities (see Tab. 8.1) decreasing from top to bottom. The coefficient of friction was $\mu = 0.5$.

Notice that before strain localization takes place the shear intensity histograms have only one peak (see Fig. 8.3 (a)). In this case, the threshold given by Otsu's method, which falls on the middle of the peak, is not physically relevant. However, as the sample is homogeneous, the selected high shear intensity regions give the volume fraction η_{SB} close to the average volume fraction of the whole sample (see Fig. 8.3 (b)).

8.4 Volume fraction in shear bands

Our simulations of axisymmetric triaxial shear tests, in accordance with experimental results (see for example [50] and references therein), demonstrate that in shear bands granular systems cancel completely the initial packing conditions in a self-organized manner and a critical⁷ volume fraction η_c is reached independent of the initial density η_0 (see Fig. 8.4 (a)). At the same time, the final global volume fraction η_g calculated from the total volume of the samples differs from the packing density of high shear intensity regions and depends on η_0 (see Fig. 8.4 (b)). This latter behavior is expected to become more and more pronounced on larger systems. Therefore, due to strain localization global measurements cannot be used to characterize the properties of shear bands.

As it is well known, dense granular samples dilate [189] and loose samples densify [261, 227] during shear. Our results demonstrate that this effect is concentrated to the shear bands. The packing can be denser or looser outside the high shear intensity regions depending on η_0 (see Fig. 8.4). In dense samples, η_g is larger than η_c , demonstrating that the dilatancy [189] takes place in the shear bands [32], while in loose samples η_g is slightly smaller than η_c , giving a direct proof of shear induced compaction [261, 227].

As an extension to the above results, we checked whether η_c depends on friction. This question was investigated quantitatively for samples having initial density $\eta_0 = 0.641$ (see Fig. 8.5). At $\mu = 0$ the high shear intensity regions have a large volume fraction $\eta_c^0 \equiv \eta_c(0) = 0.637 \pm 0.002$, showing that frictionless granular systems can be sheared at high packing densities very close to the RCP limit. This is simply the consequence of

⁷This criticality should not be confused with the self-organized criticality of nonequilibrium systems. A discussion on this is presented in Section 3.3.

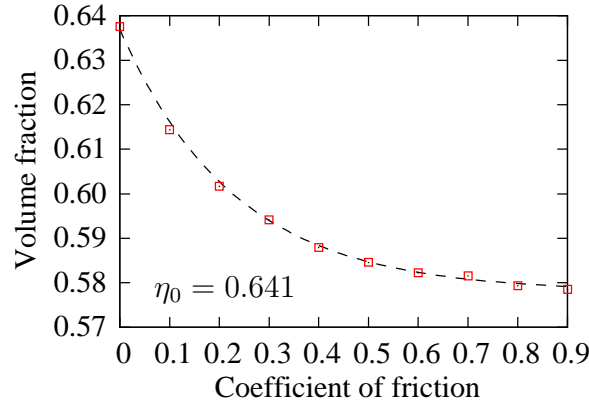


Figure 8.5: Critical packing density of shear bands as function of friction. The points were measured at 20% axial strain. The fitted curve shows $\eta_c(\mu) = \eta_c^\infty - (\eta_c^\infty - \eta_c^0) \exp(-\mu/\mu_c^0)$, where $\eta_c^0 = 0.637$, $\eta_c^\infty = 0.578$, and $\mu_c^0 = 0.23$.

the fact that frictionless grains can easily rearrange during slow shear. At the same time, because particle rearrangements are hindered by friction, the volume fraction of the fully developed shear bands decrease fast with increasing μ .

Using an exponential fit and extrapolating our data to infinitely rough grains (see Fig. 8.5), we estimate that the critical packing density of the shear bands in this limit is $\eta_c^\infty \equiv \lim_{\mu \rightarrow \infty} \eta_c(\mu) = 0.578 \pm 0.003$. The volume fraction η_c^∞ depends only on geometry factors such as shape and size distribution of the grains and is characteristic to the dynamic equilibrium between dilation and compaction developed in a self-organized manner through strain localization. Based on the numerical value of η_c^∞ and this latter aspect, the corresponding asymptotic state, which we call the *dynamic random loose packing* (DRLP) state, can be clearly distinguished from the static RLP limit.

8.5 Global behavior

In accordance with common observations (see for example [50] and references therein), we found that in presence of friction the dense samples dilate during shear, while the loose samples densify (see Fig. 8.6 (a)). In particular we observed that the larger the initial density the larger the dilatancy and the smaller the initial density the larger the compaction. However, we must stress again that the global behavior of a granular system in general gives an incomplete description of the properties of sheared granular media, especially concerning its criticality packing density. Consequently, the transition point from global dilation to compaction can be in this respect misleading.

Regarding the global dilatancy of dense granular samples, we found that for frictionless systems, i.e. for $\mu = 0$, it is insignificant. This is shown by the fact that for the densest samples ($\eta_0 = 0.641$) even the largest volumetric strain was less than 1% (see Fig. 8.6 (b)). However, as expected, for frictional systems this increased substantially with μ , reaching up to 8% at $\mu = 0.9$. As a self validation, we have also calculated the global average of the dilation rate measured locally (defined in Eq. (7.6)). In all cases, this proved to be proportional to the derivative of the global volumetric strain.

The global strain softening of dense frictional samples during triaxial shear tests is

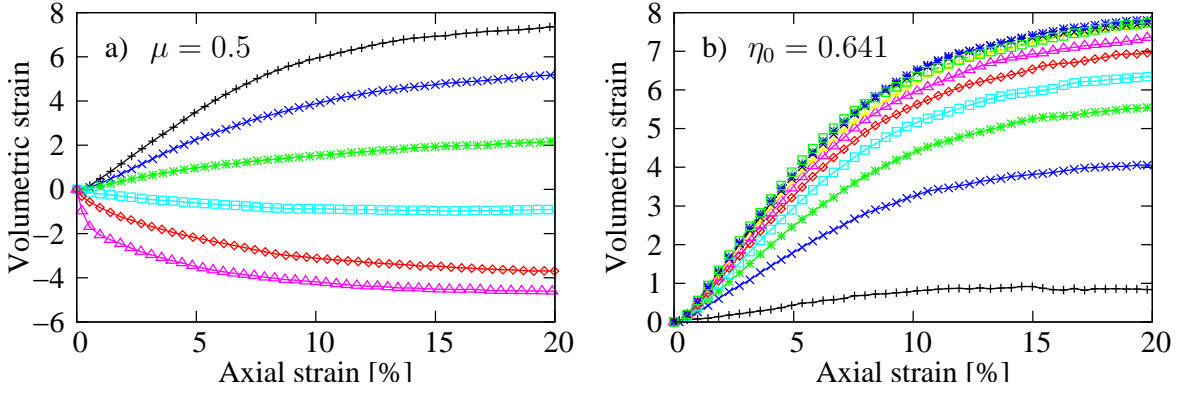


Figure 8.6: Volumetric strain as function of axial strain. The volumetric strain is measured in percentage relative to the initial volume. The different lines correspond to different initial densities (a) (see Tab. 8.1) and to different friction coefficients $\mu \in \{0, 0.1, \dots, 0.9\}$ (b). Both the initial densities and the friction coefficients decrease from top to bottom.

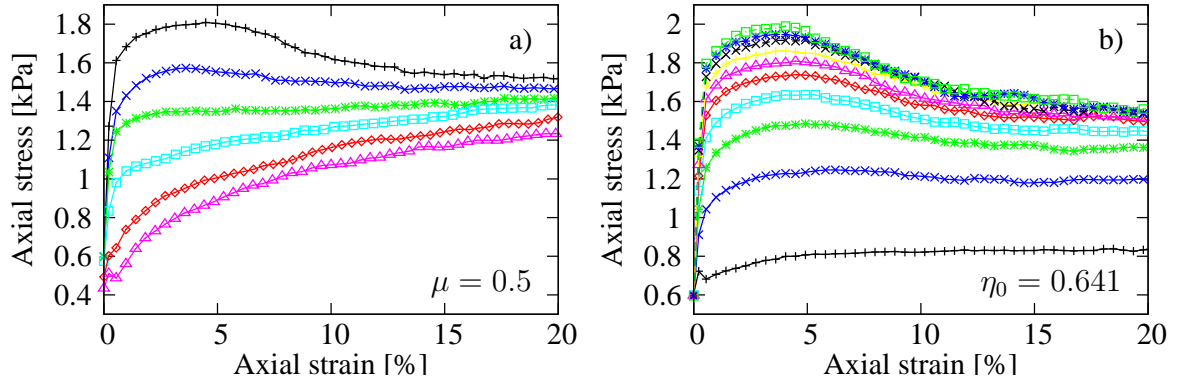


Figure 8.7: Axial stress as function of axial strain. The different lines correspond to different initial densities (a) and to different friction coefficients (b). The figure uses the same notations as Fig. 8.6.

another basic observation [130, 50] which could be reproduced in our simulations (see also Section 7.5). In case of $\mu = 0.5$, the dense samples produced a peak and then a decrease of the axial stress which amplified with increasing initial density. At the same time, the loose samples presented only a monotonously increasing resistance to compression (see Fig. 8.7 (a)). Without friction (i.e. for $\mu = 0$) strain softening was not found even for the densest samples ($\eta_0 = 0.641$). However, strain softening appeared and became more and more pronounced as μ increased (see Fig. 8.7 (b)).⁸

The small peaks, which a careful observer can find at very small axial strains on Fig. 8.7 in case of loose samples (see panel (a)) and in case of small friction coefficients (see panel (b)) are the consequence of the shock waves started in the elastic membrane

⁸We have not studied the transition from monotonously increasing resistance on compression to strain softening. This phenomena [130] should be investigated in relation with local changes in stress transmission properties of granular media and this goes beyond the limits of this work.

at the beginning of the compression, when the downward motion of the upper platen was switched on. Based on our numerical investigations, these shock waves decayed fast and have not influenced the outcome of the tests.

8.6 Conclusions and discussion

We have presented distinct element simulations of axisymmetric triaxial shear tests at zero gravity and low confining pressure. Due to spontaneous strain localization, shear bands were formed. Using a histogram technique (see Appendix E), we identified the grains in high shear intensity regions, which at large axial strains coincide with the shear bands. We measured the packing density η_{SB} in these failure zones and we found that in fully developed shear bands η_{SB} approaches a critical volume fraction η_c independent of the initial density of the sheared samples. This is in agreement with Casagrande's [32] observation made for sandy soils seven decades before and also with recent experiments [51, 50, 8, 17] and numerical studies [266, 178, 195].

We have shown that the criticality is restricted to the shear bands and global measurements (e.g. dilatancy) are unsuitable for investigating the properties of sheared granular media, when strain localization is inevitable. To our knowledge, it is the first time that the critical packing density of shear bands was evidenced based on simulations of a realistic three-dimensional setup and spontaneous strain localization revealing the self-organizing manner in which the packing state of the shear bands is developed.

We have further shown that η_c depends on the coefficient of friction μ and in the limit $\mu \rightarrow \infty$ it converges to a value η_c^∞ , which we have computed within the accuracy of our simulations. The calculated η_c^∞ defines an asymptotic low density *dynamic random loose packing* (DRLP) dependent only on the geometry of the grains. This packing state is distinguishable from the static RLP limit and is characteristic to the dynamic equilibrium between dilation and compaction emerged in shear bands during strain localization.

Our results are derived for idealized granular materials composed of spheres with narrow size distribution. For non-spherical grains and wide size distributions the packing efficiency increases [53], which should be also reflected in the packing density of the shear bands. This explains why experimental results on sand reveal smaller volume fractions in shear bands [50, 17] than the values found in our simulations. For simplicity, we have also ignored the rolling friction (see e.g. [117]) acting between the grains. The results demonstrate that this is not crucial for the criticality of the shear bands, however, the value of η_c^∞ might be influenced by this simplification too.

Regarding the global behavior of the samples, we found that during axisymmetric triaxial shear tests the dense samples dilate while the loose samples densify, which is in full accordance with the experimental results and theoretical expectations [189, 261, 227, 50]. We could also reproduce the strain softening effect known from experiments [130, 50]. We found that strain softening, along with shear band formation, appears and amplifies with increasing initial density and coefficient of friction. As it was discussed in Section 7.5, in dense frictional samples, after strain softening and shear band formation, if tilting of the upper platen is not allowed, i.e. spontaneous symmetry braking is suppressed, strain hardening sets in. Even though we have not tested the friction and density dependence of this effect, we expect it to be mainly independent of these factors, because it is basically a result of geometric constraints appearing at large axial strains.

Summary

New scientific results

- (I) (a) By means of numerical calculations, I have analyzed [68] the effect of an interaction cutoff R in a two-dimensional system of magnetic particles. In such systems, there are two main local dipole arrangements: (1) a ferromagnetic state with dipoles organized in a triangular lattice, and (2) an anti-ferromagnetic state with dipoles organized in a square lattice. I have found [68] that the ferromagnetic state is much more sensitive to the interaction cutoff than the anti-ferromagnetic state.
(b) In the infinite range limit and for large cutoff values the ferromagnetic state slightly dominates over the anti-ferromagnetic state. This is reversed at $R \approx 4$ particle diameters, leading to the complete disappearance of the ferromagnetic state at $R \approx 2$ particle diameters. Bending ferromagnetic and anti-ferromagnetic two-line systems, I have shown [68] that regarding typical local orderings a substantial change occurs between $R \approx 4$ and $R \approx 5$ particle diameters. Based on these results, I have argued [68] that $R \approx 5$ particle diameters is the lowest reasonable choice for a dipole-dipole interaction cutoff usable in computer simulations of two-dimensional dipolar hard sphere systems.
- (II) (a) I have studied [70] two-dimensional granular piles of magnetized particles in distinct element simulations using the interaction cutoff $R = 6.25$ particle diameters, which assured that the local orderings, playing a principle role in the dynamics of granular systems, are realistic. I have found [71] that in the analyzed magnetization range both the angle of repose and the surface roughness of the piles exhibits linear dependence on the interparticle force ratio f , which is defined by the ratio of the maximum magnetic force at contact and the gravitational force. This is in accordance with the quadratic dependence on magnetization known from experiments.
(b) Based on different avalanche formation mechanisms at small and at large interparticle force ratio f , I could identify two regimes [71]: a *granular* and a *correlated regime*. The transition between the two regimes is not sharp. Based on a plausible stability criteria I have derived an estimate for the transition point, which was justified by the simulation results.
(c) In the granular regime, characterized by avalanches composed of small vertical chains following each other at short times, the average avalanche durations are proportional to avalanche sizes (measured in number of grains). Furthermore, the average avalanche flow (i.e. the ratio of avalanche sizes and corresponding average durations) has a linear dependence on f . Analyzing the avalanche size distributions, I have shown [71] that – in accordance with experimental results – there exists a characteristic avalanche size proportional to f .
(d) In the correlated regime the average avalanche durations are proportional to the

square root of avalanche sizes with no further dependence on f . This is explained by the existence of large and long particle clusters characteristic to this regime. I have shown evidence [71] that the characteristic size of the avalanches found in the granular regime is suppressed by large fluctuations at the transition to the correlated regime and the avalanches in the correlated regime have only a characteristic cluster length increasing linearly with f .

- (III) (a) I have carried out [73] three-dimensional distinct element simulations of axisymmetric triaxial shear tests on dense noncohesive granular samples at zero gravity and low confining pressures. For different boundary conditions, I have found and described different shear band morphologies known from experiments. I have shown [74] that a spontaneous symmetry breaking strain localization develops if the platens of the shear cell are allowed to tilt.
(b) I have calculated different local quantities, which could be used to identify and locate the shear bands, and I have analyzed quantitatively their relationship. I have found [74] strong correlation of the local shear intensity (derived from the macroscopic strain tensor calculated from particle displacements) and the angular velocity of the grains, the coordination number, and the local void ratio. Among these quantities the local shear intensity and the angular velocity proved to be the most reliable indicators of shear bands.
- (IV) (a) In further three-dimensional distinct element simulations of triaxial shear tests, I have studied [72] the friction and density dependence of strain localization. Regarding the global behavior of a granular system undergoing a triaxial shear test, I have found that dense samples dilate while loose samples densify, which is in full accordance with experimental results and theoretical expectations.
(b) I have shown [72] that strain softening, along with shear band formation, appears and amplifies with increasing initial density and friction coefficient. If the symmetry is enforced, after the shear bands are formed, strain hardening sets in [74].
(c) Using a histogram technique, I have located the shear bands and I have measured the packing density η_{SB} in these regions. I have shown [72] that inside these failure zones the system self-organizes its density to a unique (critical) value η_c independent of the initial packing density. I have demonstrated that the criticality is confined to the shear bands.
(d) I have shown [72] that η_c depends on the coefficient of friction μ , and in the limit $\mu \rightarrow \infty$ it converges exponentially to a well-defined value η_c^∞ , which I have calculated for spherical grains with a narrow size distribution. I have argued that η_c^∞ defines a specific *dynamic random loose packing* (DRLP) state characteristic to the shear bands of granular materials.

Új tudományos eredmények

- (I) (a) Numerikus számításokkal megvizsgáltam [68] egy kétdimenziós mágneses szemcserendszerben a kölcsönhatás R levágási hosszának hatását. Egy ilyen rendszerben két jellemző lokális elrendeződés van: (1) egy ferromágneses, ami háromszögrácsba szervezi a dipólusokat, és (2) egy antiferromágneses, ami a négyzetögrácsos dipólus elrendeződéseket részesíti előnyben. Kimutattam [68], hogy a ferromágneses állapot sokkal érzékenyebb a levágási hosszra mint az antiferromágneses állapot.
- (b) Végtelen hatótávolság és nagy levágási hosszak esetén a ferromágneses állapot csekély mértékben kedvezőbb az antiferromágneses állapotnál. Ez megfordul $R \approx 4$ -nél és a ferromágneses állapot teljes eltünéséhez vezet $R \approx 2$ -nél. Kettős részecskeláncból álló ferromágneses és antiferromágneses rendszerek hajlításával kimutattam [68], hogy a tipikus helyi elrendeződéseket illetően jelentős változás áll be $R \approx 4$ és $R \approx 5$ között. A fentiekre alapozva az $R \approx 5$ választást javasoltam [68] a legalkisebb ésszerű levágási hossznak, ami dipoláris kemény golyókból álló kétdimenziós rendszerek szimulációiban alkalmazható.
- (II) (a) Mágneses szemcsékből álló kétdimenziós halmokat vizsgáltam [70] részecske alapú szimulációkban az $R = 6.25$ részecskeátmérőnyi levágási hossz mellett, ami biztosította, hogy a lokális elrendeződések, amik központi szerepet játszanak a szemcsés rendszerek dinamikájában, realisztikusak. Kimutattam [71], hogy a vizsgált mágnesezettségi tartományban mind a halmok rézsűszöge, mind a felszín érdessége lineárisan függ az f kölcsönhatási erőaránytól, amit a szemcsék érintkezésénél fellépő maximális mágneses erő és a gravitációs erő aránya definiál. Ez összhangban van a kísérletekből ismert mágnesezettségtől való kvadratikus függéssel.
- (b) A lavinák különböző keletkezési mechanizmusai szerint alacsony és magas f kölcsönhatási erőaránynál a fenti szimulációkban megkülönböztettem egy *szemcsés* és egy *korrelált tartományt* [71]. A két tartomány közötti átmenet nem éles. Egyszerű stabilitási kritériumokra alapozva megbecsültem az átmeneti pont helyét, amit a szimulációs eredmények alátámasztottak.
- (c) A szemcsés tartományban a lavinákat sűrűn egymást követő függőleges részecskeláncok jellemzik és átlagos lefutási idejük arányos a lavinák (golyószámban megadott) méretével. Továbbá, az átlagos lava áram (vagyis a lavinaméretek és az ezekhez tartozó átlagos lefutási idők aránya) lineárisan függ f -től. A lavinaméretek eloszlásának vizsgálatával kimutattam [71], hogy – kísérleti eredményekkel összhangban – létezik egy jellemző lavinaméret, ami arányos f -vel.
- (d) A korrelált tartományban a lavinák átlagos lefutási ideje arányos a lavinaméretek négyzetgyökével, f -től való minden további függés nélkül. Ezt a tartományra jellemző nagy és hosszú részecske-klaszterek szabadesése magyarázza. Megmutattam

[71], hogy a szemcsés tartományban jelen levő karakterisztikus méretet a korrelált tartományba való átmenetkor jelentkező nagy fluktuációk elnyomják, és ezt követően a lavinák csak egy f -fel arányosan növő jellegzetes hosszal rendelkeznek.

- (III) (a) Háromdimenziós részecske alapú szimulációkban tengelyszimmetrikus triaxiális nyírási teszteket végeztem [73] sűrű nemkohéziv szemcsés mintákkal, nulla gravitáció és alacsony nyomás mellett. Különböző peremfeltételekkel, kísérletekből ismert nyírási sáv-morfológiákat sikerült azonosítani és leírni. Kimutattam [74], hogy deformáció-lokalizáció során spontán szimmetriasértés jelentkezik, ha a nyírási cella nyomólemeze elbillenhet.
- (b) Nyírási sávok azonosítására és behatárolására használható különböző lokális mennyiségeket számoltam és megvizsgáltam azok kvantitatív kapcsolatát. Erős korrelációt találtam [74] a (részecskék elmozdulásával a makroszkopikus deformáció tenzorból számolt) lokális nyírási intenzitás, valamint a szemcsék szögsebessége, a koordinációs szám és a lokális üreghányad között. Ezek közül a lokális nyírási intenzitás és a szemcsék szögsebessége jelezte legmegbízhatóbban a nyírási sávokat.
- (IV) (a) További háromdimenziós részecske alapú szimulációkkal, triaxiális nyírási tesztekben vizsgáltam [72] a deformáció-lokalizáció súrlódás- és sűrűség-függését. A globális viselkedést illetően kimutattam, hogy a sűrű minták kitágulnak, a ritka minták pedig sűrűsödnek a tesztek során, ami teljes egyezésben van a kísérleti eredményekkel és az elméleti várakozásokkal.
- (b) Megmutattam [72], hogy a deformációs felpuhulás, valamint a nyírási sávok kialakulása, a kezdeti sűrűség és a súrlódási együttható növekedésével jelenik meg és erősödik fel. Ha a szimmetriasértés nem jöhet létre, a nyírási sávok kialakulása után deformációs keményedés jelentkezik [74].
- (c) Egy hisztogram-technika segítségével azonosítottam a nyírási sávokat és megértem a η_{SB} térkitöltési hányadukat. Megmutattam [72], hogy ezekben a megsúszási zónákban a rendszer önszerveződő módon egy meghatározott (kritikus) η_c értékre állítja a szemcsesűrűségét függetlenül a kezdeti sűrűségtől. Bizonyítottam, hogy ez a jelenség kizárolag a nyírási sávokra korlátozódik.
- (d) Megmutattam [72], hogy η_c függ a μ súrlódási együtthatótól és a $\mu \rightarrow \infty$ határesetben exponenciálisan konvergál egy jól definiált η_c^∞ értékhez, amit meghatároztam keskeny méreteloszlású gömb alakú szemcsékre. Amellett érveltem, hogy η_c^∞ egy *dinamikus véletlen ritka pakolást* definiál, ami jellemző a szemcsés anyagokban jelentkező nyírási sávokra.

Appendix

Appendix A

Tangential force in three-dimensional contacts

In common “soft-body” distinct element simulations, when two elements come into contact, a “tangential spring” of zero initial elongation is created. This imaginary spring, acting strictly in the tangential direction, connects the two bodies until they separate. The resulting tangential force \mathbf{F}_t is calculated as

$$\mathbf{F}_t = -\kappa_t \mathbf{u}_t - \gamma_t \mathbf{v}_t, \quad (\text{A.1})$$

where κ_t and γ_t are elastic and damping parameters depending on material properties, \mathbf{v}_t is the relative tangential velocity of the two bodies in contact, and \mathbf{u}_t encodes the spring’s elongation and the orientation of its action.

Usually, \mathbf{u}_t is calculated by integrating \mathbf{v}_t during the contact’s lifetime, i.e.

$$\mathbf{u}_t(t) = \int \mathbf{v}_t(t) \, dt. \quad (\text{A.2})$$

The integral must be calculated in the tangential plane. In a three-dimensional case both \mathbf{u}_t and \mathbf{v}_t are in fact two-dimensional vectors embedded in this plane. Because the tangential plane can change its orientation as the system evolves, care must be taken in order to update the orientation of \mathbf{u}_t accordingly.

Calculating the integral given in Eq. (A.2), in a two-dimensional case, is very simple. Both the spring’s elongation and the tangential velocity can be represented as scalars and thus the integral can be reduced to a simple scalar integral. Below we show how this integral is calculated in a three-dimensional case.

Let us consider that at a given time t the contact’s normal vector is $\mathbf{n}(t)$ and after some small time step δt this becomes $\mathbf{n}(t + \delta t)$. Let us assume that $\mathbf{n}(t)$ changes according to an infinitesimal rotation having its axis in the tangential plane. This is a natural assumption for rigid body contacts. According to this

$$\mathbf{n}(t + \delta t) = \mathbf{n}(t) + \boldsymbol{\delta\omega} \times \mathbf{n}(t), \quad (\text{A.3})$$

where “ \times ” denotes vector product, $\boldsymbol{\delta\omega}$ describes the infinitesimal rotation in question, and $\boldsymbol{\delta\omega} \cdot \mathbf{n}(t) = 0$. Here “ \cdot ” denotes scalar product.

Taking the vector product of both sides of Eq. (A.3) with $\mathbf{n}(t)$, it is easy to show that the infinitesimal angular change can be expressed as

$$\boldsymbol{\delta\omega} = \mathbf{n}(t) \times \mathbf{n}(t + \delta t). \quad (\text{A.4})$$

Applying the same rotation to $\mathbf{u}_t(t)$, we have

$$\mathbf{u}'_t(t) = \mathbf{u}_t(t) + \boldsymbol{\delta\omega} \times \mathbf{u}_t(t). \quad (\text{A.5})$$

Taking into consideration that $\mathbf{u}_t(t)$ lies in the tangential plane (i.e. $\mathbf{n}(t) \cdot \mathbf{u}_t(t) = 0$) and using the expression of $\boldsymbol{\delta\omega}$, the above equation leads to

$$\mathbf{u}'_t(t) = \mathbf{u}_t(t) - \mathbf{n}(t)(\mathbf{n}(t + \delta t) \cdot \mathbf{u}_t(t)). \quad (\text{A.6})$$

Because of numerical errors $\mathbf{u}'_t(t)$ might not fall exactly into the rotated tangential plane, and thus it might not be perpendicular to $\mathbf{n}(t + \delta t)$. To enforce this constraint, one can project $\mathbf{u}'_t(t)$ onto the rotated tangential plane by calculating

$$\mathbf{u}''_t(t) = \mathbf{u}'_t(t) - \mathbf{n}(t + \delta t)(\mathbf{n}(t + \delta t) \cdot \mathbf{u}'_t(t)). \quad (\text{A.7})$$

If $\mathbf{u}'_t(t)$ was already in the rotated tangential plane, then $\mathbf{u}''_t(t) = \mathbf{u}'_t(t)$. Otherwise, a small correction is added.

Finally, using $\mathbf{u}''_t(t)$, the spring's elongation state at time $t + \delta t$, can be calculated with the formula

$$\mathbf{u}_t(t + \delta t) = \mathbf{u}''_t(t) + \mathbf{v}_t(t + \delta t)\delta t. \quad (\text{A.8})$$

Observe that for computing $\mathbf{u}_t(t + \delta t)$, the new normal vector $\mathbf{n}(t + \delta t)$, the new relative tangential velocity $\mathbf{v}_t(t + \delta t)$, as well as the old normal vector $\mathbf{n}(t)$ and the old directional elongation $\mathbf{u}_t(t)$ are needed. In order to initialize the recursion, at time t_0 , when the contact and the tangential spring are created, one should take $\mathbf{u}_t(t_0) = 0$ and should store the contact's normal vector $\mathbf{n}(t_0)$.

Appendix B

Rotation integration in quaternion representation

Quaternions were introduced by Hamilton, in 1843, as a non-commutative extension to complex numbers. They form a four-dimensional normed division algebra over the real numbers [241]. The components of a quaternion are usually grouped into a vector and a scalar part. With usual notation, $q = [\mathbf{v}, s]$ is a quaternion having vector part $\mathbf{V}(q) = \mathbf{v}$ and scalar part $S(q) = s$. The conjugate of q is $q^* = [-\mathbf{v}, s]$.

Adding quaternions is done on a component-by-component basis, i.e.

$$q_1 + q_2 = [\mathbf{v}_1, s_1] + [\mathbf{v}_2, s_2] = [\mathbf{v}_1 + \mathbf{v}_2, s_1 + s_2]. \quad (\text{B.1})$$

The multiplication rule is

$$q_1 q_2 = [\mathbf{v}_1, s_1][\mathbf{v}_2, s_2] = [\mathbf{v}_1 \times \mathbf{v}_2 + s_1 \mathbf{v}_2 + s_2 \mathbf{v}_1, s_1 s_2 - \mathbf{v}_1 \cdot \mathbf{v}_2], \quad (\text{B.2})$$

where “ \times ” and “ \cdot ” denote vector and scalar product. With the above operations and the absolute value defined as

$$|q| = \sqrt{q q^*} = \sqrt{\|\mathbf{v}\|^2 + s^2}, \quad (\text{B.3})$$

quaternions form a Banach algebra. Scalars and vectors are embedded.

An arbitrary unit quaternion, i.e. a quaternion having $|q| = 1$, describes a three-dimensional rotation. If $q = [(x, y, z), s]$ and $x^2 + y^2 + z^2 + s^2 = 1$, then the corresponding rotation matrix is

$$\mathbf{R} = \begin{bmatrix} 1 - 2y^2 - 2z^2 & 2xy - 2sz & 2xz + 2sy \\ 2xy + 2sz & 1 - 2x^2 - 2z^2 & 2yz - 2sx \\ 2xz - 2sy & 2yz + 2sx & 1 - 2x^2 - 2y^2 \end{bmatrix}. \quad (\text{B.4})$$

Notice that no trigonometric function is involved in switching to matrix representation. The quaternion $q = [\sin(\varphi/2) \mathbf{n}, \cos(\varphi/2)]$ describes a rotation with angle φ around the unit axis \mathbf{n} . Multiplication of quaternions combines rotations.

Considering a reference position, a unit quaternion can also describe the arbitrary orientation of a body. Changes due to rotation with an angular velocity $\boldsymbol{\omega}$ are governed by the differential equation

$$\dot{q} = 1/2 \boldsymbol{\omega} q. \quad (\text{B.5})$$

With Euler's method, this can be solved as

$$q(t + \delta t) = q(t) + \boldsymbol{\omega}(t) q(t) \delta t / 2, \quad (\text{B.6})$$

where δt is a small time step. The constraint $|q(t + \delta t)| = 1$ can be enforced by considering the numerical regularization

$$q(t + \delta t) \leftarrow q(t + \delta t) / |q(t + \delta t)|. \quad (\text{B.7})$$

For deriving a higher order integration scheme similar to Verlet's Leap-Frog method, let us differentiate Eq. (B.5) with respect to t and obtain

$$\ddot{q} = 1/2 [\boldsymbol{\beta}, -1/2 \boldsymbol{\omega} \cdot \boldsymbol{\omega}] q, \quad (\text{B.8})$$

where $\boldsymbol{\beta} = \dot{\boldsymbol{\omega}}$ is the angular acceleration. Introducing the “quaternion velocity” $p = \dot{q}$ and “acceleration” $s = \ddot{q}$, based on Eq. (B.5) and Eq. (B.8) we have

$$p(t) = 1/2 \boldsymbol{\omega}(t) q(t) \quad (\text{B.9})$$

$$s(t) = 1/2 [\boldsymbol{\beta}(t), -1/2 \boldsymbol{\omega}(t) \cdot \boldsymbol{\omega}(t)] q(t). \quad (\text{B.10})$$

In intermediate steps, $p(t + \delta t/2)$ is calculated with the recursive formula

$$p(t + \delta t/2) = p(t - \delta t/2) + s(t) \delta t, \quad (\text{B.11})$$

initialized with

$$p(t - \delta t/2) = p(t) - s(t) \delta t/2. \quad (\text{B.12})$$

The new orientation and velocity is then obtained as

$$q(t + \delta t) = q(t) + p(t + \delta t/2) \delta t, \quad (\text{B.13})$$

$$p(t + \delta t) = 2p(t + \delta t/2) - p(t). \quad (\text{B.14})$$

From Eq. (B.9) it follows that $S(pq^*) = 0$. Due to numerical errors, the quaternion velocity $p(t + \delta t)$ calculated with the above integration scheme may fail to satisfy this constraint. Based on the identity

$$S((p - S(pq^*)q)q^*) = S(pq^*) - S(pq^*)S(qq^*) = 0, \quad (\text{B.15})$$

one can enforce the constraint in question by using the regularization

$$p(t + \delta t) \leftarrow p(t + \delta t) - S(p(t + \delta t) q^*(t + \delta t)) q(t + \delta t). \quad (\text{B.16})$$

Before regularizing p , enforcing $|q| = 1$ should be considered.

Finally, the orientation of the body can be extracted from q , while the angular velocity can be obtained as $\boldsymbol{\omega} = 2\mathbf{V}(pq^*)$. The integration scheme presented above gives a fast and robust method.

Appendix C

Ground state of a two-dimensional system of dipoles

We calculate the ground state of a two-dimensional system of dipoles placed on a rhombic lattice with rhombicity angle α and lattice constant a . The Hamiltonian of this system is

$$H = \frac{1}{2} \sum_{i \neq j} \sum_{u,v} J_{ij}^{uv} s_i^u s_j^v, \quad (\text{C.1})$$

where

$$J_{ij}^{uv} = \frac{1}{r_{ij}^3} \left(\delta_{uv} - 3 \frac{r_{ij}^u r_{ij}^v}{r_{ij}^2} \right), \quad (\text{C.2})$$

i and j run over the lattice points, $u, v \in \{x, y\}$ denote dipole components (see the coordinate system on Fig. C.1), δ_{uv} is the Kronecker delta, and r_{ij} is the length of the vector with components r_{ij}^x and r_{ij}^y pointing from lattice point i to lattice point j .

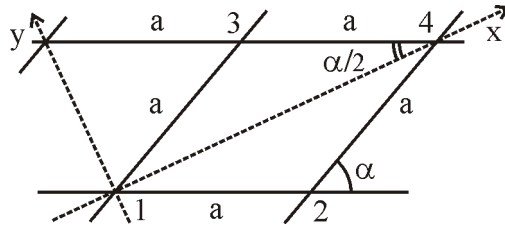


Figure C.1: Definition of the (x, y) coordinate system of a rhombic lattice with lattice constant a and rhombicity angle α .

The rhombic lattice can be divided into four rhombic sublattices each having the same rhombicity angle α and lattice constant $2a$. Let $\Gamma(i)$ denote the set of point indices of the sublattice containing the point indexed on the original lattice by $i = \overline{1,4}$ (see Fig. C.1). Following Luttinger and Tisza [148] we suppose that the ground state of the dipole system has a discrete translational symmetry. According to this, we consider that the dipoles are identical on each sublattice (i.e. $\forall i' \in \Gamma(i) : s_{i'} = s_i$) and we rewrite the Hamiltonian to

$$H = N_{\text{cell}} \frac{1}{2} \sum_{i,j=1}^4 \sum_{u,v} A_{ij}^{uv} s_i^u s_j^v, \quad (\text{C.3})$$

where N_{cell} is the number of lattice cells and

$$A_{ij}^{uv} = \sum_{j' \in \Gamma(j), j' \neq i} J_{ij'}^{uv}. \quad (\text{C.4})$$

Consequently, taking in consideration that there are 4 dipoles per lattice cell, the energy per dipole is

$$E = \frac{1}{8} \sum_{i,j=1}^4 \sum_{u,v} A_{ij}^{uv} s_i^u s_j^v. \quad (\text{C.5})$$

Introducing first a matrix notation

$$\mathbf{A}_{ij} = \begin{bmatrix} A_{ij}^{xx} & A_{ij}^{xy} \\ A_{ij}^{yx} & A_{ij}^{yy} \end{bmatrix} \text{ and } \mathbf{s}_i = \begin{bmatrix} s_i^x \\ s_i^y \end{bmatrix}, \quad (\text{C.6})$$

then a hyper-matrix notation

$$\hat{\mathbf{A}} = \begin{bmatrix} \mathbf{A}_{11} & \mathbf{A}_{12} & \mathbf{A}_{13} & \mathbf{A}_{14} \\ \mathbf{A}_{12} & \mathbf{A}_{11} & \mathbf{A}_{14} & \mathbf{A}_{13} \\ \mathbf{A}_{13} & \mathbf{A}_{14} & \mathbf{A}_{11} & \mathbf{A}_{12} \\ \mathbf{A}_{14} & \mathbf{A}_{13} & \mathbf{A}_{12} & \mathbf{A}_{11} \end{bmatrix} \text{ and } \hat{\mathbf{s}} = \begin{bmatrix} \mathbf{s}_1 \\ \mathbf{s}_2 \\ \mathbf{s}_3 \\ \mathbf{s}_4 \end{bmatrix}, \quad (\text{C.7})$$

the energy per dipole can be written in a more compact form as

$$E = \frac{1}{8} \hat{\mathbf{s}}^T \hat{\mathbf{A}} \hat{\mathbf{s}}, \quad (\text{C.8})$$

where $\hat{\mathbf{s}}^T$ is the transpose of \mathbf{s} . In the expression of $\hat{\mathbf{A}}$, we have taken into consideration that from symmetry it follows that

$$\mathbf{A}_{ij} = \mathbf{A}_{ji}, \mathbf{A}_{ii} = \mathbf{A}_{11}, \mathbf{A}_{23} = \mathbf{A}_{14}, \mathbf{A}_{24} = \mathbf{A}_{13}, \text{ and } \mathbf{A}_{34} = \mathbf{A}_{12}. \quad (\text{C.9})$$

It is easy to show that $\hat{\mathbf{A}}$ can be transformed into a block-diagonal form using the orthonormal transformation

$$\hat{\mathbf{O}} = \frac{1}{2} \begin{bmatrix} \mathbf{1} & \mathbf{1} & \mathbf{1} & \mathbf{1} \\ \mathbf{1} & -\mathbf{1} & -\mathbf{1} & \mathbf{1} \\ \mathbf{1} & \mathbf{1} & -\mathbf{1} & -\mathbf{1} \\ \mathbf{1} & -\mathbf{1} & \mathbf{1} & -\mathbf{1} \end{bmatrix}, \quad (\text{C.10})$$

where $\mathbf{1}$ denotes the 2×2 identity matrix. From simple calculations follows that

$$\hat{\mathbf{A}}' = \hat{\mathbf{O}} \hat{\mathbf{A}} \hat{\mathbf{O}}^T = \begin{bmatrix} \mathbf{L}_1 & 0 & 0 & 0 \\ 0 & \mathbf{L}_2 & 0 & 0 \\ 0 & 0 & \mathbf{L}_3 & 0 \\ 0 & 0 & 0 & \mathbf{L}_4 \end{bmatrix}, \quad (\text{C.11})$$

where $\hat{\mathbf{O}}^T$ is the transpose of $\hat{\mathbf{O}}$ and the 2×2 matrices \mathbf{L}_i are

$$\begin{aligned} \mathbf{L}_1 &= \mathbf{A}_{11} + \mathbf{A}_{12} + \mathbf{A}_{13} + \mathbf{A}_{14}, \\ \mathbf{L}_2 &= \mathbf{A}_{11} - \mathbf{A}_{12} - \mathbf{A}_{13} + \mathbf{A}_{14}, \\ \mathbf{L}_3 &= \mathbf{A}_{11} + \mathbf{A}_{12} - \mathbf{A}_{13} - \mathbf{A}_{14}, \\ \mathbf{L}_4 &= \mathbf{A}_{11} - \mathbf{A}_{12} + \mathbf{A}_{13} - \mathbf{A}_{14}. \end{aligned} \quad (\text{C.12})$$

In the above block-diagonal form, solving the eigenvalue problem of $\hat{\mathbf{A}}$, is very easy. The eigenvalues ε_k ($k = \overline{1, 8}$) of $\hat{\mathbf{A}}$ are equal to the eigenvalues of $\hat{\mathbf{A}}'$, which in turn are given by the eigenvalues of the 2×2 matrices \mathbf{L}_i . The eigenvectors $\hat{\mathbf{e}}'_k$ of $\hat{\mathbf{A}}'$ can be easily constructed from the eigenvectors of \mathbf{L}_i . The eigenvectors of $\hat{\mathbf{A}}$ are $\hat{\mathbf{e}}_k = \hat{\mathbf{O}}^T \hat{\mathbf{e}}'_k$.

By definition the matrices \mathbf{A}_{ij} are symmetric, i.e. $A_{ij}^{xy} = A_{ij}^{yx}$. With further symmetry considerations regarding the lattice, it can be shown that

$$A_{11}^{xy} = A_{14}^{xy} = 0, \quad A_{12}^{xy} = -A_{13}^{xy}, \quad A_{12}^{xx} = A_{13}^{xx}, \quad \text{and} \quad A_{12}^{yy} = A_{13}^{yy}. \quad (\text{C.13})$$

Based on this and Eq. (C.12) follows that the matrices \mathbf{L}_i are symmetric and

$$\begin{aligned} \mathbf{L}_1 &= \begin{bmatrix} A_{11}^{xx} + 2A_{12}^{xx} + A_{14}^{xx} & 0 \\ 0 & A_{11}^{yy} + 2A_{12}^{yy} + A_{14}^{yy} \end{bmatrix}, \\ \mathbf{L}_2 &= \begin{bmatrix} A_{11}^{xx} - 2A_{12}^{xx} + A_{14}^{xx} & 0 \\ 0 & A_{11}^{yy} - 2A_{12}^{yy} + A_{14}^{yy} \end{bmatrix}, \\ \mathbf{L}_3 &= \begin{bmatrix} A_{11}^{xx} - A_{14}^{xx} & 2A_{12}^{xy} \\ 2A_{12}^{xy} & A_{11}^{yy} - A_{14}^{yy} \end{bmatrix}, \\ \mathbf{L}_4 &= \begin{bmatrix} A_{11}^{xx} - A_{14}^{xx} & -2A_{12}^{xy} \\ -2A_{12}^{xy} & A_{11}^{yy} - A_{14}^{yy} \end{bmatrix}. \end{aligned} \quad (\text{C.14})$$

It can be observed that A_{11}^{uu} , A_{12}^{uu} , A_{14}^{uu} , and A_{12}^{xy} fully define \mathbf{L}_i . Moreover, assuming an infinite system with infinite interaction range, A_{14}^{uu} can be eliminated too.

The sum defining \mathbf{A}_{11} (see Eq. (C.4)) can be decomposed into components \mathbf{C}_j corresponding to sublattices, i.e.

$$\mathbf{A}_{11} = \sum_{j=1}^4 \mathbf{C}_j, \quad (\text{C.15})$$

where \mathbf{C}_j is defined by a similar sum to the one defining \mathbf{A}_{1j} (see Eq. (C.4)) but calculated on a lattice with double lattice constant. Consequently, based on Eq. (C.2), $\mathbf{C}_j = 1/8 \mathbf{A}_{1j}$, and thus

$$\mathbf{A}_{11} = \frac{1}{8} (\mathbf{A}_{11} + \mathbf{A}_{12} + \mathbf{A}_{13} + \mathbf{A}_{14}). \quad (\text{C.16})$$

Using the above equation and Eq. (C.13), A_{14}^{uu} can be expressed in function of A_{11}^{uu} and A_{12}^{uu} , which further simplifies the calculation of \mathbf{L}_i . Notice, however, that the above equation holds only for an infinite system with infinite interaction range. If one intends to do computation on a finite system or introduce a finite interaction cutoff then this simplification should not be used.

Now, we turn to the calculation of the eigenvalues and eigenvectors of $\hat{\mathbf{A}}$. For this, as it was already mentioned, we use the eigenvalues and eigenvectors of \mathbf{L}_i , which can be simply derived from Eq. (C.14).

According to this, the eigenvalues of $\hat{\mathbf{A}}$ are

$$\begin{aligned} \varepsilon_1 &= L_1^{xx}, \quad \varepsilon_2 = L_1^{yy}, \quad \varepsilon_3 = L_2^{xx}, \quad \varepsilon_4 = L_2^{yy}, \quad \text{and} \\ \varepsilon_{5,6} &= \varepsilon_{7,8} = 1/2 \left(\text{tr}(L_3) \pm \sqrt{\text{tr}(L_3)^2 - 4\det(L_3)} \right). \end{aligned} \quad (\text{C.17})$$

Here $\text{tr}(\cdot)$ and $\det(\cdot)$ denote trace and determinant, and thus

$$\text{tr}(L_3) = L_3^{xx} + L_3^{yy}, \quad \text{and} \quad \det(L_3) = L_3^{xx} L_3^{yy} - (L_3^{xy})^2. \quad (\text{C.18})$$

With the notations $\xi = \cos(\varphi)$ and $\sigma = \sin(\varphi)$, and φ defined by

$$\tan(\varphi) = (\varepsilon_5 - L_3^{xx})/L_3^{xy}, \quad (\text{C.19})$$

the corresponding eigenvectors are

$$\begin{aligned} \hat{\mathbf{e}}_1 &= \begin{bmatrix} 1 \\ 0 \\ 1 \\ 0 \\ 1 \\ 0 \\ 1 \\ 0 \end{bmatrix}, \quad \hat{\mathbf{e}}_2 = \begin{bmatrix} 0 \\ 1 \\ 0 \\ 1 \\ 0 \\ 1 \\ 0 \\ 1 \end{bmatrix}, \quad \hat{\mathbf{e}}_3 = \begin{bmatrix} 1 \\ 0 \\ -1 \\ 0 \\ 0 \\ 1 \\ 0 \\ 0 \end{bmatrix}, \quad \hat{\mathbf{e}}_4 = \begin{bmatrix} 0 \\ 1 \\ 0 \\ -1 \\ 0 \\ 0 \\ 1 \\ 1 \end{bmatrix}, \\ \hat{\mathbf{e}}_5 &= \begin{bmatrix} \xi \\ \sigma \\ \xi \\ -\sigma \\ \sigma \\ -\xi \\ -\sigma \\ -\xi \\ -\sigma \end{bmatrix}, \quad \hat{\mathbf{e}}_6 = \begin{bmatrix} -\sigma \\ \xi \\ \xi \\ -\sigma \\ \xi \\ \sigma \\ -\xi \\ \sigma \\ -\xi \end{bmatrix}, \quad \hat{\mathbf{e}}_7 = \begin{bmatrix} \xi \\ -\sigma \\ -\xi \\ \sigma \\ \xi \\ -\sigma \\ -\xi \\ \sigma \\ -\xi \end{bmatrix}, \quad \hat{\mathbf{e}}_8 = \begin{bmatrix} \sigma \\ \xi \\ -\xi \\ -\sigma \\ \sigma \\ -\sigma \\ -\xi \\ \sigma \\ -\xi \end{bmatrix}. \end{aligned} \quad (\text{C.20})$$

It can be observed that the eigenvalues and eigenvectors are fully defined by L_1^{uu} , L_2^{uu} , L_3^{uu} and L_3^{xy} . It can be also observed that $\hat{\mathbf{e}}_k^T \hat{\mathbf{e}}_{k'} = 4\delta_{kk'}$, i.e. the eigenvectors form an orthogonal system and each eigenvector is normalized to $\|\hat{\mathbf{e}}_k\|=2$. This was chosen in order to have the orthogonal vectors $\mathbf{e}_{k,i}$, which build up the eigenvectors

$$\hat{\mathbf{e}}_k = \begin{bmatrix} \mathbf{e}_{k,1} \\ \mathbf{e}_{k,2} \\ \mathbf{e}_{k,3} \\ \mathbf{e}_{k,4} \end{bmatrix}, \quad (\text{C.21})$$

normalized to $\|\mathbf{e}_{k,i}\| = 1$.

For a dipole arrangement $\hat{\mathbf{s}}$ given in the orthogonal eigenvector system $\hat{\mathbf{e}}_k$, i.e. for

$$\hat{\mathbf{s}} = \sum_{k=1}^8 b_k \hat{\mathbf{e}}_k \quad (\text{C.22})$$

the energy per dipole (see Eq. (C.8)) is

$$E = \frac{1}{2} \sum_{k=1}^8 \varepsilon_k b_k^2. \quad (\text{C.23})$$

If all dipoles have equal magnitude S , then b_k satisfies for every $i = \overline{1,4}$ the equation

$$\left(\sum_{k=1}^8 b_k e_{k,i}^x \right)^2 + \left(\sum_{k=1}^8 b_k e_{k,i}^y \right)^2 = S^2. \quad (\text{C.24})$$

Summing up these equations follows that b_k must satisfy

$$\sum_{k=1}^8 b_k^2 = S^2. \quad (\text{C.25})$$

In this case, based on Eq. (C.23), the minimum of E , i.e. the ground state energy per dipole is

$$E_0 = \frac{1}{2} \varepsilon_{min} S^2, \quad (\text{C.26})$$

where $\varepsilon_{min} = \min_k(\varepsilon_k)$.

If there is one single k_{min} such that $\varepsilon_{k_{min}} = \varepsilon_{min}$, then the ground state $\hat{\mathbf{s}}_0$ is defined by the corresponding eigenvector $\hat{\mathbf{e}}_{k_{min}}$, i.e. $\hat{\mathbf{s}}_0 = S \hat{\mathbf{e}}_{k_{min}}$. Otherwise the ground state is given by the linear combination

$$\hat{\mathbf{s}}_0 = \sum_{k \in \mathcal{K}_{min}} b_k \hat{\mathbf{e}}_k, \quad (\text{C.27})$$

where $\mathcal{K}_{min} = \{k : \varepsilon_k = \varepsilon_{min}\}$ and the arbitrary weights b_k satisfy the equation

$$\sum_{k \in \mathcal{K}_{min}} b_k^2 = S^2. \quad (\text{C.28})$$

Notice that in the latter case the ground state of the dipole system has a continuous degeneracy of order $|\mathcal{K}_{min}|$.

Appendix D

Magnetic dipole-dipole interaction

Let us consider two particles with magnetic dipoles \mathbf{m}_1 and \mathbf{m}_2 . We calculate the magnetic dipole-dipole force and torque exerted on each other by these two particles. The dipole magnetic field of particle (1) at the position of particle (2) is

$$\mathbf{B}_{21} = \frac{\mu_0}{4\pi} \frac{1}{r_{21}^3} [3 (\mathbf{n}_{21}\mathbf{m}_1) \mathbf{n}_{21} - \mathbf{m}_1], \quad (\text{D.1})$$

where $\mathbf{n}_{21} = \mathbf{r}_{21}/r_{21}$ is the unit vector pointing from particle (1) to particle (2), and r_{21} is the distance between the particles. The above formula can be also written as

$$\mathbf{B}_{21} = \frac{\mu_0}{4\pi} \left[3 \frac{(\mathbf{r}_{21}\mathbf{m}_1)}{r_{21}^5} \mathbf{r}_{21} - \frac{1}{r_{21}^3} \mathbf{m}_1 \right]. \quad (\text{D.2})$$

The magnetic force and torque exerted by particle (1) on particle (2) is

$$\mathbf{F}_{21} = \nabla (\mathbf{B}_{21}\mathbf{m}_2) = (\nabla \circ \mathbf{B}_{21}) \mathbf{m}_2 \quad (\text{D.3})$$

and

$$\mathbf{T}_{21} = \mathbf{m}_2 \times \mathbf{B}_{21}, \quad (\text{D.4})$$

where ∇ is the gradient operator, \circ denotes dyadic product and \times denotes vector product.

With arbitrary f and \mathbf{g} , scalar and vector functions, one can easily check that

$$\nabla \circ (f(r_{21}) \mathbf{g}(\mathbf{r}_{21})) = \nabla (f(r_{21})) \circ \mathbf{g}(\mathbf{r}_{21}) + f(r_{21}) (\nabla \circ \mathbf{g}(\mathbf{r}_{21})). \quad (\text{D.5})$$

Consequently, with the unit matrix \mathbf{I} , and the scalar and vector constants α and \mathbf{c} ,

$$\nabla \circ \mathbf{r}_{21} = \mathbf{I}, \quad (\text{D.6})$$

$$\nabla \circ (r_{21}^\alpha \mathbf{c}) = \alpha r_{21}^{\alpha-2} (\mathbf{r}_{21} \circ \mathbf{c}), \quad (\text{D.7})$$

$$\nabla (r_{21}^\alpha) = \alpha r_{21}^{\alpha-2} \mathbf{r}_{21}. \quad (\text{D.8})$$

Using the above formulas we first concentrate on calculating $(\nabla \circ \mathbf{B}_{21})$. The first term of \mathbf{B}_{21} from Eq. (D.2) gives

$$\nabla \circ \left[3 \frac{(\mathbf{r}_{21}\mathbf{m}_1)}{r_{21}^5} \mathbf{r}_{21} \right] = 3 \nabla \left[\frac{(\mathbf{r}_{21}\mathbf{m}_1)}{r_{21}^5} \right] \circ \mathbf{r}_{21} + 3 \frac{(\mathbf{r}_{21}\mathbf{m}_1)}{r_{21}^5} \mathbf{I}. \quad (\text{D.9})$$

Evaluating the first term of the above expression, we have

$$\nabla \left[\frac{(\mathbf{r}_{21}\mathbf{m}_1)}{r_{21}^5} \right] = \frac{1}{r_{21}^5} \nabla(\mathbf{r}_{21}\mathbf{m}_1) + (\mathbf{r}_{21}\mathbf{m}_1) \nabla \frac{1}{r_{21}^5}. \quad (\text{D.10})$$

Using

$$\nabla(\mathbf{r}_{21}\mathbf{m}_1) = (\nabla \circ \mathbf{r}_{21}) \mathbf{m}_1 = \mathbf{m}_1, \quad (\text{D.11})$$

$$\nabla \frac{1}{r_{21}^5} = -5 \frac{1}{r_{21}^7} \mathbf{r}_{21}, \quad (\text{D.12})$$

this leads to

$$\nabla \left[\frac{(\mathbf{r}_{21}\mathbf{m}_1)}{r_{21}^5} \right] = \frac{1}{r_{21}^5} \mathbf{m}_1 - 5 \frac{(\mathbf{r}_{21}\mathbf{m}_1)}{r_{21}^7} \mathbf{r}_{21}. \quad (\text{D.13})$$

Substituting it back into Eq. (D.9), we finally have

$$\nabla \circ \left[3 \frac{(\mathbf{r}_{21}\mathbf{m}_1)}{r_{21}^5} \mathbf{r}_{21} \right] = 3 \frac{1}{r_{21}^5} (\mathbf{m}_1 \circ \mathbf{r}_{21}) - 15 \frac{(\mathbf{r}_{21}\mathbf{m}_1)}{r_{21}^7} (\mathbf{r}_{21} \circ \mathbf{r}_{21}) + 3 \frac{(\mathbf{r}_{21}\mathbf{m}_1)}{r_{21}^5} \mathbf{I}. \quad (\text{D.14})$$

In a similar way, the second term of \mathbf{B}_{21} from Eq. (D.2) gives

$$\nabla \circ \left[-\frac{1}{r_{21}^3} \mathbf{m}_1 \right] = 3 \frac{1}{r_{21}^5} (\mathbf{r}_{21} \circ \mathbf{m}_1). \quad (\text{D.15})$$

Using Eq. (D.3), Eq. (D.14), and Eq. (D.15),

$$\begin{aligned} \mathbf{F}_{21} = \frac{\mu_0}{4\pi} & \left[3 \frac{1}{r_{21}^5} \mathbf{m}_1 (\mathbf{r}_{21}\mathbf{m}_2) - 15 \frac{(\mathbf{r}_{21}\mathbf{m}_1)}{r_{21}^7} \mathbf{r}_{21} (\mathbf{r}_{21}\mathbf{m}_2) + \right. \\ & \left. + 3 \frac{(\mathbf{r}_{21}\mathbf{m}_1)}{r_{21}^5} \mathbf{m}_2 + 3 \frac{1}{r_{21}^5} \mathbf{r}_{21} (\mathbf{m}_1\mathbf{m}_2) \right]. \end{aligned} \quad (\text{D.16})$$

With some further simplifications, using $\mathbf{n}_{21} = \mathbf{r}_{21}/r_{21}$, we have

$$\begin{aligned} \mathbf{F}_{21} = \frac{\mu_0}{4\pi} \frac{3}{r_{21}^4} & [(\mathbf{n}_{21}\mathbf{m}_2) \mathbf{m}_1 - 5 (\mathbf{n}_{21}\mathbf{m}_1) (\mathbf{n}_{21}\mathbf{m}_2) \mathbf{n}_{21} + \\ & + (\mathbf{n}_{21}\mathbf{m}_1) \mathbf{m}_2 + (\mathbf{m}_1\mathbf{m}_2) \mathbf{n}_{21}]. \end{aligned} \quad (\text{D.17})$$

Because $\mathbf{n}_{12} = -\mathbf{n}_{21}$, the above formula is anti-symmetric with respect to particle change. Consequently, the force exerted by particle (2) on particle (1) is $\mathbf{F}_{12} = -\mathbf{F}_{21}$, which is in accordance with Newton's law of action and reaction.

Based on Eq. (D.4) and the expression of \mathbf{B}_{21} given in Eq. (D.1), the magnetic torque exerted by particle (1) on particle (2) is

$$\mathbf{T}_{21} = \frac{\mu_0}{4\pi} \frac{1}{r_{21}^3} [3 (\mathbf{n}_{21}\mathbf{m}_1) (\mathbf{m}_2 \times \mathbf{n}_{21}) - (\mathbf{m}_2 \times \mathbf{m}_1)]. \quad (\text{D.18})$$

Notice that the above expression is not anti-symmetric nor symmetric with respect to particle change, and thus \mathbf{T}_{12} (i.e. the magnetic torque exerted by particle (2) on particle (1)) cannot be calculated directly from \mathbf{T}_{21} .

From the above formulas, valid for a three-dimensional case, one can simply derive a two-dimensional version. However, in two-dimensions, choosing the coordinate system in

a specific way the calculations can be made more simple and more easy to implement in a computer program.

For this, let us first consider that the three-dimensional vector components are denoted by (x, y, z) and assume that the y component of the vectors \mathbf{m}_1 , \mathbf{m}_2 , and \mathbf{n}_{21} are all equal to 0. In this case F_{21}^y is zero, and thus we can neglect the y component in the calculations and use only the (x, z) components. Furthermore, without loss of generality, we can consider the rotation

$$\mathbf{R} = \begin{pmatrix} n_{21}^x & n_{21}^z \\ -n_{21}^z & n_{21}^x \end{pmatrix}, \quad (\text{D.19})$$

which takes n_{21}^z to 0.

Applying the above rotation on the magnetic dipole vectors \mathbf{m}_1 and \mathbf{m}_2 , in the transformed system the magnetic force exerted by particle (1) on particle (2) is

$$\mathbf{F}_{21} = \frac{\mu_0}{4\pi} \frac{3}{r_{21}^4} \begin{pmatrix} -2 m_1^x m_2^x + m_1^z m_2^z \\ m_1^z m_2^x + m_1^x m_2^z \end{pmatrix}. \quad (\text{D.20})$$

The inverse transformation (i.e. \mathbf{R}^T) can be then applied on \mathbf{F}_{21} to transform it back to the original coordinate system. It may be surprising at first that the above expression is symmetric with respect to particle change. Notice that the anti-symmetry required by Newton's law of action and reaction is carried by \mathbf{R} .

In a similar way, the x and z components of the magnetic torque are zero, and in the transformed system

$$T_{21}^y = \frac{\mu_0}{4\pi} \frac{1}{r_{21}^3} [2 m_1^x m_2^z + m_1^z m_2^x]. \quad (\text{D.21})$$

Because T_{21}^y is invariant to the rotation \mathbf{R} , the value calculated with the above formula is valid in the original coordinate system too.

Appendix E

Otsu's threshold selection method

Otsu's threshold selection method [173] is a histogram technique known from Digital Image Processing, where it is typically used to transform grayscale images into two component (black and white) images.

Let us consider a normalized histogram $P(i)$, i.e. a histogram with the property

$$\sum_{i=0}^{n-1} P(i) = 1, \quad (\text{E.1})$$

where n is the number of histogram bins, i is the bin index, and all $P(i)$ values are non-negative. The mean μ and the variance σ^2 can be calculated as

$$\mu = \sum_{i=0}^{n-1} i P(i), \quad (\text{E.2})$$

$$\sigma^2 = \sum_{i=0}^{n-1} (i - \mu)^2 P(i). \quad (\text{E.3})$$

Let us further consider a candidate threshold t and split the histogram into two parts $\mathcal{I}_1(t) = \{i : 0 \leq i \leq t\}$ and $\mathcal{I}_2(t) = \{i : t < i < n\}$. With the notation

$$q_k(t) = \sum_{i \in \mathcal{I}_k(t)} P(i), \quad (\text{E.4})$$

where $k \in \{1, 2\}$, the mean $\mu_k(t)$ and variance $\sigma_k^2(t)$ of the two parts of the histogram satisfy the equations

$$q_k(t) \mu_k(t) = \sum_{i \in \mathcal{I}_k(t)} i P(i), \quad (\text{E.5})$$

$$q_k(t) \sigma_k^2(t) = \sum_{i \in \mathcal{I}_k(t)} (i - \mu_k(t))^2 P(i). \quad (\text{E.6})$$

The *within-class variance*

$$\sigma_W^2(t) = q_1(t) \sigma_1^2(t) + q_2(t) \sigma_2^2(t) \quad (\text{E.7})$$

and the *between-class variance*

$$\sigma_B^2(t) = q_1(t) q_2(t) (\mu_1(t) - \mu_2(t))^2 \quad (\text{E.8})$$

give an inverse measure of compactness ($\sigma_W^2(t)$) and a direct measure of separation ($\sigma_B^2(t)$) of classes. It is easy to show that $\sigma_W^2(t) + \sigma_B^2(t) = \sigma^2$. Otsu [173] proposed to calculate an optimal threshold $t = t_{opt}$ either by minimizing $\sigma_W^2(t)$ or by maximizing $\sigma_B^2(t)$. Maximizing $\sigma_B^2(t)$ is numerically more convenient.

It is easy to check that

$$q_2(t) = 1 - q_1(t), \quad (\text{E.9})$$

$$\mu_2(t) = \frac{\mu - q_1(t)\mu_1(t)}{q_2(t)}, \quad (\text{E.10})$$

and thus

$$\sigma_B^2(t) = \frac{q_1(t)}{1 - q_1(t)} (\mu_1(t) - \mu)^2, \quad (\text{E.11})$$

where $q_1(t)$ and $\mu_1(t)$ can be calculated with the recursive formula

$$q_1(t+1) = q_1(t) + P(t+1), \quad (\text{E.12})$$

$$\mu_1(t+1) = \frac{q_1(t) \mu_1(t) + (t+1) P(t+1)}{q_1(t+1)}, \quad (\text{E.13})$$

using $q_1(0) = P(0)$ and $\mu_1(0) = 0$. To avoid division by zero and keep the consistency of the calculation, if $q_1(t) = 0$, i.e. $\forall i \in [0, t] : P(i) = 0$, let $\mu_1(t) = 0$ and $\sigma_B^2(t) = 0$. Furthermore, if $q_1(t) = 1$, i.e. $\forall i \in [t+1, n-1] : P(i) = 0$, let $\mu_1(t) = \mu$ and $\sigma_B^2(t) = 0$.

The maximum point of $\sigma_B^2(t)$ is not necessarily unique. To break the possible ambiguity, let the optimal threshold t_{opt} be given by the smallest candidate threshold t for which $\sigma_B^2(t)$ takes its maximum, i.e. let

$$t_{opt} = \min \left\{ t : \sigma_B^2(t) = \max_s \sigma_B^2(s) \right\}. \quad (\text{E.14})$$

The method is very robust and fast, and because $\sigma_W^2(t) + \sigma_B^2(t) = \sigma^2$, it both minimizes the within-class variance and maximizes the separation of classes.

Bibliography

Bibliography

- [1] J. A. Åström, H. J. Herrmann, and J. Timonen. Granular packings and fault zones. *Physical Review Letters*, 84:638–641, 2000.
- [2] C. M. Aegerter, R. Günter, and R. J. Wijngaarden. Avalanche dynamics, surface roughening, and self-organized criticality: Experiments on a three-dimensional pile of rice. *Physical Review E*, 67:051306, 2003.
- [3] C. M. Aegerter, K. A. Lőrincz, M. S. Welling, and R. J. Wijngaarden. Extremal dynamics and the approach to the critical state: Experiments on a three dimensional pile of rice. *Physical Review Letters*, 92:058702, 2004.
- [4] C. M. Aegerter, K. A. Lőrincz, and R. J. Wijngaarden. A multi-scaling analysis of the surface of a three-dimensional pile of rice. *Europhysics Letters*, 67:342–348, 2004.
- [5] C. M. Aegerter, M. S. Welling, and R. J. Wijngaarden. Surface roughening and self-organized criticality: The influence of quenched disorder. *Europhysics Letters*, 74:397–403, 2006.
- [6] N. Akkiraju, H. Edelsbrunner, M. Facello, P. Fu, E. P. Mucke, and C. Varela. Alpha shapes: Definition and software. In *Proc. Internat. Comput. Geom. Software Workshop*, pages 63–66, 1995.
- [7] R. Albert, I. Albert, D. Hornbaker, P. Schiffer, and A. L. Barabási. Maximum angle of stability in wet and dry spherical granular media. *Physical Review E*, 56:R6271, 1997.
- [8] K. A. Alshibli, S. Sture, N. C. Costes, M. L. Frank, M. R. Lankton, S. N. Batiste, and R. A. Swanson. Assessment of localized deformations in sand using X-ray computed tomography. *Geotechnical Testing Journal*, 23:274–299, 2000.
- [9] E. Altshuler, O. Ramos, C. Martínez, L. E. Flores, and C. Noda. Avalanches in one-dimensional piles with different types of bases. *Physical Review Letters*, 86:5490–5493, 2001.
- [10] I. S. Aranson and L. S. Tsimring. Patterns and collective behavior in granular media: Theoretical concepts. *Reviews of Modern Physics*, 78:641–692, 2006.
- [11] T. Aste, M. Saadatfar, and T. J. Senden. Geometrical structure of disordered sphere packings. *Physical Review E*, 71:061302, 2005.
- [12] T. Aste and D. L. Weaire. *The Pursuit of Perfect Packing*. Institute of Physics - Bristol, 2000.

- [13] P. Bak, C. Tang, and K. Wiesenfeld. Self-organized criticality: An explanation of 1/f noise. *Physical Review Letters*, 59:381–384, 1987.
- [14] P. Bak, C. Tang, and K. Wiesenfeld. Self-organized criticality. *Physical Review A*, 38:364–375, 1988.
- [15] J. E. Barnes and P. Hut. A hierarchical $O(N \log N)$ force calculation algorithm. *Nature*, 324:446, 1986.
- [16] G. Bartels. *Mesoscopic Aspects of Solid Friction*. PhD thesis, University Duisburg-Essen, 2006.
- [17] S. N. Batiste, K. A. Alshibli, S. Sture, and M. Lankton. Shear band characterization of triaxial sand specimens using computed tomography. *Geotechnical Testing Journal*, 27:568–579, 2004.
- [18] N. Bell, Y. Yu, and P. J. Mucha. Particle-based simulation of granular materials. In K. Anjyo and P. Faloutsos, editors, *Proceedings of the 2005 ACM SIGGRAPH/Eurographics symposium on Computer animation*, pages 77–86. ACM Press - New York, 2005.
- [19] J. D. Bernal. *Proc. R. Soc. London*, A280:299, 1964.
- [20] D. L. Blair and A. Kudrolli. Clustering transitions in vibrofluidized magnetized granular materials. *Physical Review E*, 67:021302, 2003.
- [21] D. L. Blair and A. Kudrolli. Magnetized granular materials. In H. Hinrichsen and D. E. Wolf, editors, *The Physics of Granular Media*, pages 281–296. Wiley-VCH - Berlin, 2004.
- [22] L. Bocquet, E. Charlaix, S. Ciliberto, and J. Crassous. Moisture-induced ageing in granular media and the kinetics of capillary condensation. *Nature London*, 396:735, 1998.
- [23] J. P. Bouchaud. *Slow Relaxations and nonequilibrium dynamics in condensed matter*, chapter Granular Media: Some Ideas from Statistical Physics, pages 131–197. Springer - Berlin, Heidelberg, 2003.
- [24] J. P. Bouchaud, M. E. Cates, J. Ravi Prakash, and S. F. Edwards. Hysteresis and metastability in a continuum sandpile model. *Physical Review Letters*, 74:1982–1985, 1995.
- [25] J. P. Bouchaud, P. Claudin, M. E. Cates, and J. P. Wittmer. Models of stress propagation in granular media. In H. J. Herrmann, J.-P. Hovi, and S. Luding, editors, *Physics of Dry Granular Media*, page 97. Kluwer Academic Publishers - Dordrecht, 1998.
- [26] J. G. Brankov and D. M. Danchev. Ground state of an infinite two-dimensional system of dipoles on a lattice with arbitrary rhombicity angle. *Physica A*, 144:128–139, 1987.

- [27] L. Brendel and S. Dippel. Lasting contacts in molecular dynamics simulations. In H. J. Herrmann, J.-P. Hovi, and S. Luding, editors, *Physics of Dry Granular Media*, pages 313–318. Kluwer Academic Publishers - Dordrecht, 1998.
- [28] M. Bretz, J. B. Cunningham, P. L. Kurczynski, and F. Nori. Imaging of avalanches in granular materials. *Physical Review Letters*, 69:2431–2434, 1992.
- [29] N. V. Brilliantov and Th. Pöschel. *Kinetic Theory of Granular Gases*. Oxford University Press, 2004.
- [30] N. V. Brilliantov, F. Spahn, J.-M. Hertzsch, and T. Pöschel. Model for collisions in granular gases. *Physical Review E*, 53:5382, 1996.
- [31] K. Butter, P. H. H. Bomans, P. M. Frederik, G. J. Vroege, and A. P. Philipse. Direct observation of dipolar chains in iron ferrofluids by cryogenic electron microscopy. *Nature Materials*, 2:88–91, 2003.
- [32] A. Casagrande. Characteristics of cohesionless soils affecting the stability of slopes and earth fills. *Journal of the Boston Society of Civil Engineers*, 23:257–276, 1936.
- [33] A. Castellanos. The relationship between attractive interparticle forces and bulk behaviour in dry and uncharged fine powders. *Advances In Physics*, 54:263–376, 2005.
- [34] A. Castellanos, J. M. Valverde, A. T. Pérez, A. Ramos, and P. K. Watson. Flow regimes in fine cohesive powders. *Physical Review Letters*, 82:1156–1159, 1999.
- [35] A. Castellanos, J. M. Valverde, and M. A. S. Quintanilla. Fine cohesive powders in rotating drums: Transition from rigid-plastic flow to gas-fluidized regime. *Physical Review E*, 65:061301, 2002.
- [36] Computational Geometry Algorithms Library. www.cgal.org, 2003.
- [37] P. M. Chaikin. Thermodynamics and hydrodynamics of hard spheres: The role of gravity. In M. E. Cates and M. R. Evans, editors, *Soft and Fragile Matter, Nonequilibrium Dynamics, Metastability and Flow*, pages 315–348. Institute of Physics Publishing - London, 2000.
- [38] X. Cheng, J. B. Lechman, A. Fernandez-Barbero, G. S. Grest, H. M. Jaeger, G. S. Karczmar, M. E. Mobius, and S. R. Nagel. Three-dimensional shear in granular flow. *Physical Review Letters*, 96:038001, 2006.
- [39] K. Christensen, Á. Corral, V. Frette, J. Feder, and T. Jøssang. Tracer dispersion in a self-organized critical system. *Physical Review Letters*, 77:107–110, 1996.
- [40] J. H. Conway and N. J. A. Sloane. *Sphere Packings, Lattices, and Groups*. Springer-Verlag - New York, 1993.
- [41] R. M. Costello, K. L. Cruz, C. Egnatuk, D. T. Jacobs, M. C. Krivos, T. S. Louis, R. J. Urban, and H. Wagner. Self-organized criticality in a bead pile. *Physical Review E*, 67:041304, 2003.

- [42] C. A. Coulomb. Essai sur une application des règles de maximis et de minimis à quelques problèmes des statique, relatifs à l'architecture. In *Mémoires de Mathématique and de Physique*, volume 7, pages 343–382. Académie Royale des Sciences - Paris, 1773.
- [43] L. Cui and C. O’Sullivan. Development of a mixed boundary environment for axisymmetric DEM analyses. In R. García-Rojo, H. J. Herrmann, and S. McNamara, editors, *Powders and Grains*, pages 301–305. Balkema - London, 2005.
- [44] P. A. Cundall and O. D. L. Strack. A discrete numerical model for granular assemblies. *Geotechnique*, 29:47, 1979.
- [45] S. M. Dammer, J. Werth, and H. Hinrichsen. Electrostatically charged granular matter. In H. Hinrichsen and D. E. Wolf, editors, *The Physics of Granular Media*, pages 255–280. Wiley-VCH - Berlin, 2004.
- [46] D. Daudon, J. Lanier, and M. Jean. A micro mechanical comparison between experimental results and numerical simulation of a biaxial test on 2d granular material. In R. P. Behringer and J. T. Jenkins, editors, *Powders and Grains*, pages 219–222. Balkema, 1997.
- [47] P.-G. de Gennes. Granular matter: A tentative view. *Reviews of Modern Physics*, 71:S374–S382, 1999.
- [48] P.-G. de Gennes and P. A. Pincus. Pair correlations in a ferromagnetic colloid. *Zeitschrift für Physik B: Condensed Matter*, 11:189–198, 1970.
- [49] J. Desrues. Thèse de doctorat es science. USMG and INPG (Grenoble), 1984.
- [50] J. Desrues. Tracking strain localization in geomaterials using computerized tomography. In J. Otani and Yuzo Obara, editors, *X-ray CT for Geomaterials*, pages 15–41. Balkema, 2004.
- [51] J. Desrues, R. Chambon, M. Mokni, and F. Mazerolle. Void ratio evolution inside shear bands in triaxial sand specimens studied by computed tomography. *Geotechnique*, 46:529–546, 1996.
- [52] J. Desrues and G. Viggiani. Strain localization in sand: An overview of the experimental results obtained in grenoble using stereophotogrammetry. *International Journal for Numerical and Analytical Methods in Geomechanics*, 28:279–321, 2004.
- [53] A. Donev, I. Cisse, D. Sachs, E. A. Variano, F. H. Stillinger, R. Connelly, S. Torquato, and P. M. Chaikin. Improving the density of jammed disordered packings using ellipsoids. *Science*, 303:990–993, 2004.
- [54] K. J. Dong, R. Y. Yang, R. P. Zou, and A. B. Yu. Role of interparticle forces in the formation of random loose packing. *Physical Review Letters*, 96:145505, 2006.
- [55] J. Duran. Static and dynamic arching effect in granular materials. In H. J. Herrmann, J.-P. Hovi, and S. Luding, editors, *Physics of Dry Granular Media*, pages 197–216. Kluwer Academic Publishers - Dordrecht, 1998.

- [56] J. Duran. *Sands, Powders, and Grains: An Introduction to the Physics of Granular Materials*. Springer-Verlag - New York, 2000.
- [57] D. J. Durian, H. Bideaud, P. Düringer, A. Schröder, F. Thalmann, and C. M. Marques. What is in a pebble shape? *Physical Review Letters*, 97:028001, 2006.
- [58] C. M. Dury, G. H. Ristow, J. L. Moss, and M. Nakagawa. Boundary effects on the angle of repose in rotating cylinders. *Physical Review E*, 57:4491–4497, 1998.
- [59] H. Edelsbrunner. Computational geometry. In P. Gruber and J. Wills, editors, *Handbook of Convex Geometry*, pages 699–735. North-Holland, 1992.
- [60] H. Edelsbrunner. Weighted alpha shapes. Computer Science, Technical Report UIUCDCS-R-92-1760, University of Illinois, Urbana, 1992.
- [61] S. F. Edwards and D. V. Grinev. Granular media as a physics problem. *Advances in Complex Systems*, 4:451–467, 2001.
- [62] S. F. Edwards and D. V. Grinev. Transmission of stress in granular materials as a problem of statistical mechanics. *Physica A: Statistical Mechanics and its Applications*, 302:162–186, 2001.
- [63] P. Evesque. Analysis of the statistics of sandpile avalanches using soil-mechanics results and concepts. *Physical Review A*, 43:2720, 1991.
- [64] P. Ewald. Evaluation of optical and electrostatic lattice potentials. *Ann. Phys. Leipzig*, 64:253–287, 1921.
- [65] M. Faraday. On a peculiar class of acoustic figures, and on certain forms assumed by groups of particles upon vibrating elastic surfaces. *Phil. Trans. Roy. Soc. London*, 52:299–340, 1831.
- [66] Z. Farkas, G. Bartels, T. Unger, and D. E. Wolf. Frictional coupling between sliding and spinning motion. *Physical Review Letters*, 90:248302, 2003.
- [67] S. Fazekas. Szemcsés anyagok számítógépes szimulációja (in Hungarian). Master's thesis, Eötvös Loránd University, 1999. (Supervisor: J. Kertész).
- [68] S. Fazekas, J. Kertész, and D. E. Wolf. Two-dimensional array of magnetic particles: The role of an interaction cutoff. *Physical Review E*, 68:041102, 2003. (cond-mat/0311462).
- [69] S. Fazekas, J. Kertész, and D. E. Wolf. Simulation results on piling and avalanches of magnetized particles. maxwell.phy.bme.hu/~fazekas/magaval, 2004.
- [70] S. Fazekas, J. Kertész, and D. E. Wolf. Computer simulation of magnetic grains. In S. P. Hoogendoorn, S. Luding, P. H. L. Bovy, M. Schreckenberg, and D. E. Wolf, editors, *Traffic and Granular Flow*, pages 489–501. Springer - Berlin, 2005.
- [71] S. Fazekas, J. Kertész, and D. E. Wolf. Piling and avalanches of magnetized particles. *Physical Review E*, 71:061303, 2005. (cond-mat/0404233).

- [72] S. Fazekas, J. Török, and J. Kertész. Critical packing in granular shear bands. *Physical Review E*, 75:011302, 2007. (cond-mat/0604473).
- [73] S. Fazekas, J. Török, J. Kertész, and D. E. Wolf. Computer simulation of three dimensional shearing of granular materials: Formation of shear bands. In R. García-Rojo, H. J. Herrmann, and S. McNamara, editors, *Powders and Grains*, pages 223–226. Balkema - Rotterdam, 2005. (cond-mat/0606720).
- [74] S. Fazekas, J. Török, J. Kertész, and D. E. Wolf. Morphologies of three-dimensional shear bands in granular media. *Physical Review E*, 74:031303, 2006. (cond-mat/0506661).
- [75] J. Feder. The evidence for self-organized criticality in sandpile dynamics. *Fractals*, 3:431–443, 1995.
- [76] C. L. Feng and A. B. Yu. Effect of liquid addition on the packing of mono-sized coarse spheres. *Powder Technology*, 99:22–28, 1998.
- [77] D. Fenistein, J. W. van de Meent, and M. van Hecke. Universal and wide shear zones in granular bulk flow. *Physical Review Letters*, 92:094301, 2004.
- [78] D. Fenistein and M. van Hecke. Kinematics: Wide shear zones in granular bulk flow. *Nature*, 425:256, 2003.
- [79] J.-A. Ferrez. *Dynamic triangulations for efficient 3D simulation of granular materials*. PhD thesis, Monash University, 2002.
- [80] A. J. Forsyth, S. Hutton, and M. J. Rhodes. Effect of cohesive interparticle force on the flow characteristics of granular material. *Powder Technology*, 126:150–154, 2002.
- [81] A. J. Forsyth, S. R. Hutton, C. F. Osborne, and M. J. Rhodes. Effects of interparticle force on the packing of spherical granular material. *Physical Review Letters*, 87:244301, 2001.
- [82] A. J. Forsyth, S. R. Hutton, M. J. Rhodes, and C. F. Osborne. Effect of applied interparticle force on the static and dynamic angles of repose of spherical granular material. *Physical Review E*, 63:031302, 2001.
- [83] A. J. Forsyth and M. J. Rhodes. A simple model incorporating the effects of deformation and asperities into the van der waals force for macroscopic spherical solid particles. *Journal of Colloid and Interface Science*, 223:133–138, 2000.
- [84] Z. Fournier, D. Geromichalos, S. Herminghaus, M. M. Kohonen, F. Muggele, M. Scheel, M. Schulz, B. Schulz, Ch. Schier, and R. Seemann. Mechanical properties of wet granular materials. *Journal of Physics: Condensed Matter*, 17:S477, 2005.
- [85] N. Fraysse, H. Thomé, and L. Petit. Humidity effects on the stability of a sandpile. *European Physical Journal B*, 11:615–619, 1999.
- [86] V. Frette, K. Christensen, A. Malthe-Sørenssen, J. Feder, T. Jøssang, and P. Meakin. Avalanche dynamics in a pile of rice. *Nature London*, 379:49, 1996.

- [87] K. M. Frye and C. Marone. Effect of humidity on granular friction at room temperature. *Journal of Geophysical Research*, 107:2309, 2002.
- [88] R. García-Rojo, H. J. Herrmann, and S. McNamara, editors. *Powders and Grains 2005*. Balkema - Rotterdam, 2005.
- [89] J. Geng, E. Longhi, R. P. Behringer, and D. W. Howell. Memory in two-dimensional heap experiments. *Physical Review E*, 64:060301(R), 2001.
- [90] C. Goldenberg and I. Goldhirsch. Friction enhances elasticity in granular solids. *Nature*, 435:188–191, 2005.
- [91] I. Goldhirsch and G. Zanetti. Clustering instability in dissipative gases. *Physical Review Letters*, 70:1619–1622, 1993.
- [92] Y. Grasselli and H. J. Herrmann. On the angles of dry granular heaps. *Physica A*, 246:301–312, 1997.
- [93] T. C. Hales. An overview of the Kepler conjecture. arxiv.org/math.MG/9811071, 1998.
- [94] T. C. Halsey and A. J. Levine. How sandcastles fall. *Physical Review Letters*, 80:3141, 1998.
- [95] R. R. Hartley and R. P. Behringer. Logarithmic rate dependence of force networks in sheared granular materials. *Nature*, 421:928, 2003.
- [96] K. H. Head. *Effective Stress Tests*, volume 3 of *Manual of Soil Laboratory Testing*. John Wiley and Sons, 2nd edition, 1998.
- [97] L.-O. Heim, J. Blum, M. Preuss, and H.-J. Butt. Adhesion and friction forces between spherical micrometer-sized particles. *Physical Review Letters*, 83:3328, 1999.
- [98] G. A. Held, D. H. Solina, H. Solina, D. T. Keane, W. J. Haag, P. M. Horn, and G. Grinstein. Experimental study of critical-mass fluctuations in an evolving sandpile. *Physical Review Letters*, 65:1120–1123, 1990.
- [99] S. Herminghaus. Dynamics of wet granular matter. *Advances in Physics*, 54:221–261, 2005.
- [100] H. J. Herrmann. Structures in deformed granular packings. *Granular Matter*, 3:15, 2001.
- [101] H. J. Herrmann, J. A. Astrom, and R. M. Baram. Rotations in shear bands and polydisperse packings. *Physica A*, 344:516–522, 2004.
- [102] H. J. Herrmann, J.-P. Hovi, and S. Luding, editors. *Physics of dry granular media*. NATO ASI Series E 350. Kluwer Academic Publishers - Dordrecht, 1998.
- [103] H. J. Herrmann and S. Luding. Modeling granular media on the computer. *Continuum Mechanics and Thermodynamics*, 10:189–231, 1998.

- [104] R. Hoffmann. DEM simulations of toner particles with an $O(N \log N)$ hierarchical tree code algorithm. *Granular Matter*, 8:151–157, 2006.
- [105] D. J. Hornbaker, I. Albert, A. L. Barabási, and P. Schiffer. Why sand castles stand: An experimental study of wet granular media. *Nature London*, 387:765, 1997.
- [106] D. Howell, R. P. Behringer, and C. Veje. Stress fluctuations in a 2D granular Couette experiment: A continuous transition. *Physical Review Letters*, 82:5241–5244, 1999.
- [107] D. W. Howell, I. S. Aranson, and G. W. Crabtree. Dynamics of electrostatically driven granular media: Effects of humidity. *Physical Review E*, 63:050301, 2001.
- [108] S. Hutton. *Sand as a complex system: Inter-particle forces and granular matter*. PhD thesis, Monash University, 2002.
- [109] S. R. Hutton, A. J. Forsyth, M. J. Rhodes, and C. F. Osborne. Effect of interparticle force on mixing and segregation of dry granular materials. *Physical Review E*, 70:031301, 2004.
- [110] J. N. Israelachvili. *Intermolecular and Surface Forces*. Academic Press - San Diego, 2nd edition, 1992.
- [111] H. M. Jaeger, C. Liu, and S. R. Nagel. Relaxation at the angle of repose. *Physical Review Letters*, 62:40–43, 1989.
- [112] H. M. Jaeger and S. R. Nagel. Physics of the granular state. *Science*, 255:1523–1531, 1992.
- [113] H. M. Jaeger, S. R. Nagel, and R. P. Behringer. Granular solids, liquids, and gases. *Reviews of Modern Physics*, 68:1259–1273, 1996.
- [114] H. A. Janssen. Versuche über getreidedruck in silozellen. *Z. Verein Deutsch. Ing.*, 39:1045, 1895.
- [115] V. K. Jasti and C. F. Higgs. A lattice-based cellular automata modeling approach for granular flow lubrication. *Journal of Tribology*, 128:358–364, 2006.
- [116] M. Jean. The non-smooth contact dynamics method. *Comput. Methods Appl. Mech. Engrg.*, 177:235–257, 1999.
- [117] M. J. Jiang, H. S. Yu, and D. Harris. A novel discrete model for granular material incorporating rolling resistance. *Computers and Geotechnics*, 32:340–357, 2005.
- [118] T. B. Jones and J. B. Jones. *Powder Handling and Electrostatics: Understanding and Preventing Hazards*. CRC Press, 1991.
- [119] T. B. Jones, R. D. Miller, K. S. Robinson, and W. Y. Fowlkes. Multipolar interactions of dielectric spheres. *Journal of Electrostatics*, 22:231–244, 1989.
- [120] L. P. Kadanoff. Built upon sand: Theoretical ideas inspired by granular flows. *Reviews of Modern Physics*, 71:435–444, 1999.

- [121] D. Kadau. *Porosität in kohäsiven granularen Pulvern und Nano-Pulvern*. PhD thesis, University Duisburg-Essen, 2003.
- [122] A. R. Kansal, S. Torquato, and F. H. Stillinger. Diversity of order and densities in jammed hard-particle packings. *Physical Review E*, 66:041109, 2002.
- [123] M. Kardar, G. Parisi, and Y.-C. Zhang. Dynamic scaling of growing interfaces. *Physical Review Letters*, 56:889–892, 1986.
- [124] A. Károlyi and J. Kertész. Lattice-gas model of avalanches in a granular pile. *Physical Review E*, 57:852, 1998.
- [125] B. H. Kaye. Characterizing the flowability of a powder using the concepts of fractal geometry and chaos theory. *Particle and Particle Systems Characterization*, 14:53–66, 1997.
- [126] D. Kolymbas. Features of soil behavior and their mathematical modeling. In R. García-Rojo, H. J. Herrmann, and S. McNamara, editors, *Powders and Grains*, pages 403–409. Balkema - Rotterdam, 2005.
- [127] F. Kun, K. F. P al, W. Wen, and K. N. Tu. Break-up of dipolar rings under an external magnetic field. *Physics Letters A*, 277:287–293, 2000.
- [128] F. Kun, W. Wen, K. F. Pál, and K. N. Tu. Breakup of dipolar rings under a perpendicular magnetic field. *Physical Review E*, 64:061503, 2001.
- [129] G. Kuwabara and K. Kono. Restitution coefficient in a collision between two spheres. *Japanese Journal of Applied Physics*, 26:1230–1233, 1987.
- [130] P. V. Lade. Instability, shear banding, and failure in granular materials. *International Journal of Solids and Structures*, 39:3337–3357, 2002.
- [131] P.V. Lade, R.B. Nelson, and Y.M. Ito. Instability of granular materials with nonassociated flow. *Journal of Engineering Mechanics*, 114:2173, 1988.
- [132] T. W. Lambe and R. V. Whitman. *Soil Mechanics*. John Wiley and Sons, 1969.
- [133] L. D. Landau and E. M. Lifshitz. *Theory of elasticity*, chapter 9. Pergamon - New York, 1970. (2nd English ed.).
- [134] F. Lavoie, L. Cartilier, and R. Thibert. New methods characterizing avalanche behavior to determine powder flow. *Pharmaceutical Research*, 19:887–893, 2002.
- [135] C. Lee. Regular triangulations of convex polytopes. In P. Gritzmann and B. Sturmfels, editors, *Applied Geometry and Discrete Mathematics: The Victor Klee Festschrift*, pages 443–456. American Mathematical Society - Providence, 1991.
- [136] P.-A. Lemieux and D. J. Durian. From avalanches to fluid flow: A continuous picture of grain dynamics down a heap. *Physical Review Letters*, 85:4273–4276, 2000.
- [137] Y. Levin. What happened to the gas-liquid transition in the system of dipolar hard spheres? *Physical Review Letters*, 83:1159, 1999.

- [138] Y. Levin. Electrostatic correlations: From plasma to biology. *Reports on Progress in Physics*, 65:1577–1632, 2002.
- [139] H. Li and J. J. McCarthy. Controlling cohesive particle mixing and segregation. *Physical Review Letters*, 90:184301, 2003.
- [140] S. J. Linz and P. Hänggi. Effect of vertical vibrations on avalanches in granular systems. *Physical Review E*, 50:3464–3469, 1994.
- [141] A. J. Liu and S. R. Nagel. Jamming is not just cool anymore. *Nature*, 396:21–22, 1998.
- [142] C. Liu, H. M. Jaeger, and S. R. Nagel. Finite-size effects in a sandpile. *Physical Review A*, 43:7091, 1991.
- [143] B. D. Lubachevsky and F. H. Stillinger. Geometric properties of random disk packings. *Journal of Statistical Physics*, 60:561–583, 1990.
- [144] B. D. Lubachevsky, F. H. Stillinger, and E. N. Pinson. Disks vs. spheres: Contrasting properties of random packings. *Journal of Statistical Physics*, 64:501–524, 1991.
- [145] S. Luding. Molecular dynamics simulations of granular materials. In H. Hinrichsen and D. E. Wolf, editors, *The Physics of Granular Media*. Wiley-VCH - Weinheim, 2004.
- [146] S. Luding, M. Nicolas, and O. Pouliquen. A minimal model for slow dynamics: Compaction of granular media under vibration or shear. In D. Kolymbas and W. Fellin, editors, *Compaction of Soils, Granulates and Powders*, page 241. Balkema - Rotterdam, 2000. (cond-mat/0003172).
- [147] A. Lukkarinen and K. Kaski. Computational studies of compressed and sheared electrorheological fluid. *Journal of Physics D: Applied Physics*, 29:2729–2732, 1996.
- [148] J. M. Luttinger and L. Tisza. Theory of dipole interaction in crystals. *Physical Review*, 70:954–964, 1946.
- [149] T. S. Majmudar and R. P. Behringer. Contact force measurements and stress-induced anisotropy in granular materials. *Nature*, 435:1079–1082, 2005.
- [150] H. A. Makse, D. L. Johnson, and L. M. Schwartz. Packing of compressible granular materials. *Physical Review Letters*, 84:4160–4163, 2000.
- [151] J. E. Martin, R. A. Anderson, and R. L. Williamson. Generating strange magnetic and dielectric interactions: Classical molecules and particle foams. *Journal of Chemical Physics*, 118:1557, 2003.
- [152] T. G. Mason, A. J. Levine, D. Ertaş, and T. C. Halsey. Critical angle of wet sandpiles. *Physical Review E*, 60:R5044–R5047, 1999.
- [153] S. McNamara and W. R. Young. Inelastic collapse in two dimensions. *Physical Review E*, 50:R28–R31, 1994.

- [154] N. Mitarai and F. Nori. Wet granular materials. *Advances in Physics*, 55:1–45, 2006.
- [155] M. A. Mooney, R. J. Finno, and M. G. Viggiani. A unique critical state for sand? *Journal of Geotechnical and Geoenvironmental Engineering*, 124:1100–1108, 1998.
- [156] J. J. Moreau. Some numerical-methods in multibody dynamics - Application to granular-materials. *Eur. J. Mech. A - Solids*, 13:93–114, 1994.
- [157] D. M. Mueth. Measurements of particle dynamics in slow, dense granular Couette flow. *Physical Review E*, 67:011304, 2003.
- [158] D. M. Mueth, G. F. Debregas, G. S. Karczmar, P. J. Eng, S. R. Nagel, and H. M. Jaeger. Signatures of granular microstructure in dense shear flows. *Nature*, 406:385, 2000.
- [159] D. Müller. *Techniques informatiques efficaces pour la simulation de milieux granulaires par des méthodes d'éléments distincts*. PhD thesis, École Polytechnique Fédérale de Lausanne, 1996.
- [160] M.-K. Müller and S. Luding. Long-range interactions in ring-shaped particle aggregates. In R. García-Rojo, H. J. Herrmann, and S. McNamara, editors, *Powders and Grains*, pages 1119–1122. Balkema - Rotterdam, 2005.
- [161] S. R. Nagel. Instabilities in a sandpile. *Reviews of Modern Physics*, 64:321, 1992.
- [162] S. T. Nase, W. L. Vargas, A. A. Abatan, and J. J. McCarthy. Discrete characterization tools for cohesive granular material. *Powder Technology*, 116:214–223, 2001.
- [163] R. M. Nedderman. *Statics and Kinematics of Granular Materials*. Cambridge University Press, 1992.
- [164] E. G. Nezami, Y. M. A. Hashash, D. Zhao, and J. Ghaboussi. A fast contact detection algorithm for 3-d discrete element method. *Computers and Geotechnics*, 31:575–587, 2004.
- [165] E. G. Nezami, Y. M. A. Hashash, D. Zhao, and J. Ghaboussi. Shortest link method for contact detection in discrete element method. *International Journal for Numerical and Analytical Methods in Geomechanics*, 30:783–801, 2006.
- [166] M. Nicolas, P. Duru, and O. Pouliquen. Compaction of a granular material under cyclic shear. *European Physical Journal E: Soft Matter*, 3:309–314, 2000.
- [167] S. Nowak, A. Samadani, and A. Kudrolli. Maximum angle of stability of a wet granular pile. *Nature Physics*, 1:50, 2005.
- [168] M. Oda and H. Kazama. Microstructure of shear bands and its relation to the mechanisms of dilatancy and failure of dense granular soils. *Geotechnique*, 48:465–481, 1998.
- [169] C. S. O’Hern, S. A. Langer, A. J. Liu, and S. R. Nagel. Random packings of frictionless particles. *Physical Review Letters*, 88:075507, 2002.

- [170] C. S. O’Hern, L. E. Silbert, A. J. Liu, and S. R. Nagel. Jamming at zero temperature and zero applied stress: The epitome of disorder. *Physical Review E*, 68:011306, 2003.
- [171] G. Y. Onoda and E. G. Liniger. Random loose packings of uniform spheres and the dilatancy onset. *Physical Review Letters*, 64:2727–2730, 1990.
- [172] C. O’Sullivan, J. D. Bray, and S. Li. A new approach for calculating strain for particulate media. *International Journal for Numerical Methods in Geomechanics*, 27:859–877, 2003.
- [173] N. Otsu. A threshold selection method from gray level histograms. *IEEE Trans. Systems, Man and Cybernetics*, 9:62–66, 1979.
- [174] G. Ovarlez, F. Bertrand, and S. Rodts. Local determination of the constitutive law of a dense suspension of noncolloidal particles through magnetic resonance imaging. *Journal of Rheology*, 50:259–292, 2006.
- [175] M. Paczuski and S. Boettcher. Universality in sandpiles, interface depinning, and earthquake models. *Physical Review Letters*, 77:111–114, 1996.
- [176] J. C. B. Papaloizou and C. Terquem. Planet formation and migration. *Reports on Progress in Physics*, 69:119–180, 2006.
- [177] F. Peters and E. Lemaire. Cohesion induced by a rotating magnetic field in a granular material. *Physical Review E*, 69:061302, 2004.
- [178] M. Piccioni, V. Loreto, and S. Roux. Criticality of the “critical state” of granular media: Dilatancy angle in the tetris model. *Physical Review E*, 61:2813–2817, 2000.
- [179] C. Poirier, M. Ammi, D. Bideau, and J. P. Troadec. Experimental study of the geometrical effects in the localization of deformation. *Physical Review Letters*, 68:216–219, 1992.
- [180] P. Politi, M. G. Pini, and R. L. Stamps. Dipolar ground state of planar spins on triangular lattices. *Physical Review B*, 73:020405, 2006.
- [181] T. Pöschel and T. Schwager. *Computational Granular Dynamics: Models and Algorithms*. Springer - Berlin, 2005.
- [182] L. Pournin, Th. M. Liebling, and A. Mocellin. Molecular-dynamics force models for better control of energy dissipation in numerical simulations of dense granular media. *Physical Review E*, 65:011302, 2001.
- [183] M. A. S. Quintanilla, J. M. Valverde, A. Castellanos, and R. E. Viturro. Looking for self-organized critical behavior in avalanches of slightly cohesive powders. *Physical Review Letters*, 87:194301, 2001.
- [184] J. Rajchenbach. Flow in powders: From discrete avalanches to continuous regime. *Physical Review Letters*, 65:2221–2224, 1990.
- [185] J. Rajchenbach. Granular flows. *Advances in Physics*, 49:229–256, 2000.

- [186] J. Rajchenbach. Dynamics of grain avalanches. *Physical Review Letters*, 88:014301, 2002.
- [187] D. C. Rapaport. *The Art of Molecular Dynamics Simulation*. Cambridge University Press, 2nd edition, 2004.
- [188] F. Restagno, C. Ursini, H. Gayvallet, and É. Charlaix. Aging in humid granular media. *Physical Review E*, 66:021304, 2002.
- [189] O. Reynolds. On the dilatancy of media composed of rigid particles in contact. *Philos. Mag.*, 20:469, 1885.
- [190] P. Richard, M. Nicodemi, R. Delannay, P. Ribiére, and D. Bideau. Slow relaxation and compaction of granular systems. *Nature Materials*, 4:121–128, 2005.
- [191] G. H. Ristow. Granular dynamics: A review about recent molecular dynamics simulations of granular materials. In D. Stauffer, editor, *Annual Reviews of Computational Physics*. World Scientific - Singapore, 1994.
- [192] G. H. Ristow. Flow properties of granular materials in three-dimensional geometries. *Habilitationsschrift*, Philipps-Universität Marburg, 1998.
- [193] J. Rosendahl, M. Vekić, and J. E. Rutledge. Predictability of large avalanches on a sandpile. *Physical Review Letters*, 73:537–540, 1994.
- [194] R. E. Rosensweig. *Ferrohydrodynamics*. Cambridge University Press - Cambridge, 1985.
- [195] L. Rothenburg and N. P. Kruyt. Critical state and evolution of coordination number in simulated granular materials. *International Journal of Solids and Structures*, 41:5763–5774, 2004.
- [196] V. M. Rozenbaum. Coulomb interactions in two-dimensional lattice structures. *Physical Review B*, 53:6240–6255, 1996.
- [197] H. Sakaguchi and H.-B. Mühlhaus. Three-dimensional particle based modelling of frictional behaviour in shear zones. In *Exploration Geodynamics Chapman Conference*, pages 153–155. American Geophysical Union, 2001.
- [198] A. Samadani and A. Kudrolli. Segregation transitions in wet granular matter. *Physical Review Letters*, 85:5102, 2000.
- [199] A. Samadani and A. Kudrolli. Angle of repose and segregation in cohesive granular matter. *Physical Review E*, 64:051301, 2001.
- [200] V. B. Sapozhnikov and E. Foufoula-Georgiou. Experimental evidence of dynamic scaling and indications of self-organized criticality in braided rivers. *Water Resources Research*, 33:1983–1991, 1997.
- [201] S. B. Savage. Modeling and granular material boundary value problems. In H. J. Herrmann, J.-P. Hovi, and S. Luding, editors, *Physics of Dry Granular Media*, page 25. Kluwer Academic Publishers - Dordrecht, 1998.

- [202] J. Schäfer and D. E. Wolf. Bistability in granular flow along corrugated walls. *Physical Review E*, 51:6154, 1995.
- [203] M. Scheel, D. Geromichalos, and S. Herminghaus. Wet granular matter under vertical agitation. *Journal of Physics: Condensed Matter*, 16:S4213–S4218, 2004.
- [204] P. Schiffer. Granular physics: A bridge to sandpile stability. *Nature Physics*, 1:21–22, 2005.
- [205] A. N. Schofield and P. Wroth. *Critical State Soil Mechanics*. McGraw-Hill - London, 1968.
- [206] H. Schubert. Capillary forces: Modeling and application in particulate technology. *Powder Technology*, 37:105–116, 1984.
- [207] J. Schwedes. Review on testers for measuring flow properties of bulk solids. *Granular Matter*, 5:1, 2003.
- [208] G. D. Scott. Packing of equal spheres. *Nature London*, 188:908–909, 1960.
- [209] I. E. M. Severens. *DEM Simulations of Toner Behaviour in the Development Nip of the Océ Direct Imaging Print Process*. PhD thesis, Eindhoven University of Technology, 2005.
- [210] J. D. Sherwood. Packing of spheroids in three-dimensional space by random sequential add. *Journal of Physics A: Mathematical and General*, 30:L839–L843, 1997.
- [211] A. Snezhko, I. S. Aranson, and W.-K. Kwok. Structure formation in electromagnetically driven granular media. *Physical Review Letters*, 94:108002, 2005.
- [212] E. Somfai, A. Czirók, and T. Vicsek. Power-law distribution of landslides in an experiment on the erosion of a granular pile. *Journal of Physics A: Mathematical and General*, 27:757–763, 1994.
- [213] F. Spahn. Planetary rings: Nonequilibrium systems in space. In L. Schimansky-Geier and Th. Pöschel, editors, *Stochastic Dynamics*, volume 484 of *Lecture Notes in Physics*, pages 372–386. Springer-Verlag, 1998.
- [214] J. Stambaugh, D. P. Lathrop, E. Ott, and W. Losert. Pattern formation in a monolayer of magnetic spheres. *Physical Review E*, 68:026207, 2003.
- [215] J. Stambaugh, Z. Smith, E. Ott, and W. Losert. Segregation in a monolayer of magnetic spheres. *Physical Review E*, 70:031304, 2004.
- [216] J. J. Stickel and R. L. Powell. Fluid mechanics and rheology of dense suspensions. *Annual Review of Fluid Mechanics*, 37:129–149, 2005.
- [217] L. Szalmás, J. Kertész, and M. Zrínyi. Experimental study of systems of magnetized particles (unpublished). L. Szalmás, Master's thesis (in Hungarian), Budapest University of Technology and Economics (2000).
- [218] C. Tan and T. B. Jones. Interparticle force measurements on ferromagnetic steel balls. *Journal of Applied Physics*, 73:3593–3598, 1993.

- [219] C. Tang and P. Bak. Critical exponents and scaling relations for self-organized critical phenomena. *Physical Review Letters*, 60:2347–2350, 1988.
- [220] D. M. Taylor and P. E. Secker. *Industrial Electrostatics: Fundamentals and Measurements*. Wiley and Sons - New York, 1994.
- [221] P. Tegzes, R. Albert, M. Paskvan, A. L. Barabási, T. Vicsek, and P. Schiffer. Liquid-induced transitions in granular media. *Physical Review E*, 60:5823–5826, 1999.
- [222] P. Tegzes, T. Vicsek, and P. Schiffer. Avalanche dynamics in wet granular materials. *Physical Review Letters*, 89:094301, 2002.
- [223] P. Tegzes, T. Vicsek, and P. Schiffer. Development of correlations in the dynamics of wet granular avalanches. *Physical Review E*, 67:051303, 2003.
- [224] J. Tejchman. FE analysis of contractant shear zones in loose granular materials. *Granular Matter*, 9:49–67, 2007.
- [225] J. M. Thijssen. *Computational Physics*, chapter Molecular dynamics simulations, pages 175–241. Cambridge University Press, 1999.
- [226] J. Török, S. Fazekas, T. Unger, and D. E. Wolf. Relationship between particle size and normal force. In R. García-Rojo, H. J. Herrmann, and S. McNamara, editors, *Powders and Grains*, pages 1273–1277. Balkema - Rotterdam, 2005.
- [227] J. Török, J. Kertész, S. Krishnamurthy, and S. Roux. Self-organization, localization of shear bands and aging in loose granular materials. *Physical Review Letters*, 84:3851, 2000.
- [228] J. Török, S. Krishnamurthy, J. Kertész, and S. Roux. Shearing of loose granular materials: A statistical mesoscopic model. *Physical Review E*, 67:021303, 2003.
- [229] J. Török, T. Unger, D. E. Wolf, and J. Kertész. Shear zones in granular materials: Optimization in a self-organized random potential. *Physical Review E*, 75:011305, 2007.
- [230] S. Torquato, T. M. Truskett, and P. G. Debenedetti. Is random close packing of spheres well defined? *Physical Review Letters*, 84:2064–2067, 2000.
- [231] V. Trappe, V. Prasad, L. Cipelletti, P. N. Segre, and D. A. Weitz. Jamming phase diagram for attractive particles. *Nature*, 411:773–775, 2001.
- [232] H. Tsunekawa and K. Iwashita. Numerical simulation of triaxial test using two and three dimensional DEM. In Y. Kishino, editor, *Powders and Grains*, pages 177–180. Balkema - Rotterdam, 2001.
- [233] D. L. Turcotte. Self-organized criticality. *Reports on Progress in Physics*, 62:1377–1429, 1999.
- [234] D. L. Turcotte and J. B. Rundle. Self-organized complexity in the physical, biological, and social sciences. *Proceedings of the National Academy of Sciences of USA*, 99:2463–2465, 2002.

- [235] T. Unger. *Characterization of static and dynamic structures in granular materials*. PhD thesis, Budapest University of Technology and Economics, 2004.
- [236] T. Unger. Refraction of shear zones in granular materials. *Physical Review Letters*, 98:018301, 2007.
- [237] T. Unger, J., and Kertész. The contact dynamics method for granular media. In *Modeling of Complex Systems*, page 116. American Institute of Physics - Melville, New York, 2003.
- [238] T. Unger and J. Kertész. Frictional indeterminacy of forces in hard-disk packings. *International Journal of Modern Physics B*, 17:5623, 2003.
- [239] T. Unger, J. Kertész, and D. E. Wolf. Force indeterminacy in the jammed state of hard disks. *Physical Review Letters*, 94:178001, 2005.
- [240] T. Unger, J. Török, J. Kertész, and D. E. Wolf. Shear band formation in granular media as a variational problem. *Physical Review Letters*, 92:214301, 2004.
- [241] P. Du Val. *Homographies, quaternions, and rotations*. Clarendon Press - Oxford, 1964.
- [242] J. M. Valverde and A. Castellanos. Random loose packing of cohesive granular materials. *Europhysics Letters*, 75:985–991, 2006.
- [243] J. M. Valverde, A. Castellanos, A. Ramos, and P. K. Watson. Avalanches in fine, cohesive powders. *Physical Review E*, 62:6851–6860, 2000.
- [244] J. M. Valverde, A. Ramos, A. Castellanos, and P. K. Watson. The tensile strength of cohesive powders and its relationship to consolidation, free volume and cohesivity. *Powder Technology*, 97:237–245, 1998.
- [245] L. Vanel, D. Howell, D. Clark, R. P. Behringer, and Eric Clément. Memories in sand: Experimental tests of construction history on stress distributions under sandpiles. *Physical Review E*, 60:R5040–R5043, 1999.
- [246] I. Varga, H. Yamada, F. Kun, H.-G. Matuttis, and N. Ito. Structure formation in a binary monolayer of dipolar particles. *Physical Review E*, 71:051405, 2005.
- [247] C. T. Veje, D. W. Howell, and R. P. Behringer. Kinematics of a two-dimensional granular Couette experiment at the transition to shearing. *Physical Review E*, 59:739–745, 1999.
- [248] C. T. Veje, D. W. Howell, R. P. Behringer, S. Schöllmann, S. Luding, and H. J. Herrmann. Fluctuations and flow for granular shearing. In H. J. Herrmann, J.-P. Hovi, and S. Luding, editors, *Physics of Dry Granular Media*, pages 697–702. Kluwer Academic Publishers - Dordrecht, 1998.
- [249] G. Viggiani, M. Küntz, and J. Desrues. An experimental investigation of the relationships between grain size distribution and shear banding in sand. In P. A. Vermeer, S. Diebels, W. Ehlers, H. J. Herrmann, S. Luding, and E. Ramm, editors, *Continuous and Discontinuous Modelling of Cohesive-Frictional Materials*, volume 568 of *Lecture Notes in Physics*, page 111. Springer Verlag - Berlin, 2001.

- [250] O. R. Walton and R. L. Braun. Viscosity, granular-temperature, and stress calculations for shearing assemblies of inelastic, frictional discs. *Journal of Rheology*, 30:949, 1986.
- [251] Z. Wang and C. Holm. Estimate of the cutoff errors in the Ewald summation for dipolar systems. *Journal of Chemical Physics*, 115:6351–6359, 2001.
- [252] J. J. Weis. Orientational structure in a monolayer of dipolar hard spheres. *Molecular Physics*, 100:579–594, 2002.
- [253] J.-J. Weis. Simulation of quasi-two-dimensional dipolar systems. *Journal of Physics: Condensed Matter*, 15:S1471, 2003.
- [254] D. A. Weitz. Packing in the spheres. *Science*, 303:968–969, 2004.
- [255] W. Wen, F. Kun, K. F. Pál, D. W. Zheng, and K. N. Tu. Aggregation kinetics and stability of structures formed by magnetic microspheres. *Physical Review E*, 59:R4758–R4761, 1999.
- [256] W. Wen, F. Kun, K. F. Pál, D. W. Zheng, and K. N. Tu. Aggregation kinetics and stability of structures formed by magnetic microspheres. *Physical Review E*, 59:R4758–R4761, 1999.
- [257] J. H. Werth, H. Knudsen, and H. Hinrichsen. Agglomeration of oppositely charged particles in nonpolar liquids. *Physical Review E*, 73:021402, 2006.
- [258] J. H. Werth, M. Linsenbuehler, S. M. Dammer, Z. Farkas, H. Hinrichsen, K.-E. Wirth, and D. E. Wolf. Agglomeration of charged nanopowders in suspensions. *Powder Technology*, 133:106–112, 2003.
- [259] D. M. Wood. *Soil Behaviour and Critical State Soil Mechanics*. Cambridge University Press - New York, 1990.
- [260] J. Q. Xu, R. P. Zou, and A. B. Yu. Packing structure of cohesive spheres. *Physical Review E*, 69:032301, 2004.
- [261] T. L. Youd. Compaction of sands by repeated shear straining. *Journal of the Soil Mechanics and Foundations Division*, 98:709–725, 1972.
- [262] H. P. Zhang and H. A. Makse. Jamming transition in emulsions and granular materials. *Physical Review E*, 72:011301, 2005.
- [263] Y. C. Zhou, B. D. Wright, R. Y. Yang, B. H. Xu, and A. B. Yu. Rolling friction in the dynamic simulation of sandpile formation. *Physica A*, 269:536–553, 1999.
- [264] Y. C. Zhou, B. H. Xu, A. B. Yu, and P. Zull. An experimental and numerical study of the angle of repose of coarse spheres. *Powder Technology*, 125:45–54, 2002.
- [265] J. Zhu, M. Li, R. Rogers, W. Meyer, R. H. Ottewill, STS-73 Space Shuttle Crew, W. B. Russel, and P. M. Chaikin. Crystallization of hard-sphere colloids in microgravity. *Nature*, 387:883–885, 1997.

- [266] X. Zhuang, A. K. Didwania, and J. D. Goddard. Simulation of the quasi-static mechanics and scalar transport-properties of ideal granular assemblages. *Journal of Computational Physics*, 121:331–346, 1995.